Università degli studi di Roma

Tor Vergata

Facoltà di Scienze Matematiche Fisiche e Naturali

Corso di laurea magistrale in Fisica

ON THE KINEMATICS OF THE SCULPTOR DWARF SPHEROIDAL GALAXY

Supervisor:
Prof. Giuseppe Bono

Co-supervisor:
PhD. Michele Fabrizio

Author:

Tadeja Veršič

A thesis submitted in partial fulfilment of the requirements for the degree of

Master of Science

at the University of Rome, "Tor Vergata"

Academic year 2016/2017

On the Kinematics of the Sculptor Dwarf Spheroidal Galaxy

by

Tadeja Veršič

Submitted to the Università degli Studi di Roma Tor Vergata
and
Universität Innsbruck
on September 29, 2017, in partial fulfillment of the
requirements for the degree of
Master of Science in Astrophysics

Abstract

Dwarf galaxies are simple and strongly dark matter dominated stellar structures. They offer an intriguing insight into evolutionary processes at low halo masses and low metallicities. The studies of the whole population of dwarf galaxies in the Local Group can, among other things, provide insight into the hierarchical structure formation in the cosmological frame. While investigating, individual dwarf galaxies can shed light on the details of the build up process of the host galaxy. In this work I present the complete set of radial velocities (RV) obtained using all available pre-reduced spectra at the ESO archive for Sculptor dwarf spheroidal galaxy (dSph). In total, 7313 multiple spectra (majority spanning $16.5 \leq V \leq 20$) were used for RV measurements. After combining the multiple measurements and removing measurements with poor precision, 942 stars had assigned radial velocity. Combining with ~ 1500 literature radial velocities from the MIKE spectrograph, I compiled a sample of ~ 2200 stars in the direction of Sculptor, increasing the current literature samples by 50%. In this work the radial velocity data-sets from the ESO facilities and the MIKE spectrograph are combined for the first time in a systematic way, by comparing measurements from individual stars instead of systemic velocities. Using the kinematic selection to discriminate between field and galactic stars, a final catalogue was created consisting of 1652 radial velocity members ($80.6km/s < rv < 139.7km/s$), with the average error better than $3km/s$. This sample is 50% larger than what has been reported so far for this galaxy. The radial velocity members span the whole body of the galaxy also beyond the nominal tidal radius ($r_t = 76' \pm 5'$). All the stellar tracers of intermediate-age (red giant branch and red clump stars) and old (red giant branch and red horizontal branch) stellar populations are present. The values for the systemic velocity $v_{systemic} = 110.14 \pm 0.02km/s$ and velocity dispersion $\sigma = 9.86 \pm 0.06km/s$ are in good agreement with the recent values found in the literature and are one order of magnitude more precise than previous investigations, owing to the increase in the sample size. The kinematic Sculptor members extend up to or beyond the tidal radius almost at every azimuthal angle. Such complete sample of radial velocities is

presented for the first time and allows for systematic analysis of radial and angular variation of $v_{l.o.s.}$ and σ. The radial variation of radial velocities agree with the trends presented in several papers, but not all of them. It shows a steadily decreasing trend at large radial distances ($r > 35'$) and two minima in the angular plots (in the I and IV quadrant) indicating a slight rotation towards the Sun of the northern part of the galaxy compared with the southern one. Signs of rotation have been presented in the literature. Velocity dispersion shows a constantly increasing trend as a function of elliptic radius up to the tidal radius and an almost constant value across all azimuthal angles.

Thesis Supervisor: Giuseppe Bono
Title: Professor

Thesis Supervisor: Michele Fabrizio
Title: Researcher

Acknowledgements

Special thanks goes to the Astromundus selection committee for selecting me to participate in a master's program that culminated with the submission of this thesis. As well as my thesis advisor Giuseppe Bono and co-advisor Michele Fabrizio for enabling me to tackle this problem and provided guidance throughout my work. To Elena Valenti and Davide Magurno for their help. My former professors, friends, sisters and parents for their support.

Najlepša hvala

Work is based on the spectra retrieved from the ESO/ST-ECF Science Archive Facility: UVES/ECHELLE at ESO/VLT (65.N-0378(A) P.I.: E. Tolstoy, 291.B-5036(A) P.I.: E. Tolstoy, 281.B-5022(A) P.I.: P. Jablonka, 091.D-0912(A) P.I.: P. Jablonka, 087.D-0928(A) P.I.: P. Jablonka, 079.B-0672(A) P.I.: P. Jablonka); FLAMES/GIRAFFE at ESO/VLT: (71.B-0641(A) P.I.: V. Hill, 092.B-0564(A) P.I.: S. Fouquet, 092.B-0194(A) P.I.: E. Tolstoy, 089.B-0304(B) P.I.: E. Tolstoy, 593.D-0309(A)(B)(C) P.I.: G. Battaglia, 171.B-0588(A)(D) P.I.: E. Tolstoy, 079.B-0435(A) P.I.: G. Battaglia, 076.B-0391(A) P.I.: G. Battaglia, 072.D-0245(C) P.I.: A.-M. Hubert)

Contents

List of Figures

List of Tables

Chapter 1

Introduction

Galaxies represent the basic unit of the Universe. These gravitationally bound systems of baryonic and non-baryonic matter were the first structures to be formed and span a large range of luminosities, masses, kinematic and metallicity properties. In the last couple of decades series of photometric and spectroscopic studies have unveiled a series of relations between the structural parameters of different morphological types of galaxies. The least massive among them - the dwarf galaxies, are predicted by galaxy formation theories and cosmological models to be the building blocks that form larger structures through mergers.

The objective of this thesis is to present the largest, most precise and homogeneous sample of radial velocity measurements for the *Sculptor Dwarf Spheroidal Galaxy (dSph)*. The first chapter provides a brief overview of some of the current open problems that can be resolved by studying the internal kinematics of dwarf galaxies with the emphasis on Sculptor. The sample of spectroscopic and photometric data that I used is introduced in chapter two, followed by the discussion on the status of the spectra and their preparation for the measurements in the third chapter. Method of obtaining the radial velocities and their analysis is presented in chapter four with the following fifth chapter focused on the results of my work. The sixth chapter concludes the thesis with a brief review of the master research work as well as highlights some possibilities for future work.

1.1 Dwarf Galaxies

Most generally, galaxies can be separated into two classes: *normal galaxies* and *dwarfs*. Simulations indicate that while normal galaxies are formed through mergers with other galaxies, dwarfs, showing only the evidence of in-situ star formation, formed by gas accretion onto a dark matter halo[1]. Further empirical classification, based on observables such as the integrated color, surface brightness and magnitude, splits the galaxies into several morphological types[2].

The boundaries of morphological classes are not rigidly defined and historically the distinction between dwarf and normal galaxies comes from the observed difference in the shape of the surface brightness profile. Elliptical galaxies with $M_B \geq -18$ cannot be fitted with the de Vaucouleurs $R^{1/4}$ profile as well as the ellipticals brighter than this limit. Instead, they show an exponential decline of surface brightness with increasing radius, much like the spiral galaxies. Thus, indicating different physical properties compared with their brighter counterparts [13]. Another threshold was set at a fainter magnitude of $M_B \geq -16$ with an additional condition, that such galaxy needs to be more spatially extended than the globular clusters. Unlike galaxies, globular clusters show no trace of dark matter. The latter limit is broadly consistent with the mass of the galaxy at which outflows start to significantly affect the baryonic mass of the galaxy [24].

Dwarf galaxies are most generally split into two subtypes: *Early-type dwarfs* are gas poor and largely quiescent galaxies, predominantly found in denser regions; *Late-type galaxies* are gas rich, show several star-forming HII regions and are usually located in low-density environment[13].

Although all galaxy types deserve special attention, only the dwarf spheroidal

[1] Projects like the Millennium Simulation `http://wwwmpa.mpa-garching.mpg.de/galform/virgo/millennium/` and more recently the Illustris Simulation `http://www.illustris-project.org/`.

[2] Different combinations of these observables and the parameters that can be derived from them, can be used to investigate, whether there is any relation between different morphological types in order to study possible evolutionary paths of galaxies. Elliptical, spiral and lenticular galaxies comprise the normal galaxies and dwarfs are split into dwarf ellipticals, dwarf spheroidal, compact ellipticals, ultra compact dwarfs, blue compact dwarfs, dwarf irregulars and recently discovered ultra faint dwarfs.

galaxies will be briefly presented in this section.

Early-type: Dwarf Spheroidal Galaxies Characteristic of this type is a very low surface brightness, which makes them difficult to observe beyond the Local Volume. They show almost no evidence of gas[3] or young stars. Star formation has been quenched in most dSph galaxies $\sim 10Gyr$ ago (like Sculptor), with some showing extended star formation periods up to $\sim 1Gyr$ ago like the Fornax and Carina dSph ([24] and references therein). They are typically found in dense galactic regions where interactions with other galaxies are more frequent. Tidal interactions, additionally to the supernovae and stellar winds, effectively strip the gas from these galaxies, thereby quenching star formation. These types of galaxies are metal poor with average metallicity ranging between $-2.72 <$[Fe/H]< -0.25 ([11] and references therein). Their structure is relatively regular and their dispersion velocity, that ranges between $2.4 - 15.8 km/s$ ([11] and references therein) results in dynamic mass to light ratio of several tens to more than one hundred that of the solar ratio ($160 M_\odot/L_\odot$ has been reported for Sculptor dSph [3]), meaning that they are among the most dark matter dominated stellar structures[4].

1.2 Open Problems - What Can We Learn From Dwarf Galaxies

Dwarf galaxies stand at the apex of several open problems in modern astrophysics and cosmology. With the advent of large telescopes (with mirror sizes exceeding $5m$) enabling spectroscopic and photometric surveys of a great number of individual galaxies and stars, dwarf galaxies became the subject of many detailed photometric and spectroscopic observations. This work takes advantage of several such surveys.

[3] Gas content was measured for three dSphs with an average value of $0.22 \cdot 10^6 M_\odot$ ([11] and references therein).

[4] Initial investigation of the ultra faint dwarfs points to $M_\odot/L_\odot \approx 1000$ making them more suitable for dark matter studies. However, owing to their low surface brightness and mass they are not easy to detect or study in detail.

In this section, I would like to highlight the most relevant open problems to stress the importance of these objects. They serve to demonstrate the importance of kinematic studies of dSph, however, any attempt to clarify any of them, using the data presented in this work, is beyond the scope of this thesis.

Currently, the most accepted theory of the evolution of the Universe - ΛCDM[5] shows good agreement between various observations on a large range of scales. However, several predictions on the smallest scales show great discrepancy with current observations. According to the ΛCDM, low mass dark matter halos formed first, followed by more massive ones. This has been confirmed over the last decades with the detection of a large number of satellite dwarfs around the Milky Way, the Andromeda galaxy and in the Virgo cluster. Beyond the Local Volume the intrinsically faint dwarfs fall below the detection limit of the current telescopes (without the help of gravitational lensing).

1.2.1 Galaxy Formation

Hierarchical structure formation is favoured by the hydrodynamical simulations in the framework of the ΛCDM cosmology. This was observationally reinforced, at the turn of the century, by tracing the luminosity function of galaxies as a function of cosmological redshift. Galaxy luminosity function can be plotted by counting the number of galaxies in a given magnitude bin. Using the large sample of galaxies in the SDSS[6], a decrease in the number of bright galaxies with the increasing redshift was found. This was seen as an increase in the power at the faint end of the luminosity function. The trend is also color dependant (it is most apparent for blue, starforming galaxies and less for red, passive galaxies), but for the total population of galaxies at a given redshift this was found to be the dominant trend.

Thus, in the past there were more smaller galaxies and the remaining dwarf galaxies we observe today are the fossil records of the formation process. During the close

[5] Cosmology whit the cosmological constant Λ and where most of the gravitational mass is in the form of Cold Dark Matter - i.e. massive, non-relativistic particles.

[6] Sloan Digital Sky Survey.

encounters of the satellite dwarfs with its host galaxy, which can lead to merger or tidal disruption, the internal kinematics of stars is modified. Thus, sufficiently large sample of radial velocity measurements can identify the imprint left over by previous interactions, as was found in the analysis of the Carina dSph [7].

1.2.2 Core/Cusp Problem

The, dark matter only, ΛCDM simulations predict that the radial density profile of relaxed dark matter halos follow a universal form, known as the Navarro, Frenk, White (NFW) profile (Navarro et al. [15], [16]). This **cusped** model predicts a divergent total mass density profile $\rho_{DM}(r) \propto r^{-1}$. However, the baryonic effects in real galaxies tend to flatten this central cusp through explosive events like supernovae into a **cored profile**. Such feedback has been proposed by Navarro et al. 1996 [15] and was also found in a number of galaxy formation simulations (see Pontzen & Governato, 2014 [18] for review).

However, owing to their lower mass and supernovae rate, this feedback process should cease to be effective in dwarf galaxies. According to Peñarrubia et al. 2012 [17] dwarf galaxies with stellar mass between 10^6 and 10^7 $M_\odot$ should still have primordial - cuspy density profile.

In the past two decades the number of line-of-sight velocities and metallicites for Galactic dwarf galaxies has increased significantly[7]. Novel dynamical and chemo-dynamical models are still unable to discriminate between the two proposed density profiles. This is mainly due to the size of the radial velocity sample that cover only the bright red giant branch (RGB)[8] stars. Partly it is also due to the assumptions on the shape of the galaxy as well as the assumptions on the 3-dimensional velocity dispersion involved in the modelling[4].

[7]DART Survey, https\\www.astro.rug.nl\∼ etolstoy\dart.html, Magellan MMFS Survey [26]

[8]Red giant branch stars are evolved phases of stars. As the hydrogen in the stellar core is exhausted, they become bigger, brighter and cooler while burning the hydrogen in the shell surrounding the inert core. Their increased luminosity makes them the best spectroscopic targets for large surveys outside our Galaxy.

1.2.3 The Missing Satellite Problem

The dark matter only cosmological simulations on galactic and cluster scales predict much larger numbers of small dark matter halos than dwarf galaxies observed (Moore et al. 1999 [14]). However, recent attempts to account for the density of the local environment, re-ionization, stellar feed back and the discovery of even fainter dwarf galaxies (the ultra faint dwarfs) have shown promising results in resolving this problem (Sawala et al. 2016 [20]). With these considerations the number of predicted and observed dwarf galaxies are in good agreement. But additional confirmation is needed to mark this problem resolved.

1.2.4 Too Big to Fail

This problem concerns the dark matter subhalos with $M \sim 10^{10} M_{\odot}$. Such massive halos should not be affected by the re-ionization process, yet their internal structure seems incompatible with that observed in the brightest Galactic dwarfs. Simulations predict much higher central velocity dispersion than observed for the dark matter halos at this mass (Boylan-Kolchin et al. 2011 [5]). Simulations indicate that this discrepancy may also be explained by accounting for the stellar feed-back processes. However, more detailed studies of systems in these mass ranges is required before a definite explanation is found.

These are just some of the open problems that can be addressed by studying the internal kinematics of dwarf galaxies. Metallicity and star formation history studies are also essential in understanding the process of structure formation and galaxy evolution.

1.3 The Local Group

Owing to its proximity, the Local Group represents the best location for detailed spectroscopic studies of dwarf galaxies. Thus, before continuing with the next chapter, a short overview of the galaxies residing in the Local Group is in order. The Local

Group largest members are the Milky Way and the Andromeda galaxy - M31. The majority of the Local Group members are satellite galaxy of either our Galaxy or M31.

Being more massive, the Andromeda galaxy has a larger entourage of gas rich satellites as well as more dwarf spheroidal galaxies than the Milky Way. Dwarfs orbiting around Andromeda have recently become a target for detailed photometric and spectroscopic studies[9].

1.3.1 Galactic Dwarf Galaxies

Orbiting the Milky Way and actively star forming, the gas rich Magellanic Clouds are the largest of its satellite galaxies. The majority of the others are gas poor dSph galaxies accounting for roughly 80% of the Galactic satellites. Among the closest ones, Sagittarius ($26kpc$ [11] and references therein) and Fornax ($47kpc$ [11] and references therein) are currently being stripped into streams by tidal forces. For the other Galactic dSph galaxies little or no evidence has been found in their internal kinematics that would confirm tidal disruptions. These recently discovered tidal streams highlight the importance of dwarf galaxies in the built up of our Galaxy and its halo. The origin of the globular clusters is still not well understood. Metallicity studies of satellite dwarf galaxies could provide better understanding of the sources of these compact stellar systems as well as other field stars.

1.4 Case Study - Sculptor dSph

The discovery of this prototypical dwarf spheroidal galaxy dates back to 1938 [21]. Harlow Shapely reported its observation together with the Fornax dSph, making them the first Galactic satellites (aside from the Magellanic clouds) to be discovered. Sculptor is located $\sim 85kpc$ from the Sun at high Galactic latitudes. Relevant structural parameters are summarized in the table 1.1.

[9] `http://www.astro.uvic.ca/~alan/PANDAS/Home.html`

Parameters		Parameters	
$\alpha(J2000)^a$	$01^h00^m09.4^s$	$r_c{}^a$	$5.8' \pm 1.6'$
$\delta(J2000)^a$	$33^o42'33''$	$r_t{}^a$	$76' \pm 5'$
l^a	287.5^o	ϵ^a	0.3 ± 0.032
b^a	83.2^o	$P.A.^a$	$99^o \pm 1^{o\,(*)}$
M_V^a	11.1 ± 0.5 mag	$v_{l.o.s.}^{Scl\ c}$	$110.6 \pm 0.5\,km/s$
$E(B-V)^a$	0.018 mag	σ^c	$10.1 \pm 0.3\,km/s$
d^a	$86 \pm 6\,kpc$	$\mu_{RRLyrae}{}^b$	19.63 ± 0.06 mag

Table 1.1: Relevant parameters for the Sculptor dSph
[a] From McConnachie 2012 [11]
[b] From Martínez-Vázquez et al. 2015 [9], based on Period-Wesenheit-Metallicity relation of RR Lyrae stars
[c] From Battaglia et al.2007 [3]
(*) Here $\theta = 0^o$ corresponds to north and $\theta = 90^o$ to east.

Star Formation History Initial star formation history (SFH) studies, that used only the color magnitude diagram (CMD) to which isochrones[10] were fitted, found that the galaxy experienced a single star formation event. Recent investigation using the metallicity to fit two stellar populations instead of one, have shown better agreement with the observed CMD and metal content of Sculptor. The study conducted by de Boer et al. 2013 [6] found that the photometric and spectroscopic data best fit a single burst of star formation between 13 and $14\,Gyr$ ago where roughly 80% of the galactic stars were formed. The initial burst was followed by an extended period, terminated around $6 - 7\,Gyr$ ago, where stars were formed with increasing central concentration. Authors found that Sculptor can be considered a good benchmark for an isolated system with star formation over extended period during the early epoch of the Universe[6]. This different star formation periods are also reflected in the metallicity and kinematics. Centrally concentrated stars have, on average, higher metallicity and were created during the extended star formation period, they show smaller velocity dispersion than the more metal poor stars created in the initial burst.

Metallicities Spectroscopic studies of red giant branch stars in the galaxy show two populations of red giant branch stars depending on their metallicity. Metal poor (MP) stars peak at $[Fe/H] \sim -2$, with dispersion of 0.26 dex, and they are found

[10] Locus of points on the CMD corresponding to the stars of the same age but different mass.

throughout the galaxy. Metal rich (MR) stars peak at $[Fe/H] \sim -1.5$, with slightly smaller metallicity dispersion of 0.2 dex, and they are more centrally concentrated [3]. This dichotomy is, however, not found in the RR Lyrae population along the horizontal branch [9].

Kinematics and Dynamical Models In the recent years two large surveys focused on studying the kinematics and chemical content of the Sculptor dSph together with other bright dwarf galaxies (DART Survey and Magellan MMFS Survey). The dynamical modelling of the distribution of the line of sight velocities is needed to determine the dynamical mass of a galaxy. Though very high mass to light ratio have been consistently reported for Sculptor, the exact value depends on the adopted model. The past models used only the brightest - red giant branch stars to constrain the velocity dispersion at different radii but in the last few years, with increasing number of metallicity measurements, the RGB stars could be split into two populations depending on their relative metal content. Short summary of the observed systemic velocity, velocity dispersion and the method for radial velocity measurements is found in table 1.2. The so called chemo-dynamical models take advantage of this additional information and use the two populations to trace the same gravitational potential, mainly to determine the dark matter distribution. A recent attempt to reconcile different data sets and modelling techniques found that none of the published sets can exclude the cusp NFW profile even if the data consistently prefer the cored profile [22].

Even though my work focuses on the kinematics of the Sculptor dSph alone I felt it necessary to provide a brief overview of the recent development in the field to show how different measurements have been put together to get a complete and comprehensive view of this dwarf galaxy. This galaxy and other satellites in the Local Group have been studied significantly and great advances have been made in the field of galaxy formation and dynamical modelling in attempts to understand the observational data. But in order to clarify and resolve the existing problems larger and more homogeneous data samples across different stellar tracers are needed.

source	# stars	$v_{l.o.s.}^{Scl}[km/s]$	$\sigma[km/s]$	comment
Armandroff and da Costa [2]	16 RGB	107.4 ± 2.0	$6.3^{+1.1}_{-1.3}$	cc of CaT[a)]
Queloz, Dubath and Pasquini [19]	21 RGB	109.9 ± 1.4	6.2 ± 1.1	cc[b)]
Walker et al. [25]	1365 RGB	111.4 ± 0.1	9.2 ± 1.1	cc of MgT[c)]
Battaglia et al. [3]	470 RGB	110.6 ± 0.5	10.1 ± 0.3	cc of CaT[d)]

Table 1.2:
[a)] Based on cross correlation (cc) of the region around the near infrared CaII triplet (CaT) with a template spectrum made from 4 radial velocity standard stars.
[b)] Based on CORAVEL - a Cassegrain spectrophotometer for determining stellar radial velocities by cross-correlation. Standard velocity stars were used as templates for cross correlation.
[c)] Measurements were obtained by cross correlating composite template spectra of >200 standard radial velocity stars around the 5170Å magnesium triplet MgT.
[d)] Synthetic spectra were made convolving flat continuum with three Gaussians corresponding to the position of the CaT lines at $8498, 8542$ and 8662Å.

Chapter 2

Photometric and Spectroscopic Data Sets

The photometric and spectroscopic data set of candidate Sculptor stars used in this work is presented in this chapter. In the first section the photometric catalogue is introduced. The emphasis of this chapter is on the spectroscopic dataset, therefore, relevant instruments will be briefly introduced followed by the details of the spectroscopic data set. The number of spectra and objects taken with every instrumental set-up is presented in the second section. Finally the overlap between the subsets of different resolution is discussed.

2.1 Photometric Catalogue

Photometric studies always supersede the spectroscopic ones, since the light is not dispersed but all the flux passing through a given photometric filter is integrated. This results in much fainter limiting magnitude compared with spectroscopy observations (for Sculptor the photometric catalogue includes stars down to the 28th magnitude, whereas in the spectroscopic dataset few stars are fainter than 20.5 magnitude). This allows for the photometric studies to reach the stars below the main-sequence turn-off

(MSTO[1]) of the Galactic satellite galaxies. These stars are not accessible with current spectroscopic facilities. With photometric studies CMD can be constructed and variability studied. The color magnitude diagram also has a theoretical equivalent, the Hertzsprung-Russell diagram, and stars (once the distance and reddening have been accounted for) can be associated with a specific evolutionary phase based on their location on the CMD. Empirically, it has also been found that the coeval and monometallic populations are found in a narrow region along the color-color (CC)[2] plane in specific combination of colors (such an example is presented on the right panel of figure 2-1). These two planes can be used to roughly discriminate between field and galactic stars. The errors in photometry can mimic the presence of contaminant stars.

In this work I used the photometric catalogue with about 330000 stars in the direction of the Sculptor dwarf galaxy covering $\sim 2deg^2$ around its center which includes stars $28 > V > 8$ from the tip of the red giant branch of Sculptor and past the MSTO. I use the CMD showed in Figure 1 by Martinez-Vazquez et al. 2016 [10], which was provided to us by private communication. The stars were observed in a span of almost 24 years using several ground based telescopes and instruments and have magnitudes in the U,B,V,R,I bands[3]. The details on the data acquisition, reduction and extraction procedure can be found in Martínez-Vázquez et al. 2016 [10].

The plots on the figure 2-1 show the evolved evolutionary phases of stars in the Sculptor dwarf galaxy. The MSTO is not visible because it is too faint to observe with the current spectroscopic facilities and the plot was truncated to highlight evolutionary phases relevant for this work. In the following paragraph I will briefly discuss the evolutionary phases and only focus on the evolution of stars with masses

[1]Main-sequence turn-off refers to a locations on the color magnitude diagram where stars have almost completely exhausted the hydrogen in their cores and the hydrogen fusion in the layer surrounding the core becomes the main source of the stellar luminosity. It can be used as an age indicator once the distance, reddening and metallicity of the stellar cluster are known.

[2]Color-color diagrams are especially useful to discriminate between coeval stars of different metallicity, because, in the absence of extinction, color is independent on the distance. So the only parameters that can affect the position of the stars on the CC plane are metal content and reddening.

[3]Not all the stars have their photometric magnitudes measured in all the bands.

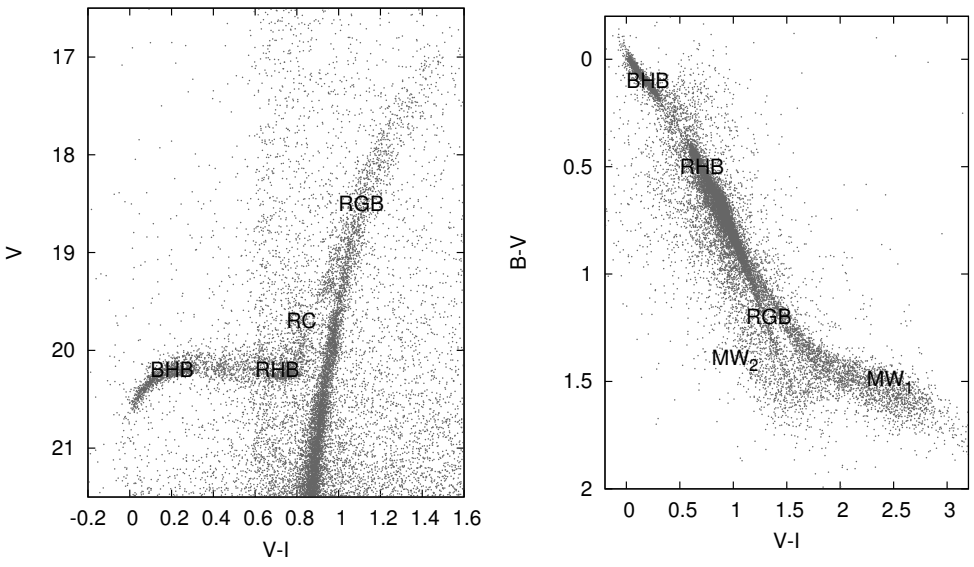

Figure 2-1: The color-magnitude diagram and the color-color plot made using $\sim$ 20000 stars from the total photometric catalogue. The stars presented have magnitudes measured in all three bands (B,V and I) and the V-band magnitude is brighter than 21.5. The most relevant and prominent evolutionary phases of Sculptor stars are also marked on both plots.

$0.5M_{\odot} < M < 5M_{\odot}$.

Following the main sequence phase (MS), where the location on the CMD is determined primarily by the mass of the star and the main source of stellar luminosity is core hydrogen fusion, the stars begin to burn hydrogen in the shell surrounding the inert helium core. The position of the evolved star along the red giant branch is mainly determined by the mass of the helium core. The stars spend most of their lives on the main sequence and the following evolutionary stages are orders of magnitude shorter. Owing to increase in the mass of the helium core the luminosity of the star increases and all stars start climbing the RGB until the condition for helium core burning is met ($M_{He-core} \sim 0.5M_{\odot}$).

The stars burning helium in the core are located on the horizontal branch. Depending on the initial mass of the star, its metallicity and mass loss along the RGB the stars with thick envelopes ($M_{env}/M_{tot} \sim 0.4$) populate the red horizontal branch (RHB) and those with thinner envelopes ($M_{env}/M_{tot} \sim 10^{-4}$) populate the blue hori-

zontal branch (BHB). These stars are associated with old stellar populations because it takes $\tau \sim 10Gyr$ for stars to evolve from the main sequence to the HB and so they are tracers of the oldest stellar population formed in any stellar system. Sculptor, that shows an initial burst and then an extended period of star formation, has in addition to the prominent HB also red clump (RC) stars. These helium core burning stars have higher masses and their progenitors have shorter hydrogen core burning phase than the HB progenitors stars and are thus tracers of intermediate age stellar populations. The progenitors to the HB and RC stars, the RGB stars, are a mixture of old and intermediate age stellar population depending on the mass of the progenitor main sequence (MS) star.

The importance of these tracers lies in the time of their formation. As they were all formed at different times and can be separated on the CMD (as seen on the figure 2-1) individual tracers can be used to study, among others, the distribution of dark matter and the history of interaction with the host galaxy.

The CMD, as seen on the left panel of the figure 2-1, also includes field stars, those belonging to the thick and thin disk as well as the halo of the Galaxy. These stars have different metallicity compared with Sculptor stars and are, therefore, located in a different region on the color-color plane on the right panel of the figure 2-1. The MW_1 stars belong to the Galactic thick disk and halo, with lower metallicity, and MW_2 stars belong to the thin disk of the Galaxy and have, on average, higher metallicity than Sculptor stars.

2.2 Spectroscopic Data

The error of the radial velocity measurement has the strongest dependence on the spectral resolution. The resolution is defined as:

$$R = \frac{\lambda}{\Delta\lambda} \tag{2.1}$$

here $\Delta\lambda$ stands for the dispersion per pixel of the spectrograph at the wavelength λ. Low resolution measurements will have intrinsically larger uncertainties and their accuracy can be evaluated by comparing them with higher resolution measurements. Hence, in order to build the largest, most homogeneous data set of line of sight velocities, samples of different degrees of precision need to have significant overlap.

The spectroscopic data set for which pre-reduced 1-dimensional spectra were available in the online ESO archive[4] in the Summer of 2016 and were used in this work will be presented in this chapter. Spectra are available in the *table fits* format with different table structure for every spectrograph.

The European Southern Observatory has a number of observation sites with Paranal in Chile being one of them. The Very Large Telescope - VLT with the diameter of the mirrors $d = 8.2m$ utilizing adaptive optics resides there. High altitude, low humidity and seclusion make this site particularly good for high resolution spectroscopy and other high precision observations that require long exposure times with stable atmospheric conditions. Several instruments, both for photometric and spectroscopic studies, are mounted in the foci of the 4 telescopes comprising the VLT. UT2 - Kueyen unit host the FLAMES[5] spectrograph at the Nasmyth A platform with a field of view of over $25'$ and UVES[6] at the Nasmyth B focus. Other instruments are also mounted onto this telescopes but only these two are relevant for this work.

2.2.1 Compiling a Catalogue of Spectroscopic Targets

Using the online platform[7] I looked for all the spectra in the direction of the Sculptor dSph. I used a box size of 1^o around the central coordinates of the galaxy, as presented in the table 1.1. I searched for all the observational programs that targeted Sculptor and disregarded spectra taken for other purposes (like studies of Lyman-α forest using

[4] All spectra collected at the ESO facilities are extracted and corrected for instrumentation effects by an automatic pipeline. Most of the spectra taken by ESO operated spectrographs are available science grade as either *phase3*, instrumental effects removed and extracted spectra, or *phase1* where spectra are only corrected for instrumental effects and are not extracted. These are available at http://archive.eso.org/cms.html.

[5] Fibre Large Array Multi Element Spectrograph

[6] Ultraviolet and Visual Echelle Spectrograph

[7] `http://archive.eso.org/eso/eso_archive_main.html`

quasars). Spectrographs that have been used to obtain spectra of the Sculptor dwarf galaxy were (presented in descending order of their resolution):

- UVES\ECHELLE(*) $R \sim 40000$
- UVES\FLAMES $R \sim 30000$
- GIRAFFE\high resolution(*) $R \sim 20000$
- GIRAFFE\low resolution(*) $R \sim 6000$
- FORS1 $R \sim 1500$
- FORS2 $R \sim 800$
- VIMOS $R \sim 600$

Among them, only the three marked with asterisk (*) had spectra processed also by the automatic pipelines of the *Phase3* data release.

The coordinates FK5 (ep=J2000) of every object are written in the header of its *fits* file and in order to create a list of stars from the list of spectra I used the program *TOPCAT*[8]. This astrophysical program was written for the purpose of manipulating tables and astronomical catalogues and has built-in routine that matches objects by their coordinates. The coordinates from all the spectroscopic subsets were compiled into one list in order to discern which spectra belong to each star, thereby creating a list of the spectroscopic targets.

The criteria for the maximal distance between two spectra, along the great circle, that still belong to a single star was first set to $1''$, since the aperture size of the fiber used by FLAMES (that feeds the light to GIRAFFE) is $1.2''$ and slit size of UVES/ECHELLE is around $1''$. To make sure that all the spectra were associated with their star and any slight misalignment of the fiber or the intrinsic change in position of the star over the years did not affect the matching I allowed the minimal distance to be $2''$ and then $3''$. The program automatically matches the best stars so there is no possibility of one spectra being assigned to two stars. The aforementioned increase in the maximal allowed distance did not reduce the number of stars and

[8] Tool for OPerations on Catalogues And Tables available online `http://www.star.bris.ac.uk/~mbt/topcat/`

as such I used the first criteria to build a catalogue of targets and evaluate overlap between stars that have spectra from different spectrographs.

Similar procedure was used also to match my list of spectroscopic targets with the photometric catalogue. Since there are more photometric targets per deg^2 than the spectroscopic ones, I had to pay special attention to possible double matching of the star for which two photometric stars were found within $1''$. This was especially important for the GIRAFFE high resolution sample, since the main targets for observation were selected in the dense center. In most of the cases the position on the CMD allowed me to discriminate between real and falsely matched stars, since those were mainly located below the detection limit (V<18.5) of the high resolution gratings.

2.2.2 UVES - ECHELLE

Is a cross-dispersed echelle spectrograph optimized for high resolution and sensitive from the atmospheric cut-off at $\sim 300nm$ to the limit of the charge-coupled device - CCD at $\sim 1100nm$. The limiting magnitude ranges between the 17th and the 19th magnitude depending on the atmospheric conditions, lunar phase and the investigated wavelength range. This limitation means that only the brightest part of the RGB of Sculptor can be investigated with this instrument. Split into red and blue arms there are several optical filters and gratings available for the spectrograph depending on the observed wavelength.

Grating	Filter name	$\lambda\lambda$ [Å]	R	$\langle SNR \rangle$	No. spectra	No. objects
CD#2	HER_5	$3280 - 4565$	40970	6.1	49	7
CD#3	SHP700	$4720 - 6840$	42310	11.5	64	12
CD#4B	BK7_5	$5650 - 9465$	34540	19.8	4	1
CD#4B	OG590	$6650 - 10255$	42310	7.0	12	1

Table 2.1: Table with the instrumental set-up specifications for the UVES *ECHELLE* spectrograph relevant for this work together with the average SNR, number of spectra and objects.

The table 2.1 summarizes the specifications of the UVES set-up that were used in order to obtain the spectra of candidate Sculptor stars as well as the number of

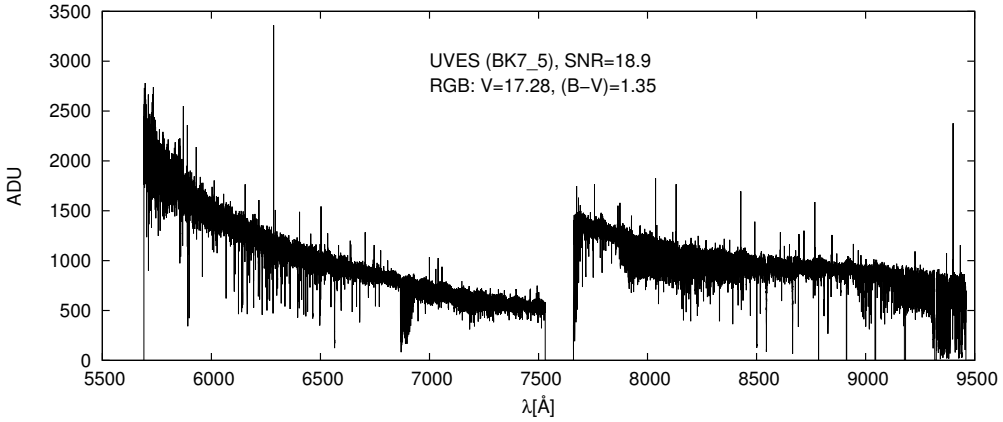

Figure 2-2: Example pre-reduced UVES 1D spectrum in BK7_5 filter.

spectra and stars. Information on the grating and the filter used in observation as well as the wavelength range, resolution and signal to noise (SNR) were taken from the header of the *table fits* files. There are, on average, 7 spectra per object in every grism (combination of grating and filter) with an average $\langle SNR \rangle = 11$.

As can be seen in the table 2.1, the relatively wide wavelength range ($\lambda > 1200$Å) and high resolution mean that only one object can be observed at the time with long integration time to achieve sufficiently high SNR. That is why only 13 stars have been observed in the Sculptor dSph using this instrument. An example of pre-reduced spectra is presented in the figure 2-2 and the distribution of the targets is presented on the plots in the figure 2-3.

In total, 13 stars have been observed with this spectrograph with, on average, 10 repeated spectra per object. The spectra were also taken in a span of 13 years, so any variation in radial velocities due to binaries or intrinsic pulsation of stars is averaged out. The main objectives of these observations was to measure the metallicities and as such the targets were not located only on the central region but span the whole galaxy as can be seen on the left plot of the figure 2-3. Photometric magnitudes are available for all but one star and their position on the CMD is depicted on the right plot of the figure 2-3.

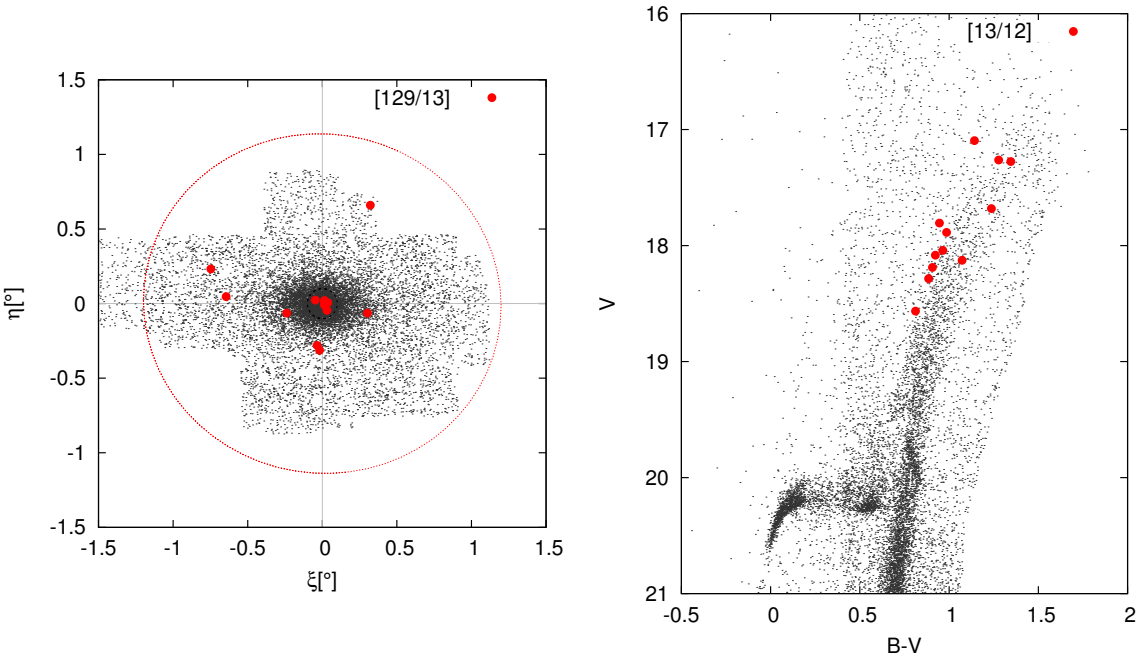

Figure 2-3: The distribution of UVES targets across the galaxy and on the color magnitude diagram. The black circle corresponds to the core radius and the red ellipse were drawn using the parameters from §1.4. The numbers in the bracket of the left plot correspond to the [# spectra / # objects] and on the right plot to the [# objects / # displayed objects].

2.2.3 GIRAFFE

The GIRAFFE spectrograph has high and low resolution set-up and is particularly useful for spectroscopic observations of galactic and extragalactic fields, where targeted objects have large spatial extent. The resolution ranges between $R \sim 65000 - 5500$ and covers the whole spectral range $\lambda\lambda 3700 - 9000$Å. The light is feed to the gratings either with optical fibers - MEDUSA mode or IFU - integral field unit. Only the former was used to observe Sculptor.

High Resolution - GH

GIRAFFE high resolution grating has around 31 fixed set-ups available and 7 of them have been used to observe Sculptor stars. An example of GIRAFFE high resolution spectrum is presented on figure 2-4 and the table 2.2 summarizes the instrumental set-ups, with the number of spectra and objects in each grism. On average, there are 5.4 spectra per object in every grism with the average $\langle SNR \rangle = 16.2$.

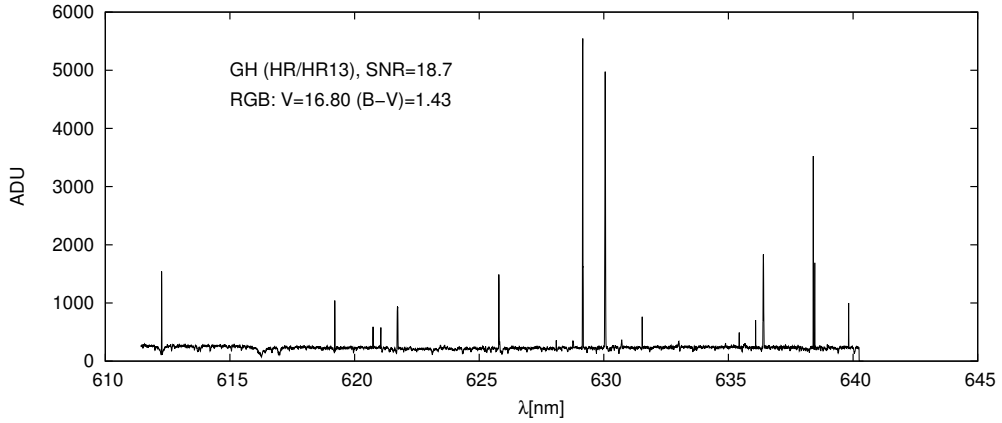

Figure 2-4: Example pre-reduced GIRAFFE high resolution 1D spectrum in HR/HR13 configuration.

Grating	ETC name	$\lambda\lambda$ [Å]	R	$\langle SNR \rangle$	No. spectra	No. objects
HRB	HR2	$3850 - 4050$	22000	3.7	765	87
HRB	HR7A	$4700 - 4980$	19000	10.1	420	106
HR	HR10	$5330 - 5620$	20000	16.5	232	116
HR	HR13	$6110 - 6400$	24000	20.2	345	116
HR	HR14A	$6380 - 6630$	17000	15.1	696	116
HR	HR15	$6590 - 6960$	19000	25.4	232	116
HRB	HR22A	$8960 - 9420$	24000	22.2	1236	103

Table 2.2: Table with the instrumental set-up specifications for the GIRAFFE high resolution spectra used in this work. The last two columns include information on the number of spectra and objects in each filter and grating combination.

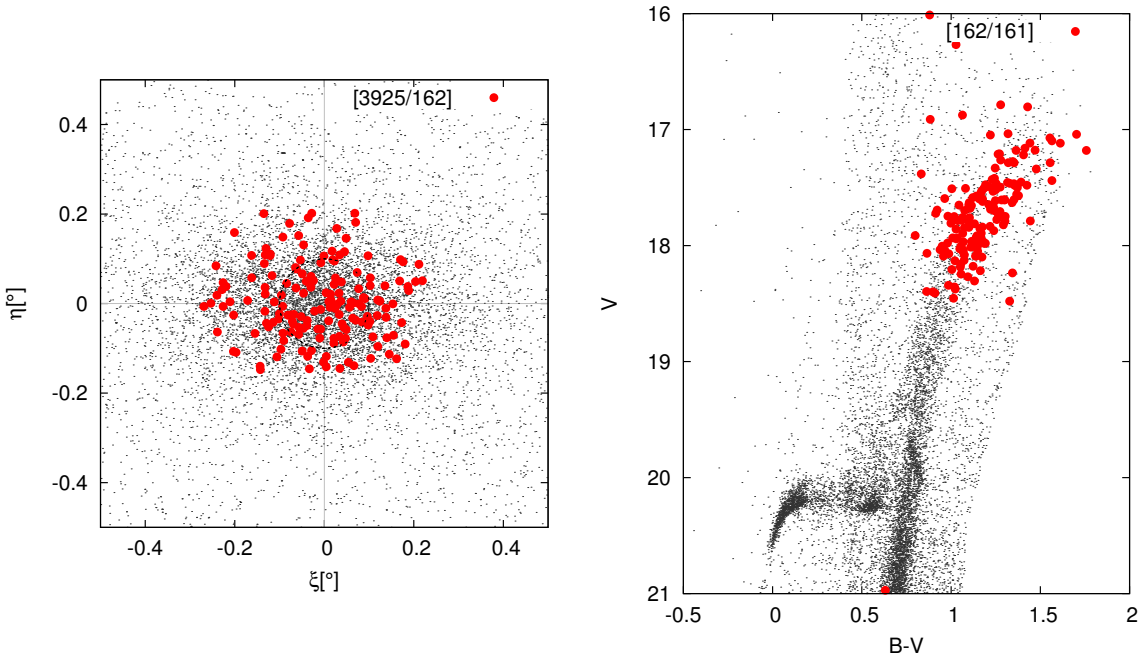

Figure 2-5: Distribution of stars with GIRAFFE high resolution spectra across the galaxy and on the color magnitude diagram. The black circle corresponds to the core size of the galaxy as presented in §1.4. The numbers in the bracket of the left plot correspond to the [# spectra / # objects] and on the right plot to the [# objects / # displayed objects].

As seen on the left plot of the figure 2-5 the stars are mainly concentrated in the central region of the galaxy. Only bright targets (V$<$ 19, for Sculptor the limit is 18.5) can be observed with high resolution grating as can be seen from the distribution of candidate Sculptor stars on the right plot of the figure 2-5.

Low Resolution - GL

The terms *medium resolution* and *low resolution* will both be used in this thesis in reference to the GIRAFFE low resolution grating as it is also found in the literature. For the low resolution gratings there are 8 filters available to observe different spectral regions. All the spectra available in the direction of Sculptor used the **LR08** filter which transmits a wavelength range $\lambda\lambda \sim 8200 - 9400$Å and has resolving power of $R = 6600$ in the MEDUSA mode.

Wavelength region transmitted by the **LR08** filter covers two important and very useful systems of lines for radial velocity measurements. For stars with low surface

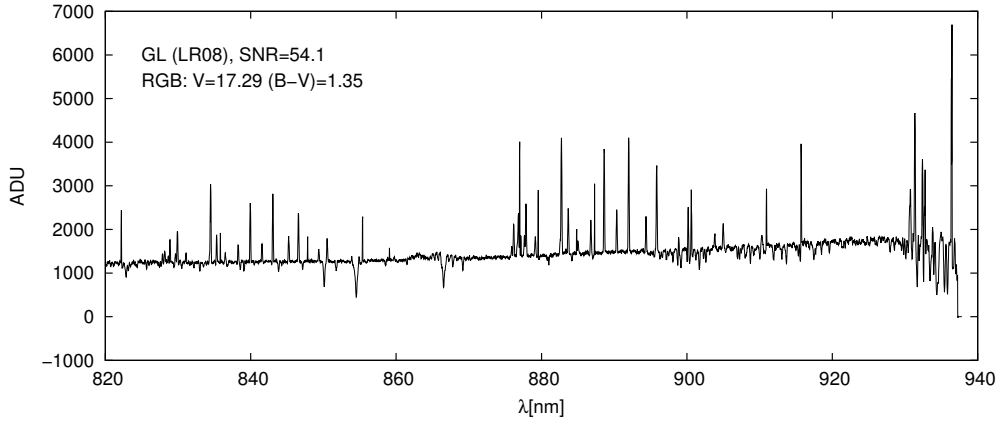

Figure 2-6: Example pre-reduced GIRAFFE low resolution 1D spectrum in LR08 filter.

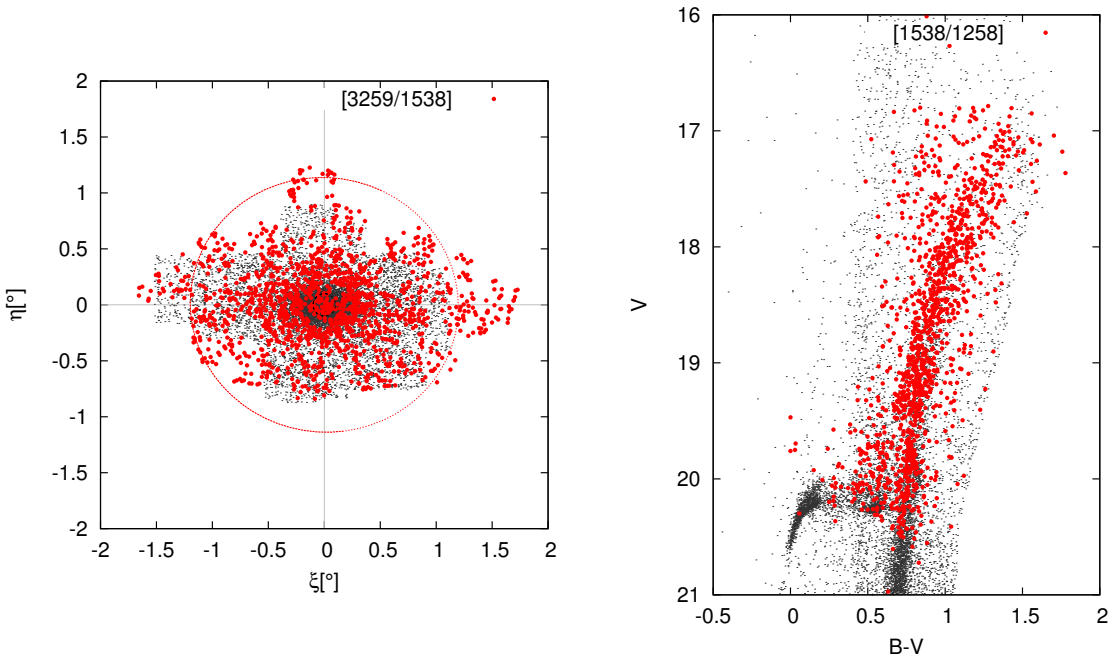

Figure 2-7: Distribution of GIRAFFE low resolution across the galaxy and on the color magnitude diagram. The black circle corresponds to the core radius and the red ellipse was drawn using the parameters from §1.4. The numbers in the bracket of the left plot correspond to the [# spectra / # objects] and on the right plot [# objects / # displayed objects].

gravity and temperature (red giant branch and red clump stars) calcium triplet - **CaT** ($\lambda 8498, 8542, 8662$Å) is visible in this filter and for the hotter blue horizontal branch stars the Paschen lines are.

This instrumental set-up was used for low resolution observations of Sculptor stars because it allows us to obtain radial velocities as well as metallicities, for the RGB and RC stars, by measuring the equivalent width of CaT lines. Compared with the high resolution samples the lower resolution of this instrumental set-up results in shorter integration time and fainter limiting magnitude (V$<$20.5). As 132 fibers of FLAMES can simultaneously be feed in the spectrograph, this configuration was used to observe most of the stars in the sample I compiled. In total there have been 8 observational campaigns between 2004 and 2015 aimed at observing the Sculptor dwarf galaxy. In total they collected 3259 spectra for 1538 stars. An example of the spectrum is depicted on the figure 2-6 and the distribution of the targets is presented on the figure 2-7.

As can be seen on the left plot of the figure 2-7, the spectroscopic targets span the whole body of the galaxy and extend also beyond the tidal radius. Lower resolution also means that fainter stars can be observed. This sample includes the spectra of red giant branch stars all down to the horizontal branch. Color-magnitude diagram on the right plot of figure 2-7 shows that helium-core burning horizontal branch stars and red clump stars of the Sculptor dwarf galaxy are represented in the sample I compiled. The spatial extent and the magnitude range of the sample is crucial in building a homogeneous measurement.

2.3 Overlap Between Different Spectrograph

After downloading all the 1-dimensional spectra from the online archive, I cross-matched the spectra from different spectrographs and gratings in order to understand whether there is sufficient overlap between low and high resolution spectra. The overlap is essential in order to constrain the systematics of low resolution measurements.

The largest error in determining the center of an absorption line, from which the

radial velocity is determined, is directly related with the step size of the spectra: $\Delta v = c\frac{\Delta\lambda}{\lambda}$ [9], where c stands for the speed of light in vacuum. From the equation it is evident that the smaller the wavelength bin of the spectra the lower is the uncertainty with which the center of the line can be determined. For the above discussed spectrographs the maximal error of the radial velocity measurement, if only one line is used, is reported in reported in the table 2.3.

spectrograph	$\Delta\, rv\, [km/s]$
UVES	1.7 – 2.5
GIRAFFE high res.	2.3 – 3.2
GIRAFFE low res.	6.9

Table 2.3: Maximal error of the $v_{l.o.s.}$ due to the size of the wavelength bin.

When more absorption lines are identified and their center is measured, the error is reduced as the $\frac{1}{\sqrt{n}}$, where n is the number of lines used for the radial velocity measurement. The bulk of the spectra come from the largest grating - LR08 and have, on average, only 2 spectra per object. The UVES sample contains, on average, 11 spectra per object and the high resolution GIRAFFE around 24. Measurements from the same star using multiple spectra allows us to further reduce the error as well as investigate possible systematics from different grating and filter combinations.

With so many spectra per individual object as well as higher resolving power the measurements from UVES can be used to investigate the accuracy of GIRAFFE high resolution measurements and both are needed to constrain the $v_{l.o.s}$ obtained from low resolution spectra. This procedure stands at the base of my project to provide the most homogeneous and accurate radial velocity measurements.

The overlap between different sub-samples is summarised in the table 2.4 and is discussed in more detail in the following paragraphs.

UVES and GIRAFFE High Resolution As can be seen on the figure 2-8 and table 2.4, almost half of the UVES stars were also observed with high resolution GIRAFFE and those are located mainly in the central region and in the brightest

[9] Here $\Delta\lambda$ corresponds to the rebinned difference in wavelength between two adjacent points, which is smaller than the dispersion per pixel of the spectrograph.

	# spectra	# stars	UVES	GH	GL
UVES	129	13	x	5	11
GIRAFFE high res.	3925	162	5	x	117
GIRAFFE low res.	3259	1538	11	117	x

Table 2.4: Overlap between different spectroscopic sub-samples.

part of the RGB. Due to the small number of overlapping stars and relatively small difference in the resolution the statistical significance of such a comparison is somehow limited. It will, however, enable me to investigate possible variability of these stars.

GIRAFFE Low and High Resolution Almost all of the stars present in the high resolution sample are also present in the low resolution. These complementary observations enable high precision measurements of radial velocities from the high resolution sample to investigate the accuracy of the low resolution measurements. Due to the distribution of high resolution targets, the overlapping stars are only located in the central region of the galaxy and only cover the brightest part of the RGB.

GIRAFFE Low Resolution and UVES The spectroscopic targets of UVES cover also the galactic regions beyond the central region. Therefore, they can be used to investigate the accuracy of low resolution sample closer to the tidal radius of the galaxy, providing a complementary test to the high resolution overlap.

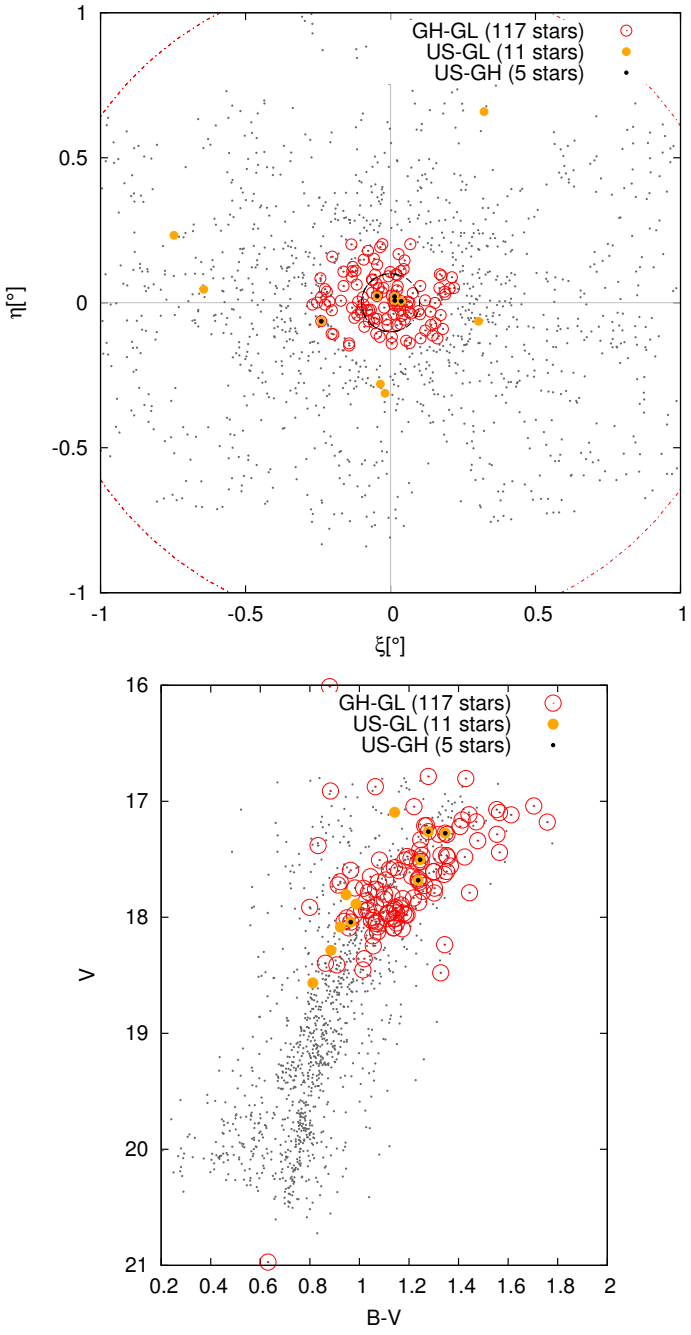

Figure 2-8: Spatial distribution as a function of galacto-centric distance of overlapping stars is presented on the upper panel and the bottom panel shows the corresponding CMD. The grey points on both plots represent GL sample for reference. The red ellipse on the upper plot corresponds to the tidal radius and black circle to the core radius of the Sculptor dSph. The open red circle represent the position of stars with both GIRAFFE high and low resolution spectra, the orange filled circles the distribution of stars with UVES/ECHELLE and GL spectra and with the black dots stars US and GH are depicted.

Chapter 3

Data Reduction and Line Identification

After downloading the spectra discussed in the previous chapter they had to be prepared for the radial velocity measurements. In this chapter I will first present the *Phase-3* data release for UVES/ECHELLE and GIRAFFE/MEDUSA spectrographs, followed by a description of the final reduction steps I performed using *IRAF*[1] as well as the line identification. The program I used for radial velocity measurements requires a list of absorption lines to be identified in the spectra and their central wavelength computed by fitting a Gaussian function. The program itself will be discussed in greater detail in the following section. The spectral features to be included in the line lists depend on the spectral type of the star, its surface temperature, metallicity (as they affect the population of the excitation levels of atoms and ions) as well as any peculiarities of the spectra in a given wavelength range. The brief summaries of the line lists are summarized in the tables in this chapter while the complete line lists can be found in the appendix B. The aforementioned appendix also includes examples of 3 lines for each grism that follow the line list. First panels depict the reference line, second an example of a strong line and the third panel an example of a weak line present in the line list. The plots are centred at the rest wavelength of the transition and the Gaussian function is fitted to the shifted absorption line. The wavelength

[1] Image Reduction and Analysis Facility, `http://iraf.noao.edu/`

shift is computed from the radial velocity of the spectrum measured with the *ROSSA* programme (the rv is presented in the figure, together with the information on the grism, spectrum and the star).

All the final reduction as described in this chapters was performed manually, without developing a program. This was deemed to be preferable owing to the large number of different instrumental set-ups used to obtain the spectra. The number of spectra with a given instrumental set-up is on average ~ 600 and with 12 individual grating/filter configurations developing and testing the automatic procedure would require more time than performing the final reduction steps manually. In that way the number of spectra that can be used for radial velocity measurements can be maximized.

3.1 Prereduction

Shortly after the data acquisition, the spectra obtained by the ESO telescopes are made available both pre-reduced and in raw form on the online archive, first for the proponents and after one year also for the public. In this section I will present UVES/ECHELLE and GIRAFFE/MEDUSA *Phase3* data release description and the process of transforming multi-column binary tables *-table-fits* to one dimensional spectra that can be used by most of the packages in the *IRAF* facility.

The spectra are also available in raw form if there is a special science goal for which more careful and tailored calibration needs to be performed which cannot be achieved with an automatic pipeline.

3.1.1 UVES Spectra

On the Status of the UVES Spectra

The discussed data release[2] is relevant for UVES spectra of **point sources** taken in **ECHELLE mode**. The cross dispersion - ECHELLE type spectrograph uses

[2]Version presented here was published on the 22.06.2016, version 1.3 `http://www.eso.org/observing/dfo/quality/PHOENIX/UVES_ECH/processing.html`

high diffraction orders in order to increase the resolution and the wavelength range. The resulting two dimensional spectra are dispersed by wavelength in one axis and by diffraction order in the other axis. In order to produce single spectra these overlapping orders have to be merged during the data reduction process.

Before the extraction of orders the spectra have to be corrected for instrumental signatures. **Flat-field** correction compensates for the non-uniform light exposure of the detector and **de-biased** spectra have thermal-noise signature, due to non-zero temperature of the telescope and the CCD, removed. These continuous data releases use certified master calibration images that are the closest in time to the observing run of the processed spectra. These are the first two steps in the automated pipeline processing. Afterwards, the Echelle orders have to be traced using continuum arc lamp and merged. Wavelength calibration solution is obtained using ThAr arc lamp and applied to the spectral data. Finally, the merged, wavelength calibrated spectra are rebinned.

Upon extraction, the high spikes in intensity corresponding to the impinging cosmic ray[3] are removed by using optimal sky background as a reference. If a master response curve is available, flux calibrated[4] spectra are also included in the binary table in physical units.

The output of the pipeline are converted to standard 1-dimensional binary table *-table fits*. The data products processed by the automatic pipeline are considered ready for high resolution scientific research, such as radial velocity measurements and line profile studies.

Spectra presented in this data release have not been corrected for telluric absorption or emission lines originating in the atmosphere. While the heliocentric[5] and

[3] Cosmic rays are high energy particles, usually electrons or photons that introduce strong spikes in intensity owing to their high kinetic energy. They are stochastic and can be removed by setting appropriate flux threshold.

[4] The flux calibration is in general not sufficiently accurate to allow for detailed spectrophotometric studies, however rough energy distributions can be obtained.

[5] Helio- and barycentric correction vary around $\sim \pm 30 km/s$ depending on the time of the year and the position of the target in the sky. Heliocentric system has origin in the center of the Sun, while the barycentric system is a bit shifted, though still close to the surface of the Sun, and it corresponds to the barycentre of the planetary system. The two values differ by less than $0.01 km/s$.

barycentric velocity correction are included in the header of the individual spectra, the spectra themselves are not shifted in wavelength to compensate for the motion of the Earth around the Sun. The corrections are logged in the header with the key words : *VRAD BARYCOR* and *VRAD HELICOR*. Upon determining radial velocity from each spectrum, barycentric or heliocentric correction have to be applied.

The light from the RED arm (corresponding to gratings CD#3 and CD#4B as presented in table 2.1) of the UVES spectrograph is feed onto two CCD detectors. This results in unavoidable gap as the spectra are merged into one with different wavelength sampling. Another set of gaps appears in the spectra at wavelengths longer than $880nm$. These are artefacts of the flat fielding algorithm of the pipeline and can be prevented by manual reduction.

The columns structure of UVES/ECHELLE binary tables is as follows:

1. **WAVE** - Wavelength in Ångström
2. **FLUX_ REDUCED** - extracted and wavelength calibrated science spectrum
3. **ERR_ REDUCED** - corresponding error
4. **BGFLUX_ REDUCED** - extracted and wavelength calibrated sky signal
5. **FLUX** - FLUX_ REDUCED in physical units of $10^{-16} erg/cm^2/s/$Å
6. **ERR** - ERR_ REDUCED in physical units of $10^{-16} erg/cm^2/s/$Å

Creating *fits* Files

In order to reduce the number of fits files stored at the ESO archive it is preferable to save all the information on the spectrum in a binary table. This format, however, is not compatible with all the available packages of the *IRAF* program. Therefore, in order to completely prepare the spectra for radial velocity measurements, the first two columns of the spectra had to be extracted and spectra from the right arm split into two individual spectra so that radial velocity measurements are not affected by the rebinning procedure.

To manipulate with this image format, the special external package *tables* is available for IRAF as a part of the *STSDAS* package[6]. The routine *ttools.tprint* prints the

[6] `http://www.stsci.edu/institute/software_hardware/tables`

content of the *table fits* file into an ascii file with a given number of row characters.

After obtaining the ascii files of all the spectra I used the bash command *awk* in order to copy only the first and the second column (wavelength and intensity in arbitrary units). In this work I used the flux in arbitrary units even though most of the UVES spectra I used had the flux calibrated column. This decision was motivated by the fact that every additional step in reduction procedure can introduce errors and the flux calibration is not needed for radial velocity measurements. Spectra from the red arm were then split into two (part **A** and part **B**) using the bash command *sed*. The beginnings and ends of both RED and BLUE arm spectra were also cut. In the bordering regions the extraction procedure can produce spurious effects, that can be removed without the loss of information. The wavelength regions for splitting were determined by displaying the spectra using the *gnuplot* program.

Finally, the cropped ascii spectra were converted into *fits* files using the *IRAF* command *noao.onedspec.rspectext* and setting the wavelength to be interpolated from the spectra. The one dimensional *fits* files contain only the information on the intensity, whereas, the information on the wavelength is stored in the header of the file as initial wavelength and step size. After finishing this procedure I performed series of tests, comparing the final with the original spectrum, to make sure that the my procedure did not introduce any shifts that would produce an error on the radial velocity measurements.

3.1.2 GIRAFFE Spectra

On the Status of the GIRAFFE Spectra

The discussed data release[7] is relevant for the FLAMES/GIRAFFE spectrograph in MEDUSA mode that allows for simultaneous observations of up to 132 targets. Initiated in April 2015, the open stream release policy of the GIRAFFE *Phase3* Data Release ensures that a month or two after observing the spectra will be available in binary table format with instrumental signatures removed and spectra extracted.

[7]Version presented here was published on the 21.09.2015, version 1.2 `http://www.eso.org/observing/dfo/quality/PHOENIX/GIRAFFE/processing.html`

The raw data are processed using the latest pipeline version and master calibration files that were taken closest in time to the observation run. The raw spectra are corrected for dark-current or thermal noise - **de-biased** and **flat-fielded** in order to correct for non-uniform illumination of the CCD detector owing to fringing and fiber-to-fiber transmission. The spectra are then extracted, wavelength calibrated and shifted for heliocentric correction. The correction is stored in the header together with the barycentric and geocentric correction (under header key words: *HELICORR, BARICORR, GEOCORR*). Unlike UVES no flux calibration is performed and the structure of the *table fits* file differs from that of the UVES spectrograph. The 1-dimensional spectra processed in this way and available online are expected to be useful for any kind of medium resolution spectroscopic research such as abundance and radial velocity measurements.

Since the GIRAFFE in MEDUSA mode can simultaneous observe 132 sky positions, a couple of fibers are always dedicated to the sky. The downloaded packet of spectra also includes sky spectra reduced in the same way as the object spectra, with references between the object and the closest sky spectra. This is important as no correction of telluric emission or absorption lines originating in the atmosphere has been performed.

Same as with the UVES spectra the files also include a column with pixel to pixel error estimate, which is used to build the SNR column. The final output of the automated pipeline is a binary *fits* table with 4 columns.

1. **WAVE** - wavelength in nm, corrected to heliocentric system
2. **FLUX_ REDUCED** - extracted and wavelength calibrated science spectrum, signal in counts not physical units
3. **ERR_ REDUCED** - corresponding error, signal in counts not physical units
4. **SNR** - signal-to-noise ratio that is a simple division between the 2nd and the 3rd column

The 4th column - SNR is provided only for convenience and its median value is included in the header of the *fits* file under the key word: *SNR*.

Creating *fits* Files

The *table fits* have to be again converted to the standard one dimensional spectra in order to perform the final reduction and, later, the radial velocity measurements. The process was similar to the one presented in §3.1.1 for the UVES spectra, without the need for additional step of cropping the spectra. After converting the spectra to ordinary *fits* files, 10 spectra were randomly selected. Using *splot* task both in *tables* and *noao* packages of *IRAF* a Gaussian profile was fitted to several selected spectral lines to investigate possible errors by the conversion process. The fitting was performed with original and processed spectra and a nominal difference of $\Delta\lambda \sim 0.003nm$ was found. It is not possible to say that this difference originates in the transformation process or in the fitting of the Gaussian function to the line profile. The error with which the center of the line is computed, given by the *splot* task, is larger than the aforementioned difference. With the *fits* files created and spectra rebinned by the *rspectext* routine, the spectra were separated by the grating/filter combination to be separately normalized.

3.2 Reduction - UVES

With the prepared 1-dimensional *fits* files the next step was to normalize the spectra by fitting the continuum and identifying strong, unblended and isolated lines for radial velocity measurements.

3.2.1 Continuum Normalization

Continuum normalization has to be performed in order to emphasize the spectral features and enable Gauss profile fitting to the lines. The continuum of a spectrum would in ideal case correspond to the Planck function of the black body spectrum at temperature of stellar surface temperature. However, the instrumental effects and extraction procedure can result in uneven continuum that needs to be individually fitted. Special care was devoted to the spectra that include broad lines, such as the

Balmer lines. Selecting a polynomial function with very high order, to fit the continuum, can result in deforming the line, thereby preventing accurate measurements.

A special task in *noao* package is present in order to perform the normalization. Several parameters have to be adjusted in the *noao.onedspec.continuum*[8] task, also the type of the fitting function. There is a slight difference between the 4 available fitting function as some are more suited for objects with broad emission/absorption lines than others. For my sample, I used *spline3* function and found that it gives satisfactory results. The rest of the parameters I used are presented in the table 3.1. The parameters not discussed in this description were left at their default settings as presented on the description web site.

parameter	value
type	ratio
function	spline3
order	10 - 15
low_reject	1 - 2
high_reject	3 - 5
niterate	10 - 12

Table 3.1: Table of *continuum* settings for UVES spectra.

The table 3.1 summarizes the most important parameters and the values I used in the continuum task. The resulting spectrum was a ratio of the initial spectrum and the fitted *spline3* function. The low and high reject parameters set the sigma threshold above which the points are rejected from the fitting process. With the initial fit to the spectrum, the task computes the residuals and rejects values greater than the standard deviation of the residuals as defined by the low and high reject parameters. Then it refits the function and recomputes the residuals. The number of iterations of the clipping procedure is defined by the last parameter in the table 3.1.

With the commented choice of parameters, I found good fitting, which resulted in a flat spectrum with continuum at level 1. Spectra reduced in this way were then used together with a template spectra to identify the lines for the radial velocity measurements. Finally, all the spectra were converted back to the ascii format using

[8] `http://stsdas.stsci.edu/cgi-bin/gethelp.cgi?continuum`

the *wspectext* task in *IRAF*. A selected spectrum in the BK7_5 filter is presented both reduced and pre-reduced on the figure 3-1 in order to show the reduction process as discussed in this section.

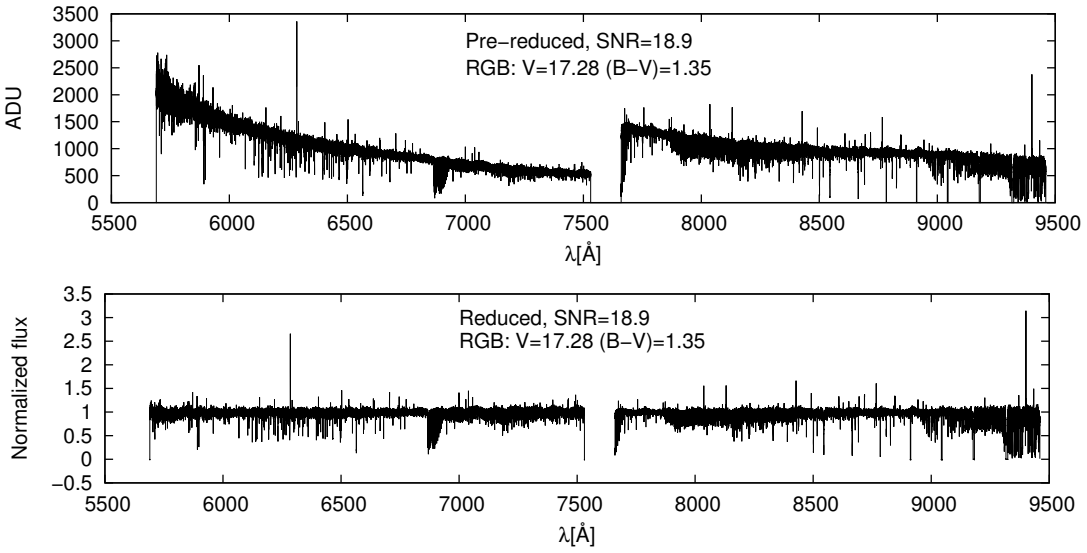

Figure 3-1: Example pre-reduced UVES spectrum on the top panel and reduced spectrum used for radial velocity measurements on the bottom panel. The spectrum was taken using the BK7_5 filter.

3.2.2 Line Identification

As seen on the right plot of the figure 2-3, the stars with the UVES high resolution spectra occupy the brightest portion of the color magnitude diagram. From their position I roughly estimated the surface temperature, gravity and microturbolence velocity, combining the information on the metallicity of Sculptor stars [3],[11] I obtained synthetic spectra for RGB Sculptor stars[9]. A selected synthetic spectrum and associated line list, from which it was created, were just used as a reference to distinguish more clearly between the noise and a real absorption feature. The strength of lines and their presence were computed and combined using the *Moog* code[10] considering $T_{eff} = 5250K$, $log(g) = 1, 2$, $\xi = 0.3$, $[Fe/H] = -1, -2$.

[9] These spectra were originally created and used for the radial velocity measurements using *fxcor* task in *IRAF*. This procedure was ultimately found to produce systematic error in radial velocity measurements and another technique was adopted. The discussion can be found in appendix A.

[10] The code is available on `http://www.as.utexas.edu/~chris/moog.html`

Since the RED arm spectra had to be split in two pieces, 7 individual line lists were created for the Sculptor targets. It is preferable that as many lines as possible are included in the line list, although blended lines or week lines should be excluded as they can easily be mistaken for noise. These false line identification can reduce the precision of the measurements and with that in mind I compiled line lists that are included in the appendix B and a brief summary is presented in the table 3.2.

set-up	# of lines	id line
CD#2 (HER_5)	79	Hδ
CD#3 (SHP700) - A	47	Hβ
CD#3 (SHP700) - B	24	Hα
CD#4B (BK7_5) - A	32	Hα
CD#4B (BK7_5) - B	14	Ca II
CD#4B (OG590) - A	12	...

Table 3.2: Summary of the UVES line list.

The atmospheric wavelength of a line transition was used to create the line lists and the wavelengths for selected lines were verified by searching through the NIST database[11]. In the table 3.2, it is clear that the number of strong lines, that can be identified in the spectra decreases with increasing central wavelength of the grism. The strongest lines belong to the Balmer series, which were used as reference lines in radial velocity measurements.

3.3 Reduction - GIRAFFE

3.3.1 Continuum Normalization

Unlike UVES, GIRAFFE spectra are obtained by dispersing the stellar light onto the CCD only in wavelength resulting in one long spectrum spanning the whole detector. Therefore, they are less prone to uneven continuum as seen in the UVES spectra. However, some pipeline related problems, such as the presence of strong arc lines[12]

[11] `http://physics.nist.gov/PhysRefData/ASD/lines_form.html`
[12] Lines from the lamp used for wavelength calibration.

at wavelength beyond $\lambda \sim 700nm$, which can cause saturation and contamination of signal in the neighbour fibres, are known and have to be treated with care.

In addition, strong telluric lines are present in these spectra especially at longer wavelengths. Careful removal of these lines is beneficial for the radial velocity measurements. The sky correction will be discussed in the following section. First the continuum normalization of high and medium resolution GIRAFFE spectra will be presented.

High Resolution All the spectra in the grating/filter configuration, as presented in table 2.2, show either slight curvature or slope of the spectra. Otherwise the continuum is very flat. Some irregularities are present in the **HRB/HR22A** configuration, where the end of the spectra show spurious oscillating flux. Irregularities of these spectra at long wavelengths are a consequence of the pipeline procedure and can be ignored. These wavelengths are also subject to molecular bands originating in the atmosphere that can distort the shape of the fitting function if the order of the function is set too high.

Similar procedure as for UVES was applied for the GIRAFFE high resolution spectra in §3.2.1. While some parameters of the *continuum* task stayed the same (function and type), the final 4 parameters as seen in the table 3.1 changed slightly.

grating/filter	order	low_reject	high_reject	niterate
HRB (HR2)	5	1	3	10
HRB (HR7A)	5	2	3	10
HR (HR10)	5	2	3	10
HR (HR13)	10	2	2	10*
HR (HR14A)	10	2	3	10*
HR (HR15)	10	2	3	10
HRB (HR22A)	7	2	3	10*

Table 3.3: Table of *continuum* settings for GIRAFFE high resolution spectra. The instrumental set-ups marked with $*$ indicate the ones where additional weighted points had to be added at the end points of the spectra. This was needed only for around 10% of the whole sample of spectra.

In some grisms, the end points of the spectra had strong discontinuities, cut-offs or upturns in the flux. These irregularities caused problems in the continuum fitting

to the whole spectra. However, as they were only present on the end region, where no line was identifiable, I added additional fitting points on case to case bases in the interactive window of the *continuum* task. This was done by positioning the pointer and pressing the key **a** to add appropriate weight to the added point. The value I used was 100. This was necessary in roughly 10% of the sample marked with $*$ in the table 3.3 and was proven to be very effective without tampering with useful data points.

Medium Resolution The low resolution spectra were first cut to remove the final $10nm$ of the spectra. This range was strongly affected by the errors in the acquisition of the spectra and pipeline artefacts. However, since no usable lines were present at these wavelengths and it needlessly complicated the continuum fitting, such a cut was justified. Around 2% of the spectra also had discontinuities in the range of the CaT lines, due to the saturation from the arc-lamp lines. Such spectra were removed from further analysis - 69 spectra were removed.

Aside from the aforementioned irregularities no major problems were found in these spectra during continuum normalization and the procedure was similar as described for UVES and GH spectra. The table 3.4 summarizes the settings for the *continuum* task in normalizing GL spectra.

parameter	value
function	spline3
order	1 - 5
low_ reject	0 - 1
high_ reject	2 - 4
niterate	10

Table 3.4: Table of *continuum* settings for GIRAFFE low resolution spectra.

3.3.2 Removal of Telluric Lines

Even if in the case of the spectra from UVES this step was not necessary, for GIRAFFE spectra the removal of telluric lines represented an important step in order to prepare the spectra for the radial velocity measurements. At longer wavelengths,

the spectra become dominated by strong molecular bands originating in the atmosphere of our planet. The best possible correction for these molecular emission lines requires detailed understanding of actual atmospheric conditions and object position as well as additional sky emission spectra (either synthetic or taken together with the object spectra). However, such rigours reduction is essential in element abundance measurements but it is not needed in obtaining radial velocities.

As mentioned in §3.1.2, there are sky spectra available in the *Phase3* data release. The sky spectra were first subjected to the same reduction process as GIRAFFE spectra described in §3.1.2. The task *skytweak*[13] in *IRAF* was used to shift the normalized sky spectrum in wavelength, amplitude and scaling it to match the star spectrum. The task iteratively shifts and scales the spectra in order to minimize the residuals between the observed and the sky spectrum.

Selecting a test sample of $\sim$ 20 GIRAFFE spectra in HRB/HR22A and LR08[14] configurations, I used the *skytweak* task in order to clean the spectra of telluric lines and molecular bands. After manipulating the shift and scale only two spectra could be cleaned of the molecular features. Furthermore, additional absorption lines appeared in the rest of the tested spectra when the sky spectrum was subtracted. The presence of additional spurious lines due to the reduction procedure would corrupt the radial velocity measurements and the sky spectra were not used to remove the telluric emission lines and molecular bands.

Even if the sky spectra could not be used, the strongest emission lines still needed to be removed to ease the radial velocity measurements[15]. Removal of the strong emission lines makes the spectra more manageable and stellar absorption features are easier to recognize. Simple procedure of cleaning the lines above a set threshold from the fitted continuum was found to be sufficient for the radial velocity measurement.

[13] The documentation on the task: `http://iraf.net/irafhelp.php?val=skytweak&help=Help+Page`

[14] These have strong molecular bands in the regions where relevant absorption lines are present and were hence chosen to test the feasibility of the task.

[15] This step was essential when measuring the radial velocity using *fxcor* task, but not necessary for the *IDL* program used in the end. However, removing the strong emission lines made the process of identifying reference lines easier in the *IDL* program, which will be discussed in the next chapter §4.

This was performed using the *IRAF* task *images.imfit.lineclean*[16].

The task fits a continuum (the parameters for the fitted function are listed in the table 3.5), computes the residuals and their standard deviation σ. Points below and above the pre-set threshold are replaced by the fitted function. By setting the parameter **grow** to non-zero values, not only the outlier point is removed but also a given number of adjacent points. The procedure is iteratively repeated for a predetermined number of steps and not by a converging criteria, this leaves it up to the user to change the parameter **niterate** until the cleaning is satisfactory for the spectra and science that will be conducted with them.

High Resolution Since the spectra have already been normalized, the order of the fitted continuum could be safely set to low values. It was imperative that no absorption lines were removed, since most are stellar features. The lower threshold for rejected points was set very large as seen in the table 3.5. The parameters that have to be set are similar to those in the *continuum* task discussed in the previous section. The function for fitting was set to **spline3** and the value for **grow**=0. The parameters not discussed in this description were left at their default settings as presented on the web site. The bottom panel on the figure 3-2 shows a spectrum after the above steps were conducted to process the spectrum on the top panel of the figure.

grating/filter	order	low_reject	high_reject	niterate
HRB (HR2)	3	5	5	10
HRB (HR7A)	2	5	3	10
HR (HR10)	2	10	3	10
HR (HR13)	2	10	3	10
HR (HR14A)	2	10	4	10
HR (HR15)	2	10	4	10
HRB (HR22A)	2	10	4	10

Table 3.5: Table of *lineclean* relevant parameters GIRAFFE high resolution spectra that removed the strong lines without tampering with the absorption lines.

[16] `http://iraf.net/irafhelp.php?val=imfit.lineclean&help=Help+Page`

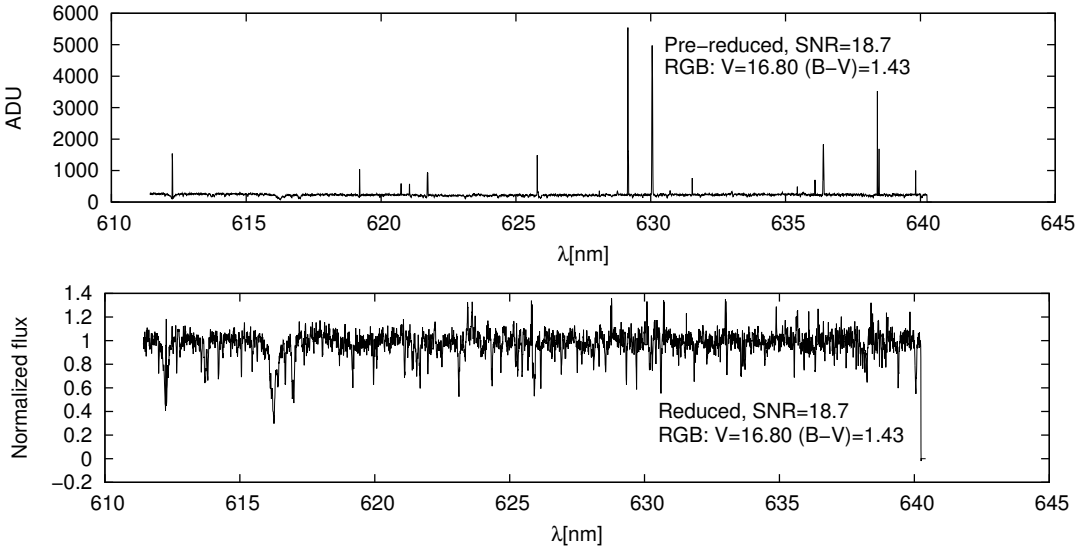

Figure 3-2: Example pre-reduced GIRAFFE high resolution spectrum, in HR/HR13 configuration, on the top panel and reduced spectrum used for radial velocity measurements on the bottom panel.

Medium Resolution The molecular OH and O_2 bands dominate the spectral region of the LR08 grating and the near-infrared (NIR) CaT lines. That is why additional efforts were made to try to remove the atmospheric features using synthetic sky spectra. From the header of the *fits* files the information on atmospheric conditions were extracted and a synthetic spectrum was created using the *TelFit* code available online[17]. The synthetic sky spectra were manipulated using *skytweak* to try and remove the molecular lines using individual sky spectra for the 6 selected LR08 spectra. Even though the synthetic sky spectra were created for each individual spectrum, the procedure only produced good results for one of them. For the others, additional absorption features appeared.

Since the use of either synthetic or observed sky spectra did not produce desired results and with no need for tedious correction, I also used the *lineclean* task to remove the strong molecular bands from the LR08 spectra. The best **order** of the fit was between 1 and 2, **low_reject** ranged between 10 and 20, **high_reject** between 4 and 6 and finally the optimal **niterate** was 10 as well as in GH spectra. The other parameters were set the same as for the high resolution spectra. An example of the

[17] `http://telfit.readthedocs.io/en/latest/`

reduction process is depicted on the figure 3-3. Top and bottom panels show the spectrum before an after the reduction process, respectively.

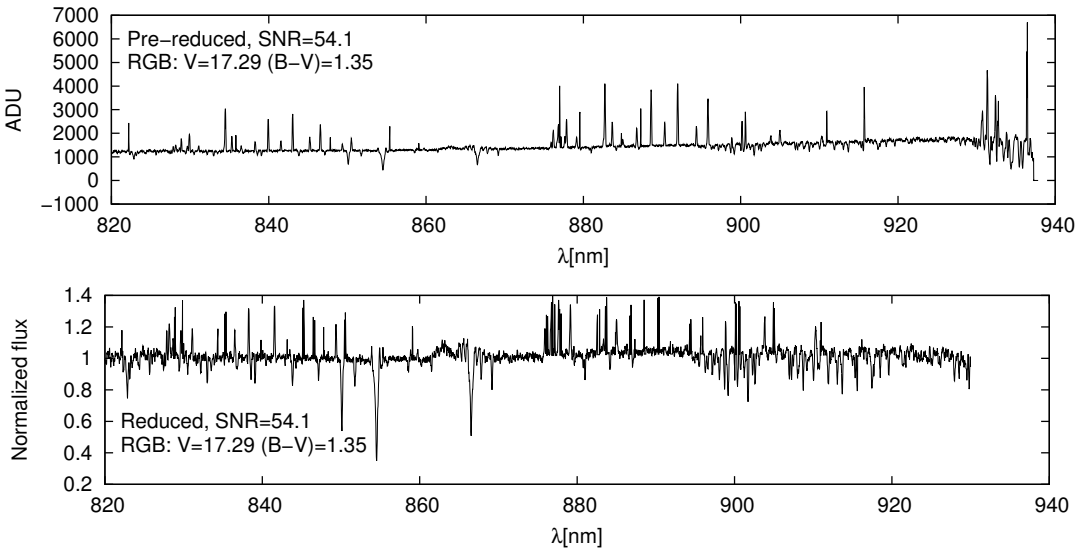

Figure 3-3: Example pre-reduced GIRAFFE low resolution spectrum in the filter LR08 on the top panel and reduced spectrum used for radial velocity measurements on the bottom panel.

3.3.3 Line Identification

Since I used the *lineclean* task in order to replace the strong emission lines with the fitted curve in the GIRAFFE spectra, the stellar lines used for radial velocity measurements should not coincide with the cleaned line. This would namely result in an error in determining the central wavelength of the absorption line. The procedure I used to identify lines in these spectra does not differ strongly from that presented for UVES spectra in §3.2.2. The same template spectra, degraded for GL to its spectral resolution, and line lists were used to identify the stellar absorption lines in a given grism.

High Resolution The distribution of high resolution targets across the color magnitude diagram presented on the figure 2-5 is similar to the distribution of UVES targets. Both occupy the brightest part of the RGB so that the stars in the GIRAFFE

sample have the same parameters as the ones in the UVES sample. Therefore, the same synthetic spectrum and the list of lines can be used[18].

The spectra in the HRB/HR2 configuration show only the calcium H and K lines that are not very prominent and these spectra have low signal to noise ratio ($\langle SNR \rangle \sim 3.7$). This wavelength region is primarily used in order to study the possible variability of stars. Since the exclusion of these spectra did not affect the number of objects with high resolution measurements, these spectra were removed from further analysis.

Special attention was placed on the spectra from the HRB/HR22A. There are, on average, 12 spectra per star in this configuration but the presence of telluric lines prevents any stellar line to be clearly identified. Since there are many repeated spectra, we investigated the possibility of combining the individual spectra and thereby increasing the SNR. Neither combining, nor attempting the sky subtraction produced desired results and the sample was excluded from further study. By removing these two grisms, the size of the total GH sample remained unchanged and no further attempts were made to try and obtain measurements from those instrumental set-ups.

The line lists were made for the remaining 5 grism set-ups (the complete lists of lines is included in the appendix B) following the procedure as explained for UVES and its summary is presented here.

set-up	# of lines	id line
HRB (HR7A)	37	H β
HR (HR10)	36	Fe I
HR (HR13)	31	Fe I
HR (HR14A)	25	Ca I
HR (HR15)	19	Fe I

Table 3.6: Summary of the GIRAFFE high resolution line list.

Medium Resolution As seen on the right plot of the figure 2-7, candidate HB and RC stars are also present in this sample even if they represent only a small fraction with respect to the RGB, they are crucial in building a homogeneous radial

[18] For GH spectra the resolution is still sufficiently high that strong lines are not blended so there was no need to degrade the sky spectrum used for identifying lines for UVES spectra

velocity measurement of the Sculptor dSph. As discussed in §2.2.3, the blue HB stars show Paschen lines in the region of the CaT lines. The atmospheric conditions of the red HB stars are such that they start showing the Paschen series but the CaT lines still dominate the region of the LR08 grism, as can be seen on the figure 3-4. On the figure the location of the two CaT lines 849.8nm and 854.2nm are marked by a red dashed line. A spectrum of RGB star is present on the top panel, followed by a red clump star spectrum and finally one belonging to an RHB star. From the figure, it is evident that the intensity of the CaT lines is decreasing when moving from RGB to RHB star and that Paschen lines are not yet present in the spectra of RHB stars in my sample. Thus the same line list was used for all the spectra taken with this grism.

The line list was compiled by degrading the original synthetic spectrum to the resolution of $R \sim 6000$ in order to exclude blended lines from the line list (the complete list of lines can be found in the appendix B). The identification of the lines proceeded in the same way as for the UVES and GH. In total 19 lines were identified and the middle CaT line, at 8542Å, was used as a reference line.

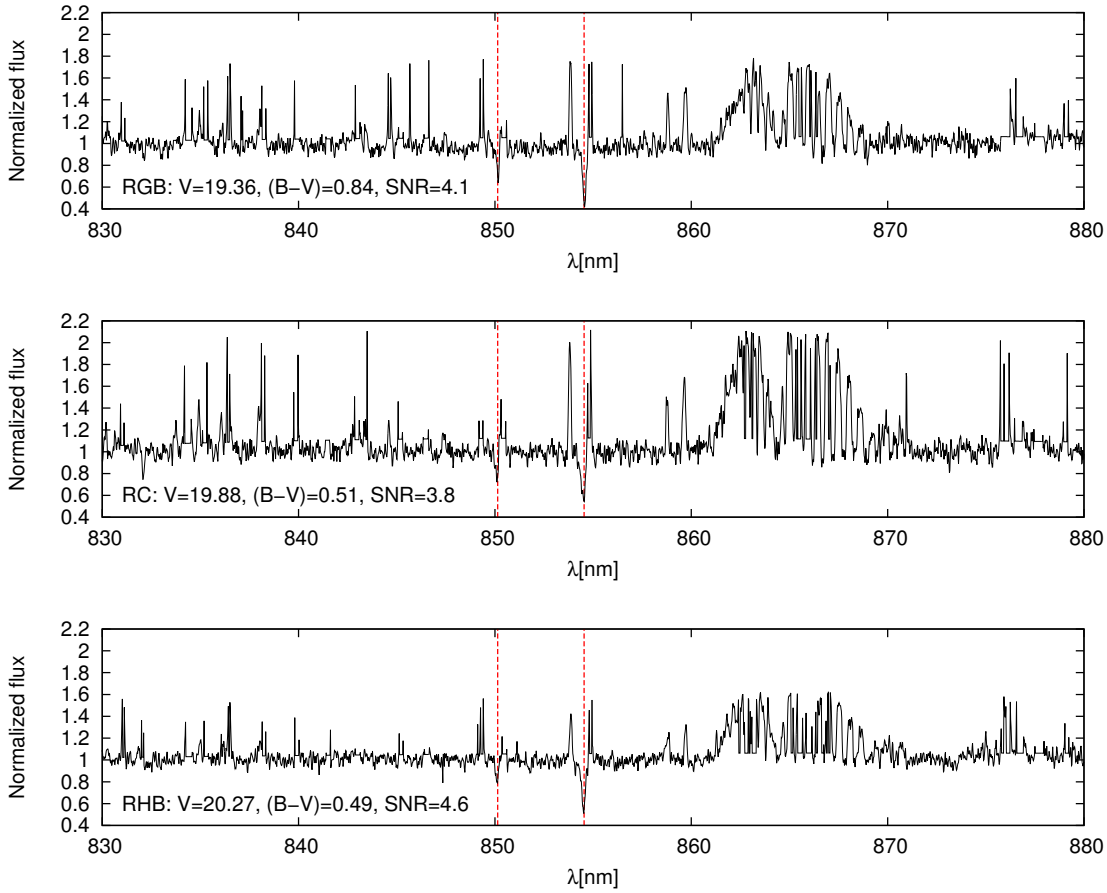

Figure 3-4: Three examples of GIRAFFE low resolution spectra for all the stellar tracers: RGB, RC and RHB that are present in my sample. Red vertical lines indicate the position of the CaT lines shifted for the radial velocity of each spectrum. Due to the low SNR of these spectra and the presence of strong molecular band in the region around ($\lambda\lambda 860 - 870nm$) the third CaT line, $\lambda_{atmos.} = 866.2nm$, is not visible. The third line is clearly visible in the spectrum with higher SNR on the figure 3-3.

Chapter 4

Radial Velocity Measurements and Analysis

In this chapter, I will present the program for radial velocity measurements - *ROSSA*. Their precision will be discussed as well as the accuracy with respect to the higher resolution measurements. Comparison with the literature is presented in the following chapter.

The Program for Radial Velocity Measurements The program with which I measured the radial velocities was written by Michele Fabrizio in *IDL* [8]. As input, it requires the normalized spectrum in ascii format, spectral resolution, wavelength of the reference line and a list of lines to identify in the spectrum.

First, the program fixes the zero point of the velocity scale at the rest wavelength of the specified reference line, converts the wavelength into radial velocity scale and displays the spectrum smoothed[1] in a region of $\pm 500 km/s$ from the reference line within a prompt window. The user is then requested to set the initial guess on the position of the reference line. This value is then used to iteratively fit a Gaussian line profile in order to determine its center μ_λ and to compute the initial guess on the

[1]Spectra are only smoothed at this initial step. This makes it easier to identify the correct line in the prompt window.

radial velocity of the star:

$$rv = c \cdot \frac{\mu_\lambda - \lambda_{atmos}}{\lambda_{atmos}} \tag{4.1}$$

here c stands for the speed of light in vacuum and λ_{atmos} wavelength of the corresponding line in the atmosphere[2]. The Doppler shift is then applied in order to bring the spectrum to a "rest frame". The program proceeds with the Gaussian profile fitting to the lines from the line list.

There are several criteria that candidate lines have to meet in order to reduce the possibility that random noise is identified as an absorption line.

- The radial velocity computed from the line: $rv < c/R$
- The depth of the line must exceed the average level of the noise in the vicinity of the line: $depth > 5 \cdot \langle NOISE \rangle$
- The width of the fitted profile must not be too large ($< 5 \cdot FWHM$) or too narrow ($> FWHM/5$)[3]

If all the criteria are met, then the resulting radial velocity from a given line is saved in order to compute the arithmetic mean, median and biweight mean[4], with the corresponding errors, for each spectrum. Due to its robustness of the location estimator, I used the biweight values of the global radial velocity in further analysis. Hereafter, when the term *individual measurement* is used, it refers to the *radial velocity* of the entire spectrum, not to an individual line.

Initially, I used the task *fxcor* in *IRAF* but internal comparison between the measurements for the same star using different GH grisms revealed a systematic error of radial velocity as a function of the stellar line-of-sight velocity and resolution. After a series of tests, with a synthetic spectrum, it became clear that the trend was always present. Even though the resulting error was smaller than the step size of the spectrum (presented in table 2.3), it was systematic and thus we opted for the use

[2] The spectra I used come from ground based observatories and as the light enters the atmosphere of the Earth its wavelength becomes slightly modified. This occurs due to the different refractive index of vacuum and air.

[3] FWHM here corresponds to the full width at half maximum of the reference line.

[4] The biweight location estimator is a robust indicator, insensitive to outliers both for Gaussian and non-Gaussian distributions[23].

of the IDL program described above. The benefit of which is that, compared with *fxcor* where the reference - synthetic spectrum is rigidly shifted, the radial velocity is instead determined from individual lines. Any error is therefore expected to be symmetrically scattered around the true radial velocity, which was not the case in the *fxcor* method. For further discussion on the measurements with the *IRAF* program, I refer the reader to the appendix A.

The precision of the program was investigated by using a template spectrum in the wavelength region $\lambda\lambda 610 - 640nm$ and applying Doppler shift in steps of $10km/s$ using the *dopcor*[5] task in *IRAF*. The radial velocity was then measured using a line list for the GIRAFFE HR/HR15 set-up[6]. The difference between the measured velocity and the applied shift shows no trend and the average deviation: $\langle v_{shifted\ spectrum} - v_{shift} \rangle = -0.003km/s$ is smaller than the average dispersion of measurements $\sigma = 0.2km/s$.

4.1 UVES\ECHELLE

4.1.1 Acquiring Measurements

The normalized UVES spectra in ascii format were sorted by their wavelength range in accordance to the table 3.2. The spectra taken with the CD#4B(OG590) configuration belong only to one star and are strongly dominated by telluric lines and errors in pipeline reduction procedure. For the (A) part of these spectra (check §3.1.1), 12 lines were identified with the help of the template spectrum and for the (B) part no lines were easily identifiable as they are buried in noise. Therefore, the error of the radial velocity measurements from these spectra would be greater than that coming from the other grisms. Spectra of RGB stars, aside from the prominent CaT lines which coincides with the CCDs gap as mentioned in §3.1.1, show only weak metallic

[5] Documentation available on `http://stsdas.stsci.edu/cgi-bin/gethelp.cgi?dopcor`

[6] It was using this wavelength region that the systematic shift became apparent when I investigated the difference of radial velocity measurements for the same star but different grism, from the *fxcor* task. The robustness of the *ROSSA* program using a real spectrum is presented in appendix A in comparison with *fxcor* measurements.

lines in this wavelength range. Moreover, these spectra belong to only one star, which was also observed with other grism. On these bases the CD#4B(OG590) spectra were excluded from radial velocity measurements.

For the rest of the 3 grisms (171 spectra for 13 objects) I used the lists of lines (presented in appendix B) and the values for the resolution from the table 2.1 in order to run the *ROSSA* program. On average, there are 40 lines to identify in each grism. The average number of lines identified by the program was 21. This reduced the error presented in the table 2.3 by a factor of $\sim \frac{1}{\sqrt{21}}$, meaning $2.5(1.7)km/s \rightarrow 0.6(0.4)km/s$. This is also the order of the error found for each grism and is presented in table 4.1.

The program could not identify any lines in 4 spectra and for 7 spectra only 1 or 2 lines were identified. Lastly, the heliocentric velocity was added to the measured velocities before combining the measurements.

4.1.2 The Precision of the Measurements

The median velocity (MED[7]) was computed for each star from all the measurements and the dispersion ($\sigma_{current}$) of the grism from all the measurements in set grism. The radial velocity measurements deviating more than $3\sigma_{current}$ from the median were removed and the values for the median and the dispersion were recomputed to perform another 3σ clipping. The program I wrote in *python* iteratively repeats the clipping until there are no more outliers. Starting with 160 individual measurements 9 were removed by the clipping procedure.

Based on the difference of each measurement with respect to the median, the standard deviation was computed and associated to each instrumental set-up, which is presented in the table 4.1 together with the number of measurements and stars for each grism.

The precision of UVES measurements is presented on the 4 panels (**A**-**D**) on the figure 4-1. The residuals are within $2km/s$ of the median value and there are no trends in the measurements as a function of velocity, magnitude, SNR or number

[7]Median was used as location estimator as it is less sensitive to outliers than the normal mean.

set-up	# ind. meas.	# stars	$\sigma[km/s]$
CD#2(HER_5)	41	7	0.89
CD#3 (SHP700)	102*	12	0.68
CD#4B (BK7_5)	8*	1	0.35

Table 4.1: Final number of individual rv measurements and objects for UVES measurements after the 3σ clipping.
(*)The spectra from the (SHP700) and (BK7_5) configurations have double measurements because the spectra were split as discussed in §3.1.1.

of identified lines. Moreover, the residuals are symmetric. Based on the internal validation, the UVES measurements were considered precise. The error of individual measurements was replaced with the σ of the corresponding grism in order to compute radial velocity of each star from the median.

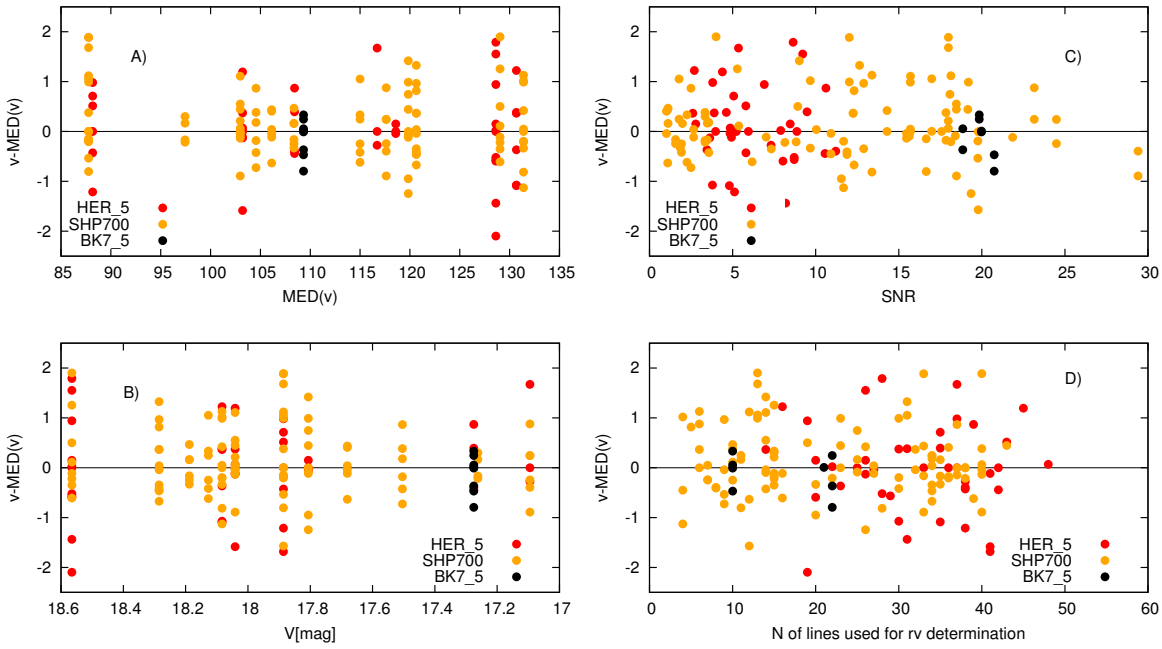

Figure 4-1: Distribution of the residuals of the UVES\ECHELLE measurements as a function of **A)**- median velocity of each star, **B)**- apparent magnitude, **C)**- SNR and **D)**- number of lines used to measure radial velocity, after 3σ clipping to remove the 9 outliers. Measurements from each grism are highlighted in a separate color.

Since the distribution is symmetric, the use of weighted mean of the biweight radial velocities as location estimator, with the dispersion of the grism taken as weight, is justified. The weighted standard deviation was adopted as the error of the combined

radial velocity for each star. This is a standard way of combing measurements with Gaussian errors and different levels of precision. It was later used also for GIRAFFE high and low resolution.

UVES measurements were later used to evaluate the accuracy of lower resolution measurements. Comparison with the literature values of the complete dataset is presented in the next chapter.

4.2 GIRAFFE\High Resolution

The spectra taken in the HR2 and HR22 filter of GIRAFFE high resolution set-up were removed from the sample prior to the measurements, as already mentioned in §3.3.3. For the remaining 5 instrumental set-ups, there were no problems.

4.2.1 Acquiring Measurements

Measurements were conducted in the same way as for the UVES spectra. Out of initial 2029 spectra, 1810 had the respective reference line identified. Out of those, 43 spectra had no other line, from the line lists presented in appendix B, identified. This resulted in the radial velocity measurements for 1767 spectra with, on average, 12 lines identified per spectrum. This meant that the initial estimation of error was reduced $3.2(2.3)km/s \rightarrow 0.9(0.6)km/s$. Similar values were later also found for the σ of individual grism presented in table 4.2.

4.2.2 Analysing the Precision and Accuracy

With acquired measurements I adopted a similar approach as for the UVES spectra to compute the median velocity of each star and the dispersion of each grism. The values were improved through a standard 3σ clipping procedure, which was terminated when all the outliers were eliminated. From the 1767 measurements, 192 or $\sim 10\%$ of them were removed. The remaining measurements had higher average number of identified lines (1.5 lines more) and higher $\langle SNR \rangle$. As seen in the table 4.2, removing the

outliers improved my measurements by as much as 30%.

On average, only 22% of lines from the line list were identified for the HR7A grism, which explains why these measurements are the least precise. For the remaining 4 grisms, the average percentage of identified lines ranged between 50% and 40%, which is also reflected in the precision of the measurements.

In total, from the initial 3925 spectra for 145 stars in 7 grisms I could use only 5 grisms and 1575 spectra to measure radial velocities of 132 stars. Even though less than half of the spectra were of sufficiently good quality to perform the radial velocity measurements (using my reduction process), the final number of measured stars was not significantly affected.

grating	before 3σ clip.		after 3σ clip.	
	# spectra per obj.	σ	# spectra per obj.	σ
HR7A	3.4	1.10	3.4	0.76
HR10	2	0.43	1.9	0.39
HR13	2.9	0.47	2.7	0.29
HR14A	5.5	0.54	4.9	0.52
HR15	2.9	0.59	1.9	0.52

Table 4.2: Dispersion of measurements with respect to the median of individual grism before and after the sigma clipping.

As can be seen from the table 4.2, measurements from the grism HR13 have the smallest dispersion and almost 3 spectra for each star. Therefore, they were taken to be the most precise. Additionally, the percentage of overlapping stars with respect to the other grisms is more than 80%, as can be seen in the table 4.3. Hence, the median velocity from this grism was considered to be the most accurate and was used as a bench mark to examine the accuracy of the other grisms and compensate for any potential systematic offset from the true radial velocity of the stars.

The median and the standard deviation of the difference were computed and only one grism showed an offset larger than its dispersion. The mean difference between the individual HR7A measurements and the median value coming from HR13 was $0.88 km/s$, with $\sigma_{HR7} = 0.76 km/s$. Thus, all the individual measurements using the spectra in the HR7A grism were shifted for the difference. After the applied

grism	# stars	# stars in common with HR13	$\langle \Delta rv \rangle$ $[km/s]$	σ_{grism} $[km/s]$
HR7A*	105	85	0.04	0.76
HR10	110	107	-0.16	0.39
HR13	110			0.29
HR14A	106	105	0.12	0.52
HR15	95	95	0.04	0.52

Table 4.3: Number of stars with measurements in corresponding grisms and the number of overlapping stars with the reference grism. The fourth column shows the average difference between individual measurement and median from the reference grism after the shift applied to HR7A velocities ($\Delta rv = rv_{grism} - MED(rv_{HR13})$). The last column includes the dispersion of the grism measurements.

correction, the median radial velocity of the individual stars was recomputed. The results are presented in table 4.3.

Before investigating the accuracy using the HR13 grism, I made sure that after removing the outliers the distribution of residuals shows no peculiar trend with velocity, magnitude, SNR or number of identified lines. After excluding such peculiarities, I evaluated the accuracy as described above and re-examined the precision. The 4 panels on the figure 4-2 clearly show that the residuals (here the reference value is the median radial velocity from all the grisms and not from HR13) are symmetrically distributed around 0. Since we have a factor of 10 larger sample than for UVES, the bell shape dependence of the residuals on the SNR and number of lines is apparent on the panels **C)** and **D)**. Namely, as the signal to noise of a spectrum increases, the number of identified lines increases, hence the precision. Similarly, it is expected that as the magnitude increases (we are considering fainter stars) the residuals will be more scattered, since the SNR of fainter objects are typically lower. However, the stars in the GH sample have relatively narrow range in magnitude (ΔV=2.5mag compared with GL ΔV=4mag) and the distribution on the panel **B)** only slightly shows the expected trend.

After removing the outliers and correcting the HR7A measurements, I combined all the GH measurements in order to associate one radial velocity to each star. I used the weighted mean to combine the individual measurements (the weight was the error of the biweight mean) in each grism. Assigning the dispersion of the grism as the

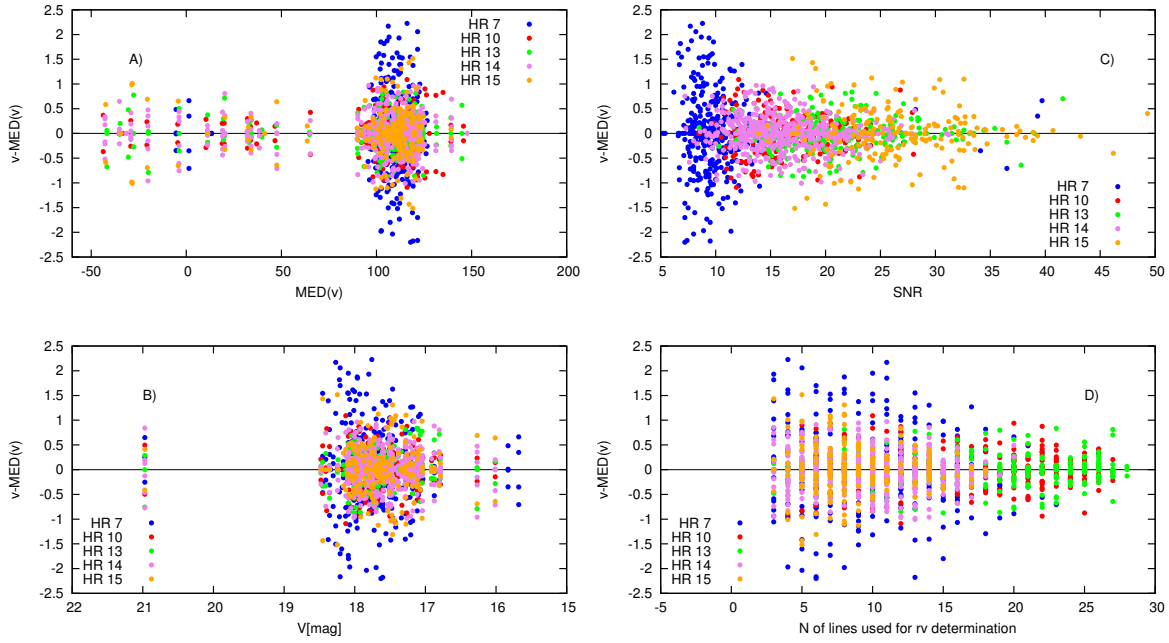

Figure 4-2: Distribution of the residuals of the high resolution GIRAFFE measurements as a function of **A)**-median velocity of each star, **B)**-apparent magnitude, **C)**- SNR and **D)**-number of lines used to measure radial velocity, after 3σ clipping to remove the 9 outliers. Measurements from every grism are highlighted in a separate color.

error of the weighted mean, I combined the measurements from all the grisms in one line of sight velocity and computed its weighted standard deviation.

Lastly, I compared the 5 stars with UVES and GH measurements. Two stars, TScl609 and TScl298, showed unexpectedly large difference $\mid \Delta rv \mid > 3km/s$. Spectra with such a high resolution are not expected to show such a discrepancy. After eliminating the possibility that this error originated in the reduction procedure or radial velocity measurements, I investigated the time variation of the radial velocity measurements. Multi epoch measurements allowed such investigation, which is discussed in greater detail in section §4.4.1. For the remaining 3 stars, the mean difference was $\langle \Delta rv \rangle = -0.03km/s$, for practical purposes negligible.

4.3 GIRAFFE\Medium Resolution

During the final preparation of these spectra, described in §3.3.1, spurious spectra (69) were removed from further analysis. Such spectra showed discontinuities and missing sections, mainly in the region of the CaT. Thus, they were considered unusable, whereas no attempt was made to remove very noisy spectra with low SNR. The unusable, noisy spectra are automatically excluded when performing the radial velocity measurements if the reference line cannot be identified. This approach was adopted in order to maximize the number of objects with radial velocity measurements and is supported by an absence of trend between the precision of the measurements, number of identified lines (presented in appendix B) and SNR from high resolution spectra.

4.3.1 Acquiring Measurements

Compared with UVES and high resolution GIRAFFE spectra, which have more than 10 spectra per object in different wavelength ranges, low resolution GIRAFFE have, on average, only 2 spectra per object covering a relatively narrow wavelength range around the CaT. Together with lower resolution, this results in lower accuracy of measurements using these spectra. In order to test whether sufficient lines from the line list can be identified in the spectra and that the measurements are comparable with already obtained radial velocities, a random sample of 800 spectra was selected and examined.

The initial test revealed no trends in accuracy with apparent magnitude, signal to noise ratio, number of lines identified or radial velocity. The difference between the velocities, obtained from high and low resolution spectra, does show an increasing spread with lower SNR and decreasing number of individual lines used to compute a global radial velocity of the spectra. However, there is no systematic trend. With this important issue investigated, I continued to measure the line of sight velocities for the rest of the GIRAFFE medium resolution spectra.

The program displayed 3191/1380 smoothed spectra/stars, however, the reference line was identified only for 1854/1001. The 379 stars for which the radial velocity

could not be measured are mainly located on the outskirts of the galaxy, but the spatial extend of my sample was not affected by the absence of these stars.

The excluded spectra were additionally inspected but no or little absorption lines were visible. After determining that, even meticulous sky correction could not improve the spectra and any further attempt was disregarded.

Out of the 1854 spectra, 1174 belong to 321 objects and the rest of the stars -680 have only one individual radial velocity, computed from, on average, 5.4 individual lines. It is important to stress again that even though there is only one spectrum, there are several lines that can be identified and the program computes the radial velocity from those individual lines and combines them in a biweight average. Therefore, the number of radial velocity measurement per object are, on average, more than 5, which increases the credibility of the final line of sight velocity.

4.3.2 Analysing the Precision and Accuracy

The stars with more than one spectrum were used to investigate the precision of the whole sample. First a median and standard deviation were computed. Only the values $|MED - rv| < 1.5\sigma$ from the median were used to recompute the median. This 1.5σ constrain was adopted because a few stars had one radial velocity that greatly deviated from the rest, causing a large dispersion and it rendered the usually adopted 3σ criterion useless.

Roughly 10% of the sample (86 spectra /38 objects) showed dispersion larger than $20km/s$. These 38 objects mostly had only 2 spectra and the measurements from the two deviated by more than $20km/s$ from each other. Studies of the presence of binaries are estimating the percentage of them to be 46% [12] but only 6 of the 38 stars had spectra taken more than one hour apart, the others were taken in short succession. Therefore, the orbital motion is probably not the cause of this discrepancy. Moreover, there appeared to be no trend with SNR or number of lines by which I could extend the criteria for spurious measurements to the whole set of measurements. Stars that show this discrepancy were also found across the whole body of the galaxy and evenly spaced along the red giant branch. With no trend identified, such as possible variable

or binary star, this effect is considered a systematic error. With these measurements removed, I continued the iterative processes of sigma clipping until the values for the median converged.

The dispersion of radial velocities converged after 4 runs of the 1.5σ clipping program written in *python* and 963 candidate Sculptor and field stars remained. Out of those, 216 stars had radial velocity measurements only from the reference line. The error associated to those measurements was the maximal error for the GL spectra - $6.86km/s$. For those that have multiple spectra, the error was the dispersion of radial velocities around the mean. The average error for all is $\sim 4.5km/s$. The average error is smaller than the nominal error of the spectra.

In order to asses the accuracy, the median radial velocities were compared with those coming from GIRAFFE high resolution. The samples have very high degree of overlap. Out of 132 stars in high resolution sample, 103 are also present in the medium resolution. For all the stars the median difference is $MED(rv_{LR08} - rv_{GH}) = 0.21km/s$ and $\sigma(rv_{LR08} - rv_{GH}) = 23.2km/s$. The high dispersion of the measurements is caused by 5 outliers which have radial velocities $< 70km/s$, which indicates that they are candidate field stars. After excluding these outliers the resulting median difference $MED(rv_{LR08} - rv_{GH}) = 0.07km/s$ and its dispersion $\sigma(rv_{LR08} - rv_{GH}) = 3.9km/s$ decreased. The distribution, as a function of radial velocity and apparent magnitude, is presented on the figure 4-3. No significant difference is found between the measurements from low and high resolution GIRAFFE spectra.

Thus, I conclude that the radial velocity measurements for the *candidate* Sculptor stars are both precise and accurate within the error of the low resolution spectra.

4.4 Combining the Samples

All the measurements were compiled and ordered by resolution for each star. From the whole sample, 110 stars had more than one radial velocity measurement. For those the highest resolution value was adopted. This resulted in 993 radial velocity measurements from UVES, GIRAFFE high and medium resolution. The final spatial

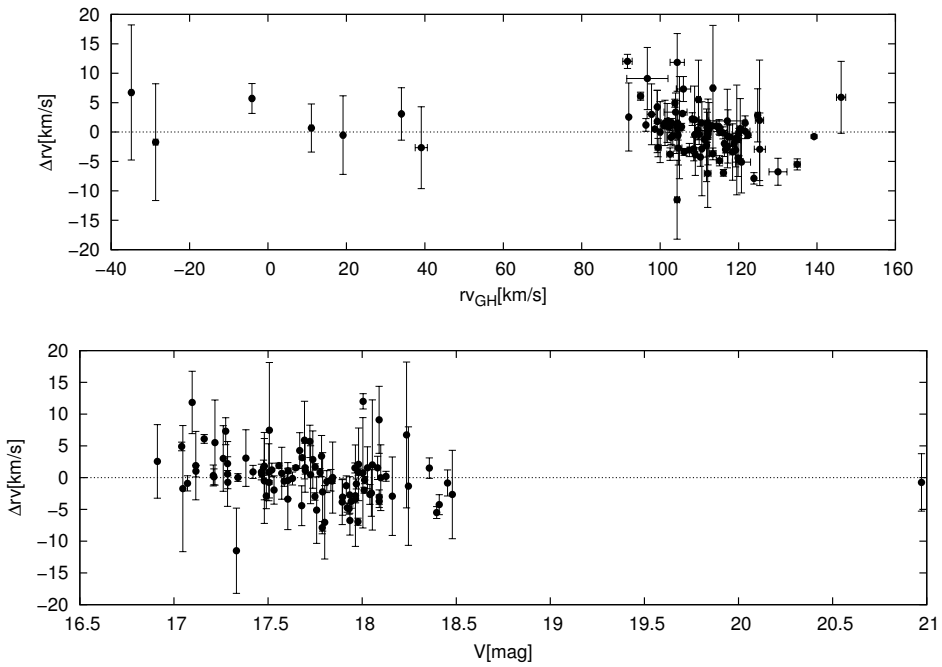

Figure 4-3: Comparison between GH and GL measurements for the $|\Delta rv| < 3\sigma$. On both plots the difference between the combined values from $rv_{GL} - rv_{GH}$ is presented together with their error bars. On the top panel the difference as a function of the radial velocity (as measured from the high resolution spectra) and on the bottom panel as a function of apparent magnitude.

distribution and coverage of the CMD of overlapping stars did not differ greatly from one presented in the figure 2-8. The measurements for candidate Sculptor stars are presented together with literature values in the next chapter. The distribution of the stars with radial velocity measurements is presented on the figure 4-6. The panel **A)** shows the spatial distribution of all measurements and the red points highlight 3σ members of Sculptor. On the panel **B)** 3σ members are depicted in red along the CMD, overlying the photometric catalogue, and CC on the panel **C)**. The final **D)** panel shows the symmetry of the radial velocity peak of Sculptor.

4.4.1 Possible Variability of TScl298 and TScl609

When comparing UVES and GIRAFFE low and high resolution measurements, two objects showed a difference larger than the dispersion of the measurements. These two stars had repeated measurements taken with the UVES spectrograph and such a difference was not present in the other 10 stars that overlap with the GL measurements. The variability index[8] indicated that these stars may be variable and the radial velocity was investigated as a function of the observing time.

The plot on the figure 4-4 shows the individual radial velocity measurements with errors as a function of time. Every star is depicted with its own color. UVES and both GIRAFFE measurements are combined in this sample. The star that does not show this discrepancy - TScl516 is shown with blue dots, whereas the candidate variables are presented in red and orange. The error presented on the plot is the error of the individual measurement and not the dispersion associated to the individual grism. In order to make the plot more transparent, all the measurements for a given star are presented with the same color.

The reference star was observed at seven different times and the variation around the average is $< 2km/s$, the error of the high resolution sample. The candidate variables TScl298 and TScl609 vary more than $2km/s$ between consecutive observations.

[8] The photometric catalogue, used to match the magnitudes with the radial velocity measurements, also includes a variability index for individual photometric band, for which the magnitudes were observed. The index indicates a probability of a star being a variable. The higher the index the higher is the probability of that star being a variable.

The points with the error bars greater than $5km/s$ are GL radial velocities and are presented in order to emphasize the variations.

star	V[mag]	B[mag]	var_V	var_B	var_I	var_R	var_U
TScl298	17.275	18.621	0.858	0.374	0.402	70.5	1.4528
TScl609	18.041	19.006	0.996	0.305	0.380	139.5	1.7247

Table 4.4: The variability index of the two stars that show unexpectedly large discrepancy between UVES - GIRAFFE.

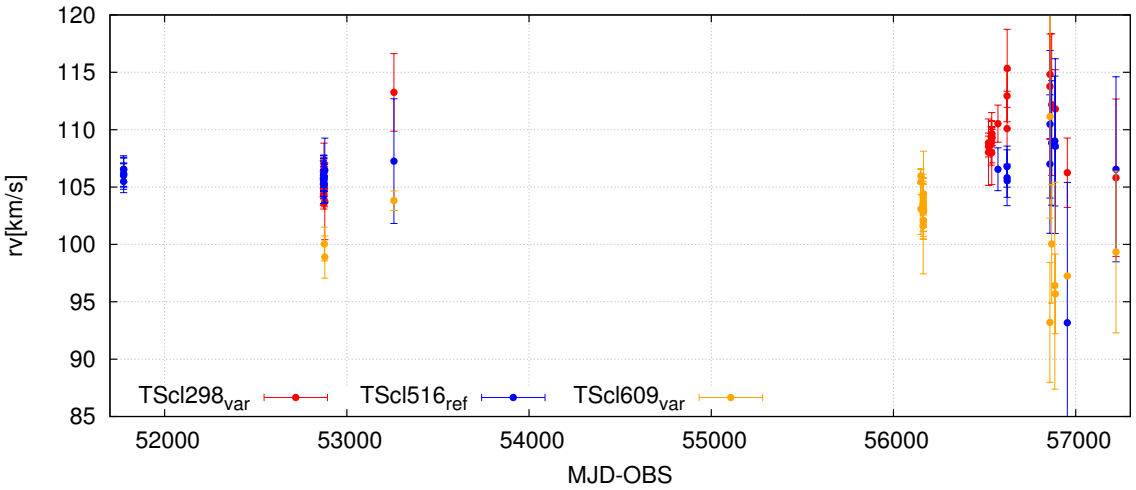

Figure 4-4: Possible variability of TScl298 and TScl609. These two stars have spectra taken with all the spectrographs. The star TScl516 is given as an example of a star that is not candidate variable star but it has similar number of measurements.

We consider these stars good candidates for variables. Other variables may also be present in the data set presented in this thesis, however, only the ones presented in this section had measurements in all the three grisms and showed clear evidence of variation.

4.4.2 Establishing Galaxy Membership

Initial investigation in the global radial velocity distribution showed a separation of the candidate field and candidate Sculptor stars. The field stars have typically different kinematics and metallicity than Sculptor stars. The dominant stellar spectral types that are the main contaminants in the photometric catalogue presented are F

and G type dwarfs, which can be clearly identified on the CMD as two plums of constant color but different apparent magnitude. This trend is vanishing on the left panel of figure 2-1 because of my truncation of the photometric catalogue. In the presence of weak extinction, color is insensitive to the distance and on the right panel of the figure the sequences belonging to thick and thin disk are easily identifiable.

Even with 3-dimensional position of the stars known, it is in general not possible to discriminate between field stars and stars belonging to a group. Stars belonging to a group or galaxy, typically, all have similar kinematics and metallicity. By investigating the number of stars, as a function of radial velocity, we can associate plausible membership to a group of stars (that either still are or have been at some point gravitationally bound). For the 993 stars, for which I have measured radial velocities, I computed the location of the peak of the radial velocity distribution that belongs to Sculptor and its dispersion. The purpose of this investigations was to confirm that kinematically selected members also correspond to tighter distribution of the stars on the CMD and CC[9] plots, while preserving the spatial distribution.

In order to find the location of the peak, I made an initial guess on the systemic $v_{l.o.s.}$ of Sculptor and its dispersion σ based on the literature values presented in the table 1.2. Then, I iteratively removed measurements 3σ from the peak and used median to obtain the systemic velocity and recomputed dispersion at each step. The process converged after 4 iterations and the results are presented in the figures 4-5 and 4-6.

Compared with the initial distribution, the 3σ members are more tightly constrained along the RGB branch on the CMD. On the CC plot, almost no stars are found on the locus of points typically populated by thick and thin disk Milky Way stars as well as halo stars. The residual points that are scattered across the plots on the **B)** and **C)** panels of the figure 4-6 are partially due to the photometric errors. On the figure 4-5 it is evident that the extended low velocity peak, populated by field

[9]Star belonging to a coeval stellar population with the same metallicity populate a narrow region on the (V-I) (B-V) color plane. This condition is not strictly speaking met for the Sculptor stars however, the difference in the metallicity of the field and Sculptor stars is sufficient to quantitatively comment on the distribution.

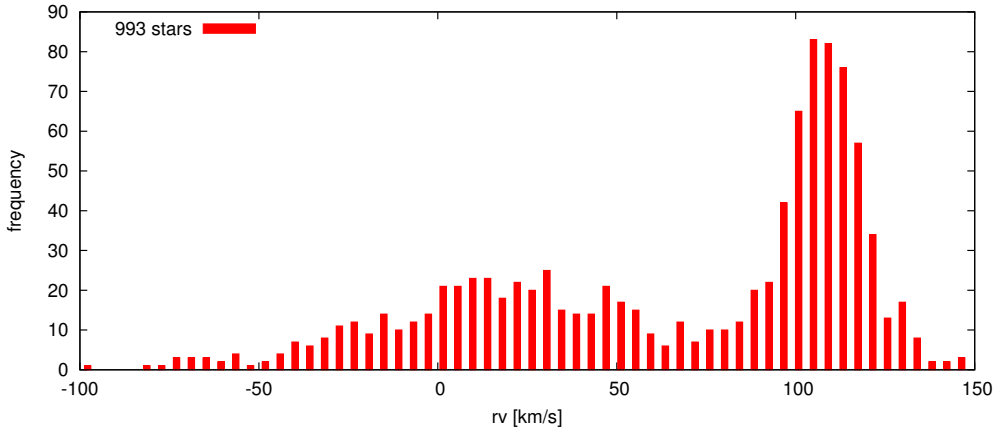

Figure 4-5: Radial velocity distribution of the whole set of measurements - candidate field stars and candidate Sculptor stars.

stars, has high velocity tail that extends in the Sculptor peak. The discussion on the number of the contaminant stars is presented in the following chapter. It is also important to note that the 3σ members of Sculptor extend beyond the nominal tidal radius. Therefore, the kinematics of the least bound stars can be investigated.

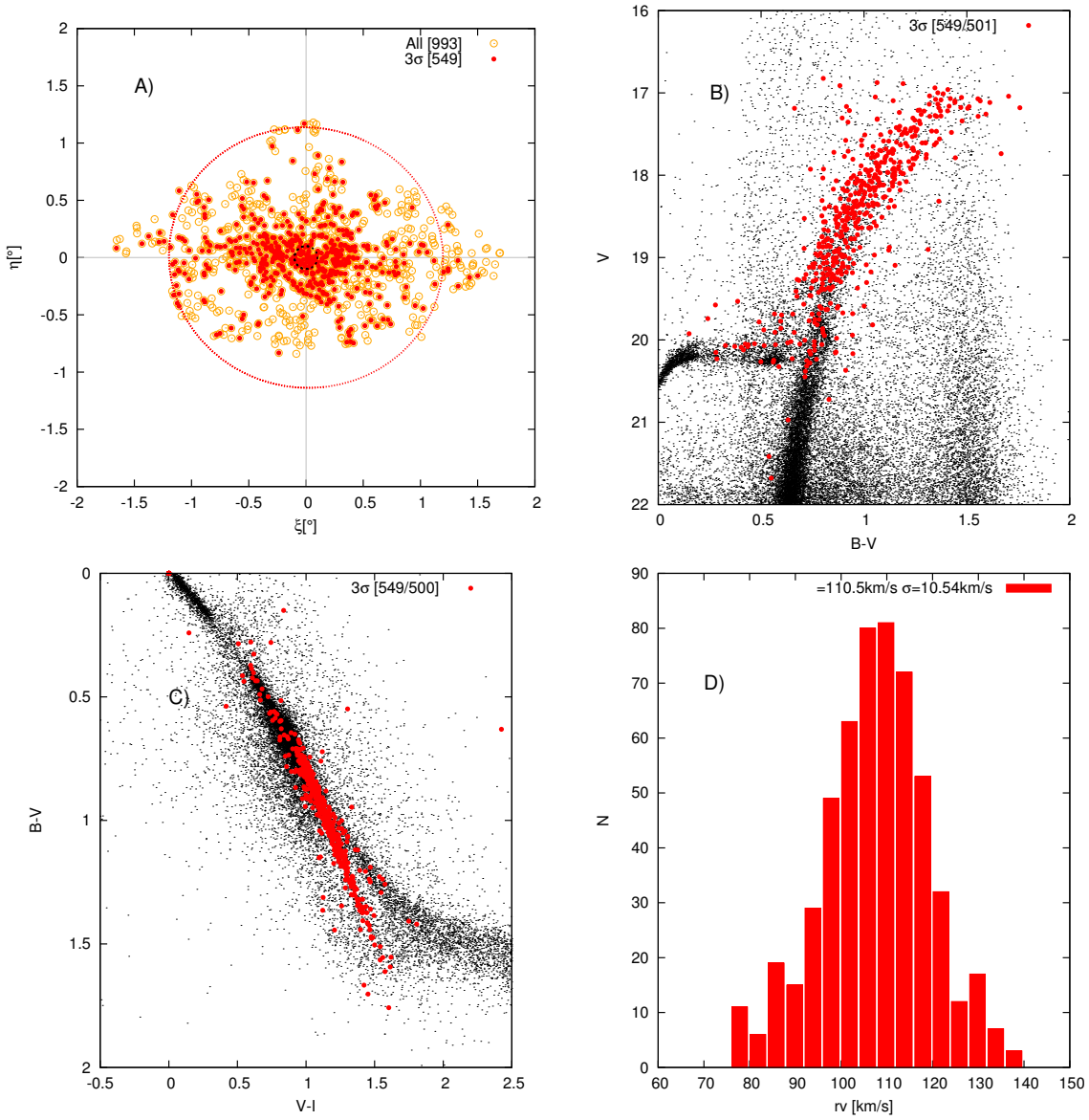

Figure 4-6: Distribution of candidate Sculptor stars after 3σ clipping. The plot **A)** shows the distribution of all stars with radial velocity measurements with orange circles and the stars after the 3σ clipping with red dots. The key contains the number of points depicted. The red ellipse represents the tidal radius of the galaxy and the black circle the core radius of Sculptor. The plot **B)** shows the CMD after the clipping and the key contains [# stars/# displayed stars]. Similar is the structure of the key on the plot **C)** where the distribution of candidate Sculptor stars is presented on the color-color plot overlying the photometric catalogue. The plot **D)** depicts the distribution of probable kinematic members of the Sculptor dSph after removing the candidate field stars.

Chapter 5

Results

In order to present the largest and most homogeneous sample of radial velocities for the Sculptor dSph, I combined my data-set with publicly available literature samples. The largest such a sample, published in 2009 ([26], henceforth identified as W09), is briefly presented in this chapter, with the emphasis on the overlap with my sample and the analysis of the 270 stars that were present in both data set.

With samples combined, the kinematic membership is evaluated in section §5.2 and the number of contaminant stars examined using the **Model of stellar population synthesis of the Galaxy - Besançon**[1]. The effect of kinematic selection on the distribution of the stars across the galaxy, the CMD as well as CC plane, are presented in the succeeding section.

Finally, the systemic velocity and the velocity dispersion are presented in the last section, together with the radial and angular variation of both quantities. These results are afterwards compared with the literature.

5.1 Literature Data - Individual Measurements

Here only the literature data with radial velocities of individual stars will be presented, as opposed to the papers, presenting only the Sculptor systemic velocity and the velocity dispersion. In the series of papers by Walker et al. 2007-2009 ([25], [26], [27])

[1] `http://model.obs-besancon.fr`

the acquisition of spectra, data reduction and the largest sample of individual radial velocities, for the stars in the direction of the Sculptor dSph, have been presented.

As a part of the survey, 4 local group dwarf spheroidal galaxies were observed: Carina, Fornax, Sextant and Sculptor. Using a photometric catalogue, they selected candidate RGB stars of the aforementioned dwarfs in the magnitude range $17 \leq V \leq 20.5$, which is similar to the sample I compiled. The resolution of the spectrograph is $R \sim 22000$ and the median error they reached was $\pm 2.1 km/s$. The spectra include a prominent MgT, from which they also derived metallicity indicator. In order to measure radial velocity, they combined $\sim$ 500 spectra of bright late-type stars, 1/3 were standard radial velocity stars with known velocity and the rest were taken from Milky Way globular clusters. To obtain radial velocity they used the *fxcor* task in *IRAF*, where the combined spectrum was taken as a template. The measurements included radial velocities for 1533 Sculptor candidates with estimated 990 kinematic members.

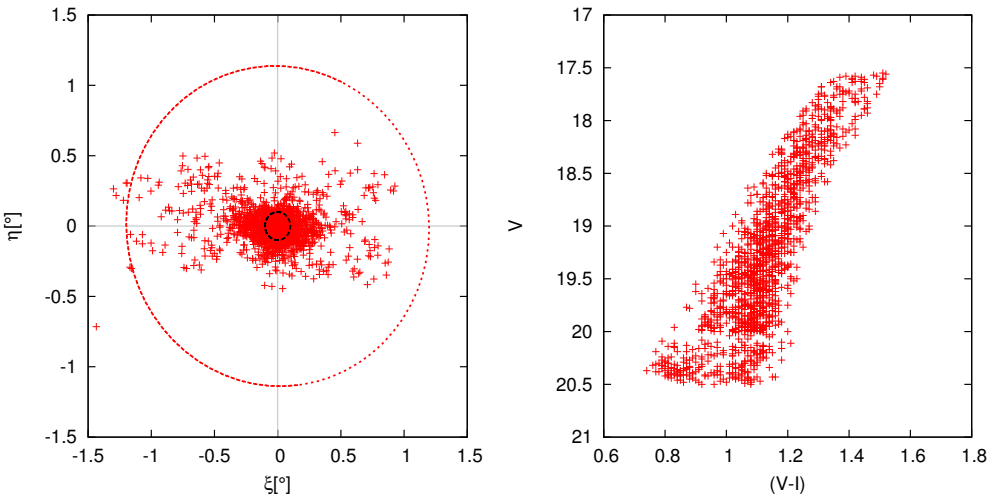

Figure 5-1: The spatial distribution and CMD of the targets in literature sample. The measurements are concentrated along the semi-major axis of the galaxy, several measurements are also found beyond the tidal radius. Along the color magnitude diagram, the stars in the W09 sample span similar magnitude and color ranges as the sample of my measurements seen, depicted with orange circles, on the A) panel of the figure 4-6. The red ellipse on the left plot corresponds to the tidal radius and the black circle to the core radius of the Sculptor dSph.

The color magnitude diagram for stars presented in W09 was plotted using the

photometric magnitudes from the catalogue presented in §2.1.

5.1.1 Overlap Between Spectroscopic Targets and Literature Sample

The combined sample of 996 stars with radial velocity measurements from UVES, GIRAFFE high and low resolution were compared with 1533 stars in the W09 catalogue. The plots on the figure 5-2 depict the overall sample in grey and the position of the overlapping stars (stars with both measurements) with orange, black and red points. In total, 270 stars are in common (7 from UVES, 59 from GH and 204 from GL subsample). They cover the whole galaxy and the entire length of the red giant branch down to the horizontal branch, which is close to the selection criteria of the MMFS survey, at $V \sim 20.2$.

Investigating the difference between my measurements and W09 values 30 stars showed peculiar trend with $\Delta rv > 40 km/s$. According to W09 values, they were all radial velocity members, whereas my measurements placed them among the field stars. These stars were, on average, fainter ($\langle V \rangle = 19.05$) than the total sample of overlapping stars ($\langle V \rangle = 18.34$) and mainly located near the galactic tidal radius. Most of them (24) had only one spectrum taken with GIRAFFE low resolution spectrograph, which were re-examined to investigate the source of this discrepancy.

The radial velocity was measured again using *ROSSA* program and also for the three CaT lines using *splot* task in *IRAF*. Both additional measurements agreed with the original values within the error. The difference of more than $40 km/s$ can not be explained by orbital motion, in case of binaries, or intrinsic variability and, as such, I removed the stars from further analysis. Since based on my measurements, these stars belong to the field stars and thus, the final number of candidate Sculptor stars was not affected by removing the questionable stars.

The spread of Δrv is not symmetric, as can be seen on plot 5-3, therefore, median and scaled median standard deviation (MADN[2]) were used to investigate possible

[2]Scaled median standard deviation. The selection on the scaling constant is such that in the case of symmetric distribution the MADN equals the standard deviation.

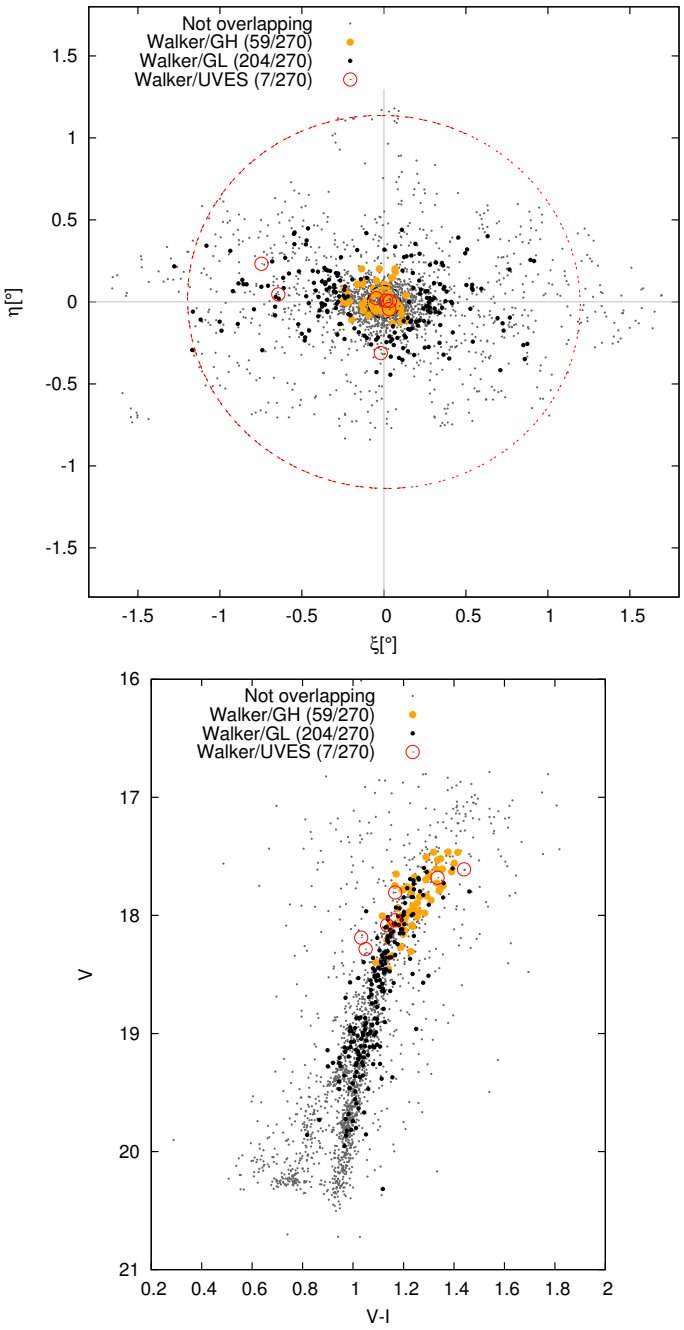

Figure 5-2: Spatial distribution of literature data and spectroscopic targets (the combined sample as discussed in §4.4) as well as CMD position of the complete data-set highlighting the overlapping stars. On both plots grey dots represent combined sample of literature and the sample presented in this thesis that have only one of the two radial velocity measurements. The orange points show position of the stars that have both literature and GIRAFFE high resolution measurements, black dots correspond to stars with literature and GL radial velocities and open red circles indicate the position of the stars with both literature and UVES measurements. The red ellipse on the upper plot corresponds to the tidal radius and black circle to the core radius of the Sculptor dSph.

systematics between the two datasets. In order to remove the outliers, I used median clipping, which is more robust than the 3σ clipping when the distribution is not symmetric.

	#	$\langle V \rangle$	MED$(\Delta rv)[km/s]$	MADN$[km/s]$	$\langle \Delta rv \rangle\,[km/s]$	$\sigma\,[km/s]$
initial	270	18.52	-2.76	6.47	-9.03	46.63
final	201	18.40	-2.06	3.83	-2.60	5.21

Table 5.1: The table presents the initial statistical values of the 270 overlapping stars and 201 stars after removing the outliers.

After 4 iterations, the values for the scaled median standard deviation converged and the statistic of the overlapping stars before and after the clipping is presented in the table 5.1. The standard deviation decreases by a factor of 9 and mean by a factor of 3, while MADN only by a factor of 2 and MED only changes by $0.70km/s$. This relatively small increase demonstrates the robustness of the median clipping as the location estimator in such non symmetric distribution. From the table, it is also evident that just the faint targets are removed by the clipping. The spectra from fainter stars, typically, have lower SNR, hence larger errors and this decrease in the average magnitude was expected.

In order to accurately determine the shift in radial velocity, I also considered the errors of the individual measurements and used the weighted mean. This location estimator takes into account the precision of individual measurements, so it is a better choice compared with MED or average, where all the measurements are equally weighted[3]. To every $\Delta rv = rv_{This\ work} - rv_{W09}$ the error of $\sigma = \sqrt{\sigma^2_{This\ work} + \sigma^2_{W09}}$ was associated and for the 201 remaining stars the weighted mean difference between the two samples was: $\Delta = -2.51 \pm 0.12km/s$.

A systematic shift between W09 and measurements using ESO spectra was also presented in the paper by Amorisco and Evans in 2012 [1], where the shift was estimated to be $-1km/s$. This shift was estimated between the radial velocity distribution as a function of position for the $\sim$ 600 stars measured by Battaglia et al.

[3]Several tests were conducted to verify that median clipping does not affect the resulting weighted mean. By using the weighted mean and standard deviation as criteria for clipping, the final result was the same but took by a factor of 3 more steps to converge.

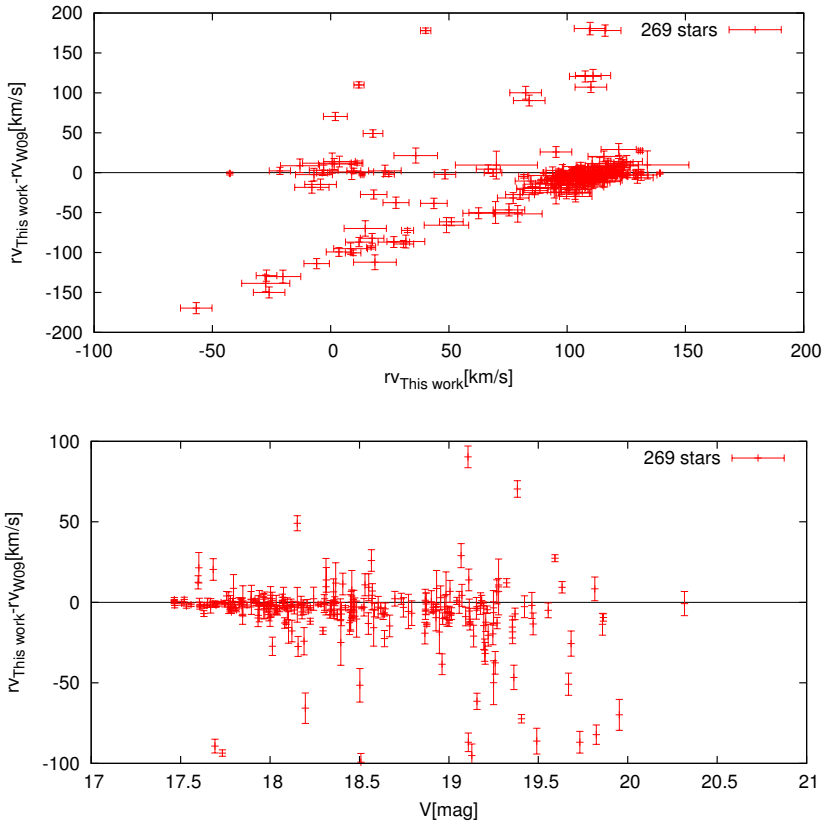

Figure 5-3: The plots show the difference in measured radial velocity between the literature sample and the one presented in this work with the corresponding errors. Top panel shows the difference as a function of radial velocity and bottom panel the difference as a function of visual magnitude. On this panel the increase in the accuracy as we are moving towards the brighter magnitude is evident. Brighter stars with typically higher SNR have smaller errors (since more spectral lines are identified and used for the measurements), compared with fainter objects. The stars fainter than ~ 18.5 magnitude show significant increases in the dispersion compared to the brighter objects, with approximately the same number of stars, fainter stars have $\sim 50\%$ greater dispersion than the brighter objects.

in 2008 [3] and distribution from the W09 measurements. The shift was, therefore, not estimated by comparing stars that have both measurements but by comparing distributions. Even if their value does not exactly agree with my analysis, it does show the same systematic trend of overestimated velocities in the sample of W09, compared with ESO spectra derived values. From experiences with the *fxcor* task in appendix A and the clear trend in radial velocities that it produces, the cause of this systematic shift probably lies in the method used to obtain W09 measurements, but a more detailed analysis is needed. Several tests with artificially shifted stellar and synthetic spectra revealed that the *ROSSA* program introduces no systematic shift with radial velocities that is present in the measurements using the *fxcor* task. These were solid reasons why the shift was to be applied to W09 measurements and not to the measurements presented in this work.

5.1.2 Merging the Datasets

The systematic shift of $\Delta = -2.51 \pm 0.12 km/s$ was applied to the 1262 W09 measurements, not overlapping with my sample, and merged with 924 radial velocities presented in this work (13 UVES, 127 GH and 784 GL measurements). The merged dataset includes 2188 stars with radial velocities determined, on average, better than $3.7 km/s$. Their distribution is presented in the bottom figure 5-4.

From the figure 5-4, the increase in the spatial extent of the stars with radial velocity measurements is evident. While the literature sample is mainly concentrated in a region along the semi-major axis (left plot on the figure 5-1), the combined sample extends towards the ellipse marking the tidal radius, almost at every azimuthal angle. This increase in the coverage allows for complete analysis of the behaviour of radial velocity across the galaxy and not only in a preferred direction.

From the CMD on the panel **B)** of the figure 5-4, it is clear that the stars in the combined data-set densely populate the RGB of Sculptor with minor fraction of RC and RHB stars present at fainter magnitudes ($V > 19.5$) and bluer colors ((V-I)$<$0.8).

The bottom panel **C)** of the radial velocity distribution shows two peaks. An extended distribution centred around $20 km/s$, belonging to field stars. A stronger

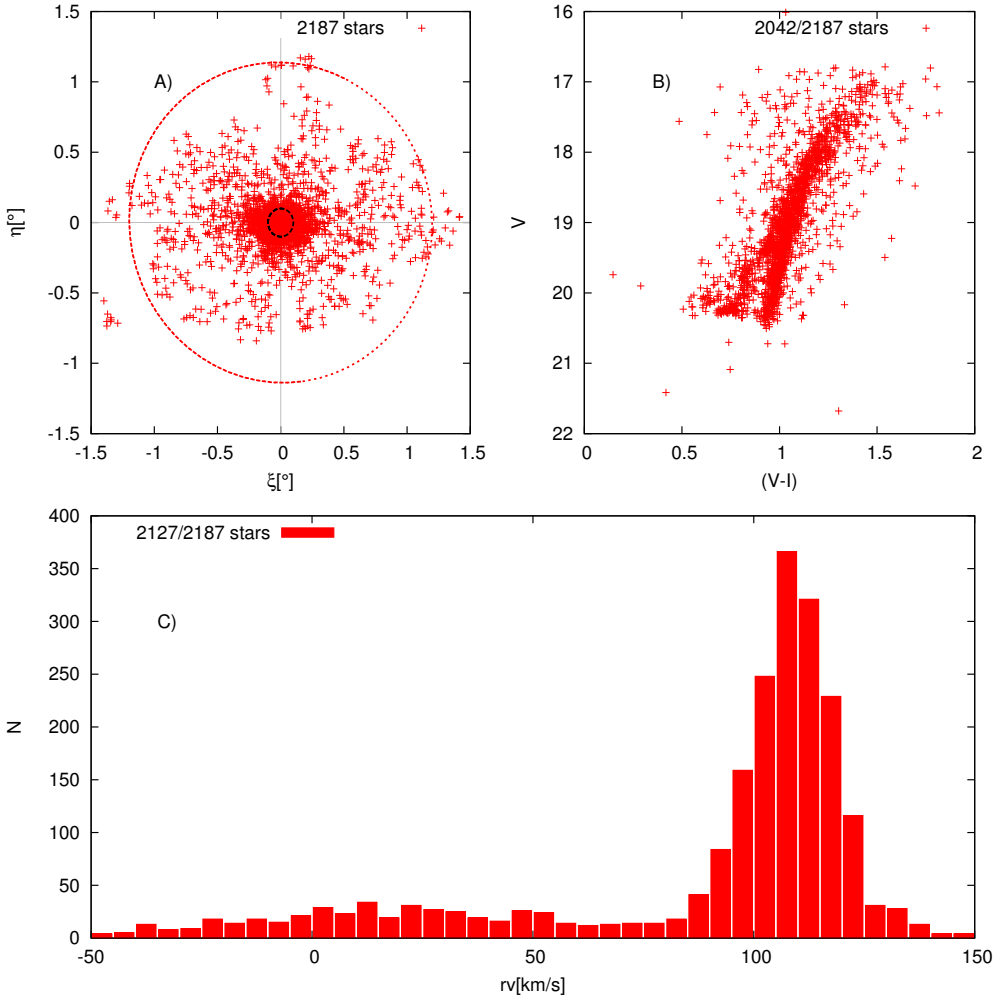

Figure 5-4: The three panels on this figure show the distribution of the combined sample across the body of the galaxy in the panel **A)** (the black circle represents the core size and red ellipse the tidal radius), the color magnitude diagram on the panel **B)** and the histogram of radial velocities on the panel **C)**. Not all the stars in the combined sample have photometric magnitudes and the radial velocity distribution was truncated to remove the high velocity outliers thereby making the plot more transparent. The key in the panels **B)** and **C)** shows the number of stars presented on the plot compared to the total number in the sample.

and narrower peak, centred around $110km/s$, is populated mainly by Sculptor stars. The peak of Sculptor stars appears symmetric around the mean. It is evident that the distribution of field stars extends also in the radial velocity peak of the Sculptor dSph. When the kinematics are used to assign galactic membership for the stars in similar distribution, it is important to estimate the number of field stars with similar velocities as those belonging to the galaxy. The number of contaminant stars is discussed in §5.2.1.

ID	$\alpha(J2000)$	$\delta(J2000)$	V	B	I	rv
	deg	deg	mag	mag	mag	km/s
TScl105[a]	14.395	-33.6629	18.08	19.01	16.95	131.13 ± 0.89
TScl281[b]	14.7858	-33.7082	18.01	18.96	16.89	91.67 ± 0.24
TScl186[c]	14.6239	-33.6393	19.01	19.94	17.93	103.93 ± 3.65
TScl2912[d]	15.0325	-33.7293	19.14	19.91	18.15	91.5 ± 7.7

Table 5.2: Section of the table of radial velocity measurements with the position of the star and photometric magnitude. Complete table is available in the electronic form.
[a] - measurements from UVES spectra
[b] - measurements from GIRAFFE high resolution spectra
[c] - measurements from GIRAFFE low resolution spectra
[d] - W09 measurements

5.2 Galaxy Membership

The procedure to find the systemic velocity and the dispersion velocity was the same as described in 4.4.2. By using the values from the table 1.2 as initial guess on the parameters, I performed 5,4,3 and 2.5σ clipping. The weighted mean systemic velocity increases with the decreasing order of the clipping and converges at the 3σ threshold. The resulting systemic velocity is $rv_{systemic} = 110.14 \pm 0.02km/s$ and the velocity dispersion is $\sigma = 9.86 \pm 0.06km/s$ with 1652 kinematic members. Section of the table with the final results is presented in the table 5.2.

The systemic velocity and the velocity dispersion agree within the errors with the two most recent investigations (Battaglia et al. 2007 and Walker et al. 2009) on the samples of comparable sizes, as is seen in the table 5.3. The values are larger

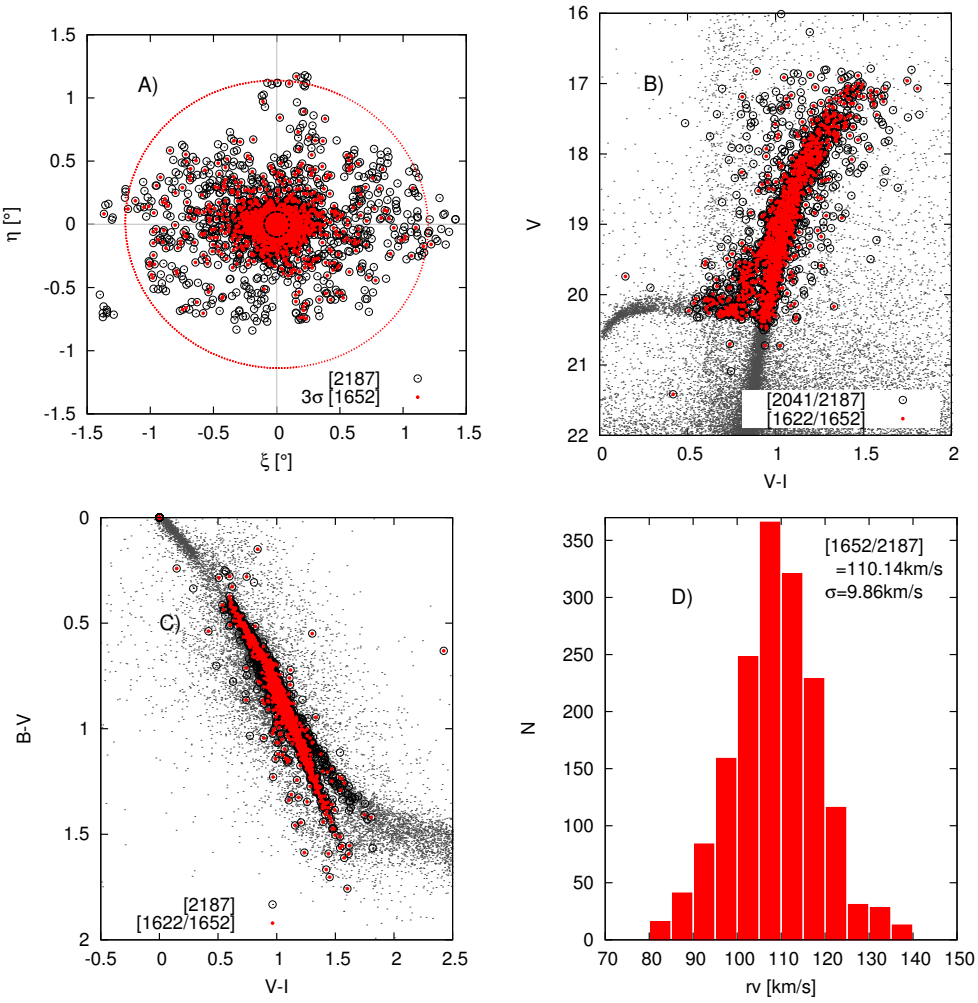

Figure 5-5: The four panels on the figure show the distribution of the complete data set I compiled, presented with black circles on the panels **A)-C)**, and the distribution of the targets after 3σ clipping around the radial velocity peak of Sculptor, shown with red dots. The histogram shows the distribution of the 3σ members together with the first moment and square root of the second moment of the distribution.

source	# stars	$v_{l.o.s.}^{Scl}\,[km/s]$	$\sigma\,[km/s]$
Armandroff & da Costa [2]	16 RGB	107.4 ± 2.0	$6.3^{+1.1}_{-1.3}$
Queloz, Dubath & Pasquini [19]	21 RGB	109.9 ± 1.4	6.2 ± 1.1
Walker et al. [25]	1365 RGB	111.4 ± 0.1	9.2 ± 1.1
Battaglia et al. [3]	470 RGB	110.6 ± 0.5	10.1 ± 0.3
This work	1652 (RGB, RC and RHB)	110.14 ± 0.02	9.86 ± 0.06

Table 5.3: Short comparison of previous measurements and the values obtained in this work.

than the two initial investigations by Armandroff & da Costa 1986 and Queloz et al. 1995 determined. These measurements, however, were based on samples 2 orders of magnitude smaller than the one presented in this work.

As can be seen on the **C)** panel of the figure 5-4, the kinematic selection of the Sculptor members is also seen on the color magnitude digram and in the color-color plane. This trend was expected based on the star formation history of Sculptor and metallicity as discussed in §1.4 and it confirms the validity of kinematic selection.

5.2.1 Contaminant Field Stars

As can be seen from the figure 4-5, the high velocity tail of the disk and halo stars extends into the peak of the Sculptor stars. In order to evaluate the number of contaminant stars, I used the Besançon online stellar population model. After providing the direction in galactic coordinates, distance, magnitude, velocity and spectral type range, the program returns a list of stars, with stellar parameters, distance and radial velocity.

I simulated ~ 4400 stars and since there were ~ 540 field stars in my sample, I randomly extracted 540 stars from the simulated catalogue. After making sure that histogram of radial velocities of the extracted stars approximates the histogram of measured field stars, I computed the number of stars per bin in the radial velocity range populated by Sculptor stars. Based on the simulated stars the total percentage of contaminant stars in the velocity range of Sculptor stars is less the 4%, ~ 60 stars. In the range of 1σ around the peak, the fraction of contaminant stars is less than 0.02. Therefore, the determination of the second moment of the distribution is not significantly affected by possible field stars.

5.3 Radial Velocity and Velocity Dispersion

To further investigate the kinematics of the Sculptor dSph, the behaviour of radial velocity and velocity dispersion was studied as a function of elliptical distance and angle. Even if the number of field stars is negligible, they were considered when computing the distribution of radial velocities and velocity dispersion. Firstly, the simulated field stars were sorted in radial velocity bins with the same step size as Sculptor stars. When both were separated into the same bins, the number of contaminant stars was randomly extracted from corresponding Sculptor radial velocity bin. The remaining Sculptor stars were then used to compute the angular and radial variation of systemic velocity and velocity dispersion. The random extraction was performed 20 times and from the average and the standard deviation of the computed profiles the mean radial and angular distributions were plotted together with the associated errors. The mean distribution runs along the center of the red shaded region on the figures 5-6 and 5-7 while the black lines, that constrain the area, mark the error in each radial bin or angular wedge.

5.3.1 Radial Distribution and Angular Variation

To make the radial plot, the distance to each star from the center of the galaxy was computed, taking into account the photometric ellipticity and position angle of the galaxy, as presented in §1.4. The stars were sorted by their distance and for 100 stars in one bin the procedure, as described in the introduction to the section, was used to build up the radial distribution. We found 100 stars in a bin to be optimal. Using smaller bin sizes resulted in a very noisy distribution. Larger bins, on the other hand, suffered far from the center of the galaxy. There the number of stars decreases exponentially, which strongly affected the number of stars in the bin[4]. The running average replaced 15 stars with equal number of more distant stars

[4]We tried 50 stars in each bin and the general behaviour of the two plots were similar. Larger binning of 150 stars resulted in different behaviour in the outer regions because of the increasingly smaller number of stars in one bin. Namely the last full, 150 stars sized bin, is located at a distance of $r \sim 48'$, meaning that ~ 1450 stars out of ~ 1650 are located within less than a half of the tidal radius at $r_t \sim 76'$.

and average distance was computed at each step together with the weighted mean radial velocity and dispersion. Similar procedure was adopted to make the angular distribution across the galaxy.

Radial variation of the line of sight velocity and velocity dispersion is presented on the figure 5-6. The upper panel of the figure shows how the radial velocity varies as a function of the elliptic radius. The oscillations in the radial velocity, which are visible from the center and up to $r \sim 20'$, are most likely caused by the fact that at every value r different values of the azimuthal angle are considered. This is supported by the upper plot of the figure 5-7, where it is clearly seen that the radial velocity distribution has two minima in the I and IV quadrant, while it is steadily increasing across the II and the III quadrant. This effect is more dominant in the central region and is smoothed out at larger radii. The radial distribution also shows a steady decrease of the line of sight velocity beyond the $r \sim 38'$, which is the opposite of what has been reported in previous studies by Battaglia et al. 2007 [3] and concurs with investigations by Walker et al. 2007 [28]. There is an increase in the radial velocities for $r > 75'$ but it is not clear whether it is real since the number of stars in the radial bin falls below 50 at around $r \sim 60'$.

The velocity dispersion, on the bottom panel of the figure 5-6, steadily increases up to the tidal radius at $r_t \sim 76'$, where it suddenly decreases. Due to the limited number of measurements beyond this distance, it is not possible to contribute the sudden change in the trend to a physical reason but to the incompleteness of the data at larger radii. A sudden dip in the radial distributions appears at $r \sim 38'$. The change in trend follows the maxima of the line of sight velocity distribution at $r \sim 36'$ in the upper panel, thus indicating a correlation between the two quantities. The increasing trend of velocity dispersion with the elliptical radius, up to the truncation radius of the galaxy, has also been reported by previous studies.

Angular variation of the line of sight velocity and velocity dispersion is presented here for the first time, since the kinematic Sculptor members extend to or beyond the tidal radius at almost every azimuthal angle, as seen on the **A)** panel of the figure 5-5. This observation is reinforced by the fraction of Sculptor members in

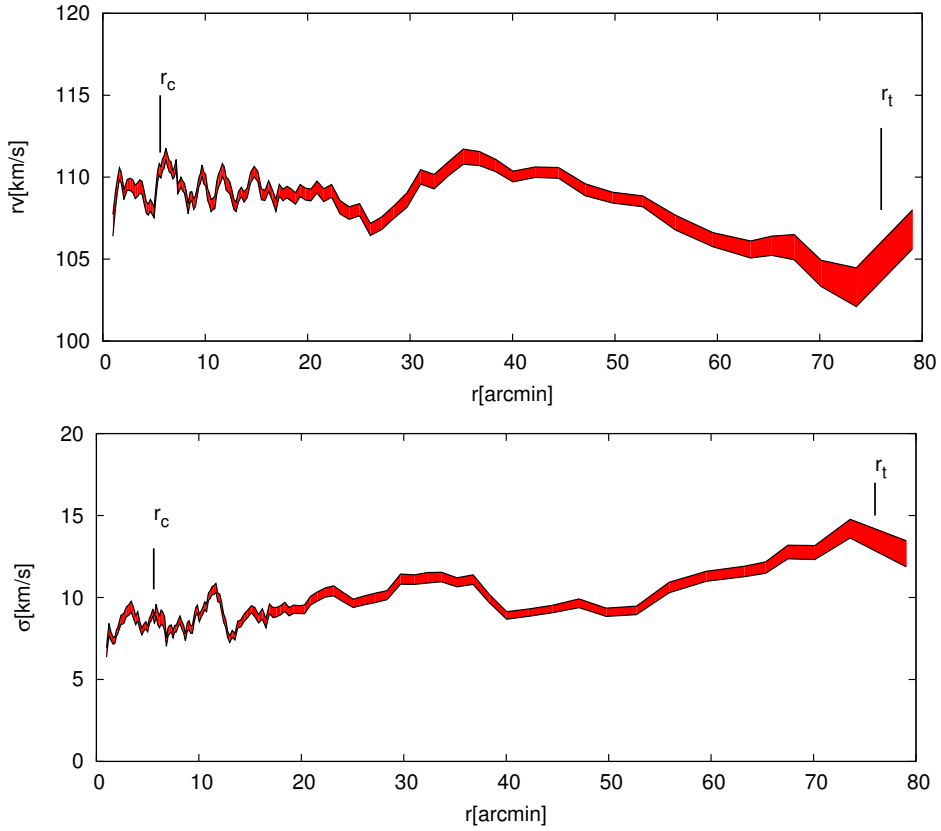

Figure 5-6: The plots depict the variation of the radial velocity and velocity dispersion as a function of elliptic radius. Tidal radius and the core radius are marked on the plot with black arrows.

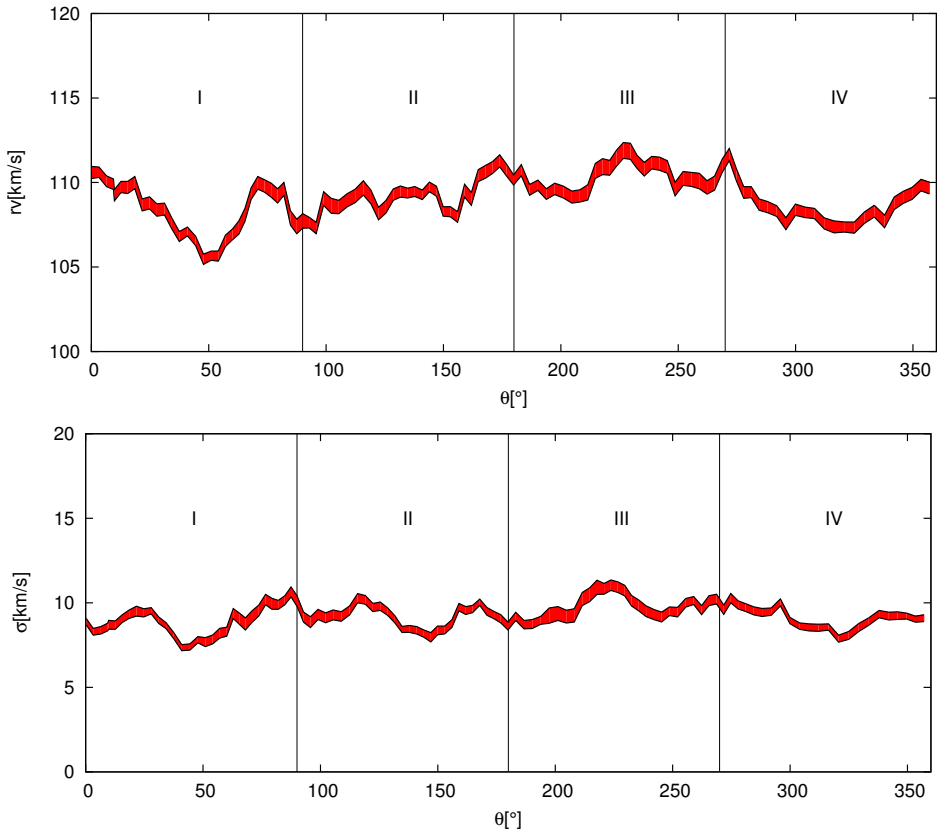

Figure 5-7: The plots depict the variation of the radial velocity and velocity dispersion as a function of the azimuthal angle, where the zero point is taken to be the northern minor axis of the galaxy and the angle increases eastward.

each of the quadrant: **I**:27%, **II**:25%, **III**:27%, **IV**:21%. In almost every quadrant $^1/_4$ of the measurements is present. The figure 5-7 depicts the angular variation of the line of sight velocities and velocity dispersion. The $v_{l.o.s.}$ shows a presence of two minima in the first and last quadrant and a steady increase in between. This hints at a minor rotation, with Ist and IVth quadrant moving towards and the others away the Sun. Based on the aforementioned fraction of stars in each quadrant, this trend cannot be caused by the difference in the number of measurements in each quadrant. The difference between the minimum and the maximum of the angular plot $\Delta = 6.4 \pm 0.4 km/s$ suggests that the rotation is of the order of $\sim 3 km/s$. Slight rotation of $\sim 2 km/s$ was also reported in the literature [3]. The angular variation shows no apparent trend of the dispersion velocity as a function of the azimuthal angle.

Chapter 6

Conclusions

Dwarf galaxies observed in the Local Group are the fossil record of the Galaxy formation process. Due to their high mass to light ratio and proximity, a complete and detailed kinematic study can be conducted in order to trace the underlying dark matter and to investigate the interaction history with the Galaxy. In the course of my thesis, I compiled the largest sample or radial velocity measurements of stars in the direction of the Sculptor dwarf spheroidal galaxy (dSph). In total, I measured radial velocities for 924 stars in the field of the Sculptor dSph from, in total, 7313 repeated spectra with resolution ranging between $R \sim 7000$ and $R \sim 40000$. The pre-reduced spectra I used in this work were taken in the course of more than 13 years with UVES/ECHELLE, GIRAFFE high resolution and low resolution spectrographs, mounted at the VLT. The long temporal baseline provides a unique opportunity to average out possible variations in radial velocity due to intrinsic variability of the star or orbital motion in a binary. The stars for which I measured radial velocity cover the whole body of the galaxy. High resolution GIRAFFE spectra are more centrally concentrated, whereas UVES and GIRAFFE low resolution extend up to the truncation radius. The targets also cover the stellar tracers of the old and the intermediate-age stellar populations: red giant branch (RGB), red horizontal branch (RHB) and red clump (RC) stars.

After the final steps of reduction, I measured radial velocities using the *ROSSA* program, which searches and identifies predetermined set of lines. The radial velocity

of each line is measured and the final result for every spectrum is a biweight mean of all the lines the program identifies. The program was found to be very robust and measurements for the same star in different grisms were found to agree with each other better than $1km/s$. The method of using high resolution measurements in order to constrain the systematics and investigate the accuracy of lower resolution measurements has proven to be very effective. The multi epoch measurements, such as presented here, enable qualitative investigation of the presence of binaries and variable stars, which can inflate the velocity dispersion.

The dataset of 924 stars presented in this work was complemented with Walker et al. 2009 (W09) [26] measurements and the combined set is presented here for the first time. The data sets coming from ESO spectrographs and MIKE spectrograph are compared here for the first time in a systematic way. Systematic shift between the two datasets, based on direct comparison of the 201 overlapping stars, is found to be $\Delta = -2.51 \pm 0.12km/s$. The origin of this offset is probably in the method used to obtain the W09 measurements. Similar behaviour was noticed in the first series of radial velocity measurements using *fxcor* and is discussed in the appendix A. The kinematic membership of the Sculptor dwarf was assigned to 1652 stars, from the total set of 2187 stars, using 3σ clipping around its radial velocity peak. This is 50% more than what has been presented to date with an average error of the entire sample better than $3.8km/s$. The kinematic selection criterion also reduces the scatter on the color magnitude diagram (CMD) and color-color (CC) plane in the direction of Sculptor as seen on the **B)** and **C)** panels on the figure 5-5.

The galactic systemic velocity of $rv_{Systemic} = 110.14 \pm 0.02km/s$ and velocity dispersion $\sigma = 9.86 \pm 0.06km/s$ were found to be in agreement with the literature values, as highlighted in the table 5.3. The precision of the new measurements is one order of magnitude better than what has been presented until now. The increase in precision is mainly a consequence of the 50% increase in the sample of radial velocity measurements. The radial variations of the two values are also in agreement with several previous investigations, with steadily increasing velocity dispersion towards the tidal radius, while the radial velocity starts to decrease at around $1/2r_t$. These

trends are opposite to what Battaglia et al. 2007 [3] found using GIRAFFE low resolution spectra. The discrepancy is most likely caused by the size of the sample of radial velocity measurements, since my sample is more than a factor of 3 larger than in the aforementioned paper.

The radial velocity Sculptor members, in the sample presented here, extend up to or beyond the tidal radius at almost every azimuthal angle. This homogeneous coverage allows, for the first time, the angular behaviour of the radial velocity and velocity dispersion to be examined in a systematic way. Slight presence of rotation is present on the plot of angular variation of radial velocity, which was also reported in the literature and is supported by almost equal percentage of stars in every quadrant. The distribution of radial velocity as a function of the azimuthal angle shows two minima in the I and the IV quadrant and a steady increase from the II to the III quadrant. This indicates a rotation of the order of $3km/s$.

6.1 Future Prospects

Using multi epoch observations reduces the influence of orbital motion in binary star systems or intrinsic variables on the dispersion velocity. This should be investigated in greater detail, since not properly accounting for these effects can inflate the radial velocity dispersion and increase the estimate on the total galactic mass.

Since the Sculptor dSph shows evidence of two stellar populations with different metallicities and ages, fainter horizontal branch stars should be subjected to similar analysis in order to get a more complete picture of the evolution of this and other dwarf galaxies as well as a better understanding of dark matter profiles at these mass ranges. The method of using high resolution measurements to constrain the systematics and investigate the accuracy of low resolution values can be used to expand the sample of measurements to lower resolutions. Thereby, fainter HB stars could be observed without the loss of accuracy.

After the photometric and kinematic studies, it would be greatly beneficial to investigate the metal content of the Sculptor dSph. Such an expanded sample would

enable the investigation of a metallicity gradient in connection with the radial and angular behaviour of radial velocities and velocity dispersion. Such a complete analysis would allow for a better understanding of the formation of this galaxy. The chemical content of the stars can be used as a tracer of intermediate-age and old stellar populations. Stellar populations along the RGB can also be separated using a specific color index $c_{U,B,I}$ as a function of the visual magnitude, similar discrimination of the RGB stars in Carina dSph [7] has already been successfully utilized. In order to create the complete plot using this color index, photometric catalogue of Sculptor stars needs to be completed with the U,B,I magnitudes assigned to each star.

Finally, the rich kinematic information in this sample, coupled with the measurements of the metal content of an equally large sample, should be compared with the chemo-dynamical simulations. The metallicity provides a crucial information in splitting the stars between old (metal poor) and intermediate-age (metal rich) stellar populations. Thus, the interaction history of Sculptor with the Galaxy could be better understood, as well as the dark matter density profile. This analysis would also benefit by increasing the number of radial velocity measurements in the outskirts of the galaxy, by which the behaviour of radial velocity and velocity dispersion could be qualitatively studied.

Appendix A

Measurements Using *fxcor*

Initially, the measurements for the radial velocities were conducted using the *fxcor* task in *IRAF*. Starting with the highest resolution UVES spectra, I used 4 synthetic spectra as templates to measure radial velocities as described in §3.

All the correlation peaks were higher than 0.8 as it is advised in the manual of the task and no peculiar trends were found performing internal validation of the measurements. There was little variation between the measurements using different synthetic spectra.

After measuring the radial velocities for the GIRAFFE high resolution sample and comparing the measurements from different grisms among each other, a trend appeared. Further investigation revealed that the origin of the trend were neither the spectra nor the reduction procedure but the *fxcor* task itself. In order to verify this hypothesis, first the stellar spectra were artificially shifted in radial velocity in steps of $20km/s$ up to $\pm 120km/s$, around the velocity range of the systemic velocity of the Sculptor dSph. Using three GH spectra the measured radial velocity were compared with the applied shift. The comparison clearly showed that the larger the intrinsic radial velocity of the spectrum we are measuring, the lower is the measured velocity compared with the true value. Comparing measurements from three spectra of different SNR, it was clear that the lower the SNR, the steeper is the relation.

The figure below shows this investigation, comparing the measurements from the *fxcor* task depicted with filled boxes and the *ROSSA* program depicted with empty

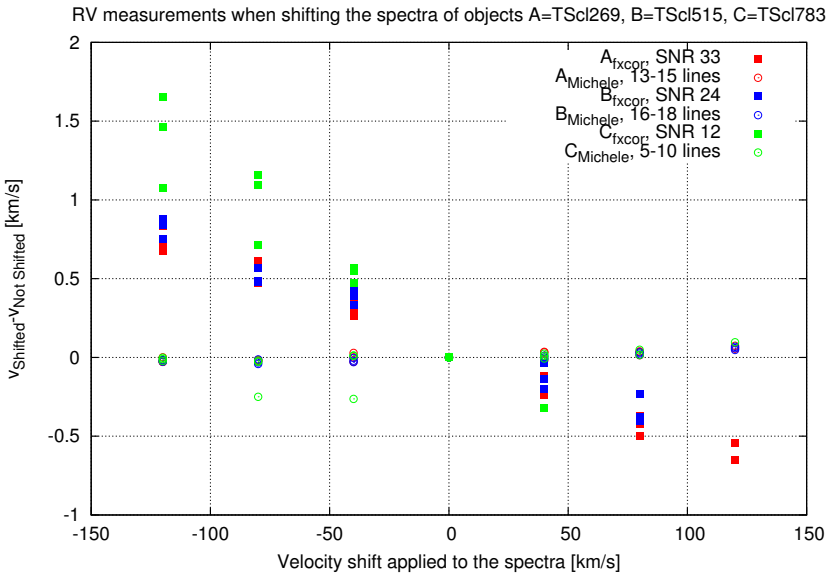

Figure A-1: The plot depicts the difference between the measured radial velocity and applied shift as a function of the shift applied to the spectra. Two methods are compared and each star is presented with the same color and different symbols correspond to each method.

circles. Each color corresponds to measurements of one of the three spectra used to investigate this trend.

To indisputably confirm this trend, I also performed the same test on the template spectrum that has effectively infinite resolution. Even though the difference at a shift of $120km/s$ was only $-0.5km/s$, it was systematically present. With the systematic trend confirmed, the measured radial velocities were discarded. All the spectra were remeasured using the *ROSSA*.

Appendix B

Line Lists

The line lists, which are used in order to obtain radial velocity measurements with the *ROSSA* programme, are presented in this appendix. Tables include the species and the air wavelength of the atomic transition in Ångström. Reference line is marked with an asterisk (*). For each grism the reference line, an example of one strong and one weak line is presented in the figures. These examples serve to demonstrate the the consideration, that were taken into account, when selecting lines for the radial velocity measurements (not blended, strong, not saturated). Spectra, presented here, were all chosen for their high SNR and clear lines. Information on the spectrum and the star are presented in the figures. The bottom axis on the figures displays wavelength (in Ångström for UVES and nm for GIRAFFE spectra) and the top axis displays radial velocity. The velocity axis is computed starting from the grey line marking the air wavelength of the transition labelled on the top of each panel.

The spectra from the UVES spectrograph are not corrected for heliocentric correction. To obtain the $v_{l.o.s.}$ the heliocentric velocity had to be added to the velocity presented in the plots. In the case of GIRRAFE spectra this correction was already considered in the automatic pipeline.

UVES

λ [Å]	species	λ [Å]	species	λ [Å]	species	λ [Å]	species
4861.32743	HI$^{(*)}$	5006.10489	FeI	5183.60179	MgI	5276.00017	FeII
4871.30725	FeI	5007.24487	FeI	5188.70170	TiII	5316.63946	FeII
4878.18713	FeI	5012.08479	FeI	5197.56154	FeII	5328.03926	FeI
4890.74691	FeI	5014.24475	TiI	5204.54142	FeI	5371.49850	FeI
4891.48690	FeI	5018.42468	FeI	5206.02139	CrI	5397.13805	FeI
4918.98642	FeI	5041.74427	FeI	5208.44135	CrI	5405.77790	FeI
4920.50639	FeI	5107.58312	NdII	5227.18102	FeI	5429.71748	FeI
4923.92633	FeII	5110.38307	FeI	5262.18041	TiII	5446.91718	FeI
4934.06615	BaII	5167.38207	FeI	5266.56034	FeI	5455.57703	FeI
4957.30575	FeI	5169.00204	FeII	5269.54028	FeI	5528.39575	MgI
4957.62574	FeI	5171.60200	FeI	5270.32027	FeI	5602.87445	SiI
4991.08516	TiI	5172.68198	MgI	...	...	...	...

Table B.1: List of lines for radial velocity measurements in CD#3 (SHP700) - A. The asterisk (*) marks the reference line used in this grism.

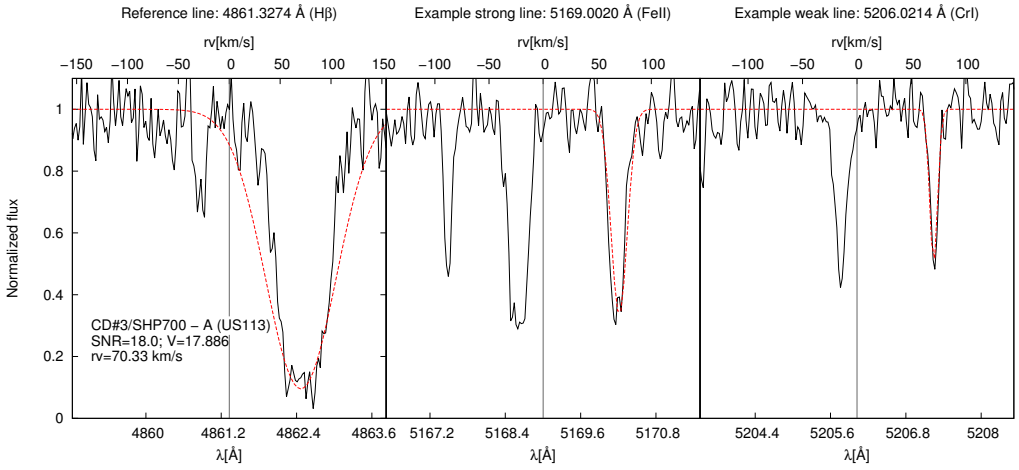

Figure B-1: Example of 3 lines for rv measurements in CD#3/SHP700 - A grism.

λ [Å]	species	λ [Å]	species	λ [Å]	species	λ [Å]	species
3900.52424	FeI	3956.38326	TiI	4083.62104	MnI	4250.79811	FeI
3902.94420	FeI	3961.52317	AlI	4101.74072	HI	4271.75774	FeI
3903.86418	MgI	3963.70314	CrI	4118.80042	CoI	4290.27742	FeI
3905.52415	SiI	3963.94313	NdII	4129.70023	EuII	4294.09735	TiII
3906.46414	FeI	3964.26313	TiI	4132.02019	VI	4307.85711	TiII
3907.06413	EuII	3968.46305	CaII	4143.85998	FeI	4315.01699	FeII
3913.50401	TiII	3976.62291	FeI	4172.65948	FeI	4325.01681	ScII
3914.30400	FeI	3981.74282	FeI	4173.45946	FeII	4325.75680	FeI
3915.96397	ZrII	3989.78268	VII	4177.59939	FeI	4339.43656	CrI
3918.36393	ErII	3997.94254	CoI	4198.27903	FeI	4340.45654	HI
3918.60392	SmII	4005.26241	FeI	4202.03896	FeI	4351.81634	CrI
3920.26390	FeI	4030.78196	MnI	4205.01891	FeI	4383.53579	FeI
3922.90385	FeI	4033.06192	MnI	4215.51873	SrII	4384.75577	VI
3927.92376	FeI	4035.66188	MnI	4225.35856	FeI	4404.75542	FeI
3933.66366	CaII	4041.34178	MnI	4226.71853	CaI	4415.11524	FeI
3938.34358	FeI	4045.78170	FeI$^{(*)}$	4227.37852	FeI	4435.61488	EuII
3944.02348	AlI	4048.74165	MnI	4233.17842	FeII	4459.09447	FeI
3948.74340	FeI	4063.58139	GdII	4239.85830	FeI	4482.21406	FeI
3949.10339	FeI	4071.74124	FeI	4246.81818	ScII	...	...
3952.62333	FeI	4077.70114	SrII	4247.37817	NdII	...	...

Table B.2: List of lines for radial velocity measurements in CD#2 (HER_ 5). The asterisk (*) marks the reference line used in this grism.

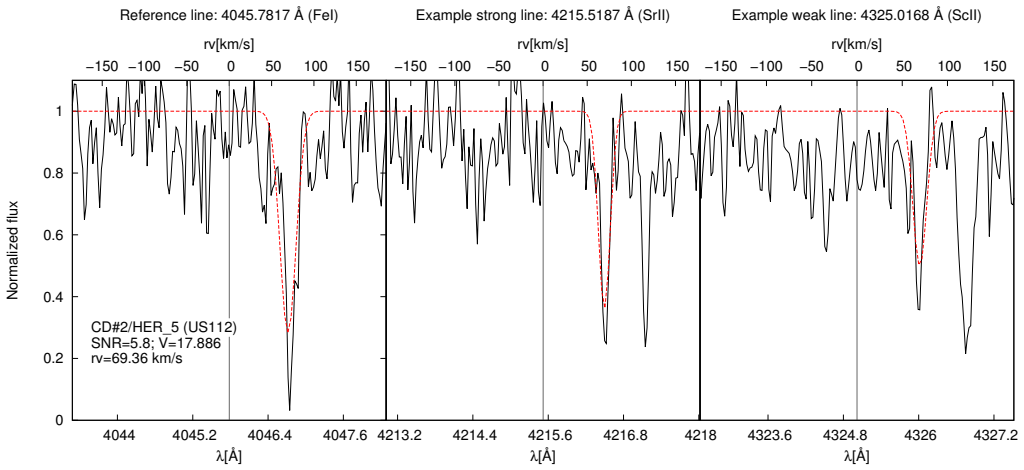

Figure B-2: Example of 3 lines for rv measurements in CD#2/HER_5 grism.

λ [Å]	species	λ [Å]	species	λ [Å]	species	λ [Å]	species
5853.69006	BaII	6162.16466	CaI	6301.50222	FeI	6496.91880	BaII
5889.94943	NaI	6191.56415	FeI	6335.32163	FeI	6516.07847	FeII
6016.64721	MnI	6230.72346	FeI	6400.00050	FeI	6562.79765	HI$^{(*)}$
6065.48635	FeI	6245.64320	ScII	6430.83996	FeI	6643.63624	NiI
6122.22536	CaI	6254.22305	FeI	6439.07982	CaI	6677.97564	FeI
6141.72502	BaII	6279.76260	ScII	6462.59940	CaI	...	...

Table B.3: List of lines for radial velocity measurements in CD#3 (SHP700) - B. The asterisk (*) marks the reference line used in this grism.

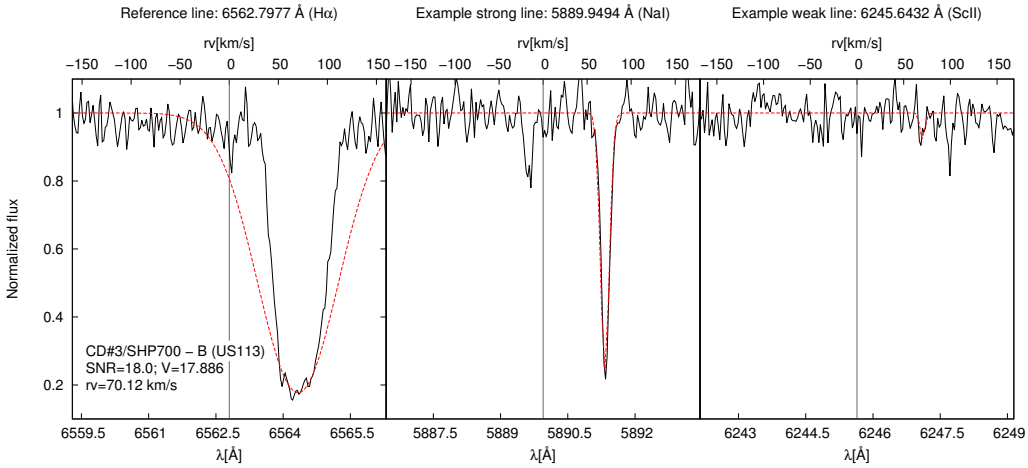

Figure B-3: Example of 3 lines for rv measurements in CD#3/SHP700 - B grism.

λ [Å]	species	λ [Å]	species	λ [Å]	species	λ [Å]	species
5657.89349	ScII	6122.22536	CaI	6301.50222	FeI	6562.79765	HI$^{(*)}$
5658.79347	FeI	6141.72502	BaII	6335.32163	FeI	6643.63624	NiI
5669.03329	ScII	6162.16466	CaI	6400.00050	FeI	6677.97564	FeI
5709.41259	FeI	6191.56415	FeI	6430.83996	FeI	7148.14741	CaI
5853.69006	BaII	6230.72346	FeI	6439.07982	CaI	7187.32672	FeI
5889.94943	NaI	6245.64320	ScII	6462.59940	CaI	7289.16494	SiI
6016.64721	MnI	6254.22305	FeI	6496.91880	BaII	7326.14429	CaI
6065.48635	FeI	6279.76260	ScII	6516.07847	FeII	...	...

Table B.4: List of lines for radial velocity measurements in CD#4B (BK7_5) - A. The asterisk (*) marks the reference line used in this grism.

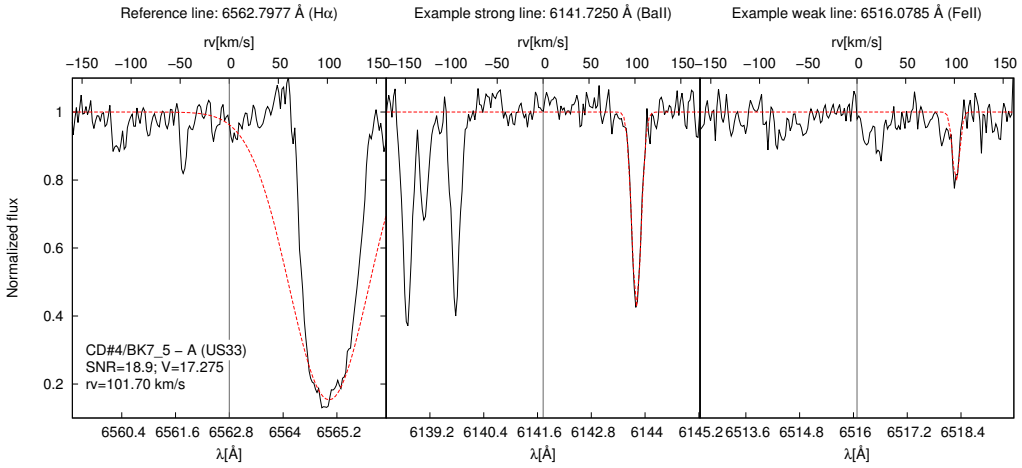

Figure B-4: Example of 3 lines for rv measurements in CD#4/BK7_5 - A grism.

λ [Å]	species	λ [Å]	species	λ [Å]	species	λ [Å]	species
7511.02106	FeI	7937.13360	FeI	8498.02378	CaII	8688.62045	FeI
7664.91836	KI	8194.82909	NaI	8542.08301	CaII$^{(*)}$	8757.17925	FeI
7725.03731	SI	8327.06678	FeI	8662.14091	CaII	...	...
7748.27691	FeI	8387.76571	FeI	...	...	...	...

Table B.5: List of lines for radial velocity measurements in CD#4B (BK7_5) - B. The asterisk (*) marks the reference line used in this grism.

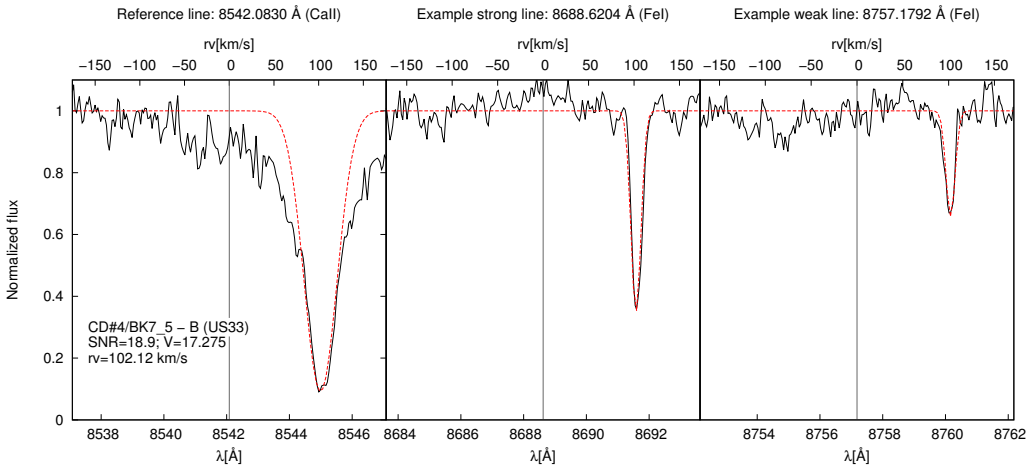

Figure B-5: Example of 3 lines for rv measurements in CD#4/BK7_5 - B grism.

GIRAFFE high resolution

λ [Å]	species	λ [Å]	species	λ [Å]	species	λ [Å]	species	λ [Å]	species
4708.663	TiII	4805.085	TiII	4861.323	HI(*)	4891.495	CrII	4939.687	FeI
4733.591	FeI	4823.489	MnI	4865.61	TiII	4903.31	FeI	4942.496	CrI
4745.8	FeI	4823.502	MnI	4871.318	FeI	4918.994	FeI	4946.388	FeI
4763.883	TiII	4824.131	CrII	4872.138	FeI	4920.502	FeI	4950.106	FeI
4766.408	MnI	4831.176	NiI	4876.397	CrII	4923.922	FeII	4966.089	FeI
4772.832	FeI	4848.25	CrII	4878.126	CaI	4924.77	FeI	...	...
4783.425	MnI	4849.168	TiII	4889.002	FeI	4934.005	FeI	...	...
4798.531	TiII	4859.742	FeI	4890.755	FeI	4938.814	FeI	...	...

Table B.6: List of lines for radial velocity measurements in HRB (HR7A). The asterisk (*) marks the reference line used in this grism.

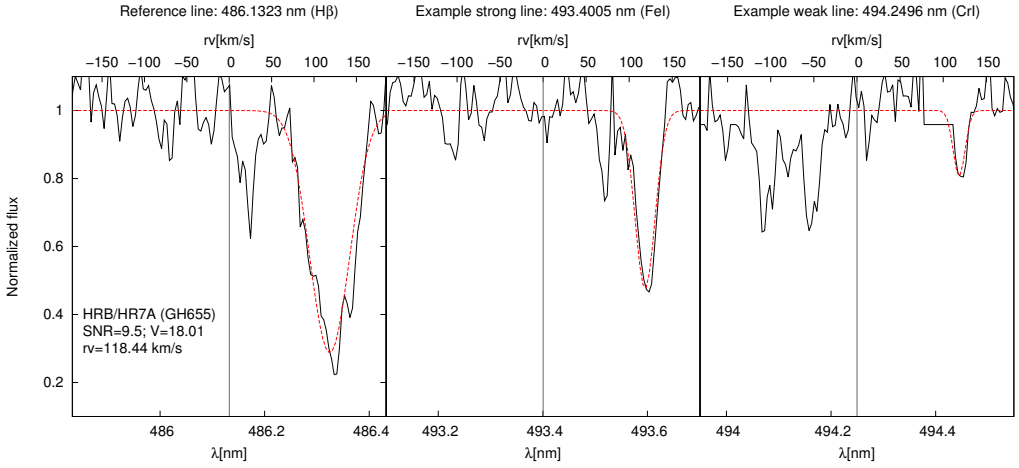

Figure B-6: Example of 3 lines for rv measurements in HRB/HR7A grism.

λ [Å]	species	λ [Å]	species	λ [Å]	species	λ [Å]	species	λ [Å]	species
5334.868	CrII	5367.466	FeI	5409.783	CrI	5455.609	FeI	5586.756	FeI
5339.929	FeI	5371.489	FeI	5415.199	FeI	5466.396	FeI	5594.462	CaI
5341.024	FeI	5383.369	FeI	5424.068	FeI	5497.516	FeI	5598.48	CaI
5345.796	CrI	5393.168	FeI	5429.696	FeI	5501.465	FeI	5602.877	SiI
5348.314	CrI	5397.128	FeI$^{(*)}$	5434.524	FeI	5506.779	FeI	...	...
5353.374	FeI	5400.501	FeI	5445.042	FeI	5528.405	MgI	...	...
5353.391	NiI	5400.596	CrI	5446.917	FeI	5554.895	FeI	...	...
5362.869	FeII	5404.151	FeI	5455.454	FeI	5572.842	FeI	...	...

Table B.7: List of lines for radial velocity measurements in HR (HR10). The asterisk (*) marks the reference line used in this grism.

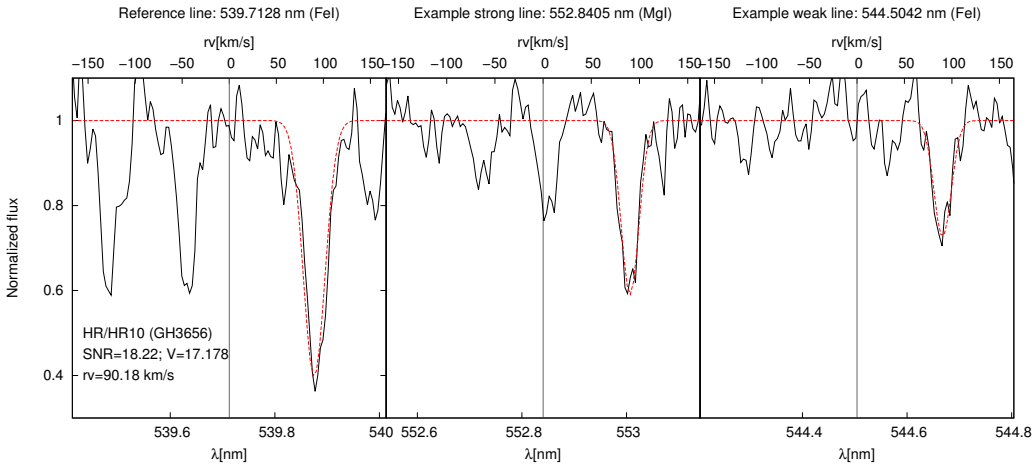

Figure B-7: Example of 3 lines for rv measurements in HR/HR10 grism.

λ [Å]	species	λ [Å]	species	λ [Å]	species	λ [Å]	species	λ [Å]	species
6122.217	CaI	6162.173	CaI	6215.143	FeI	6280.618	FeI	6336.824	FeI
6136.615	FeI	6163.755	CaI	6219.28	FeI	6297.792	FeI	6358.697	FeI
6137.691	FeI	6169.563	CaI	6230.722	FeI	6301.501	FeI	6393.6	FeI
6141.732	FeI$^{(*)}$	6173.334	FeI	6246.319	FeI	6314.659	NiI	...	...
6147.734	FeI	6180.203	FeI	6252.555	FeI	6318.018	FeI	...	...
6151.618	FeI	6200.313	FeII	6254.257	FeI	6322.685	FeI	...	...
6161.297	CaI	6213.429	FeII	6265.134	FeI	6335.33	FeI	...	...

Table B.8: List of lines for radial velocity measurements in HR (HR13). The asterisk (*) marks the reference line used in this grism.

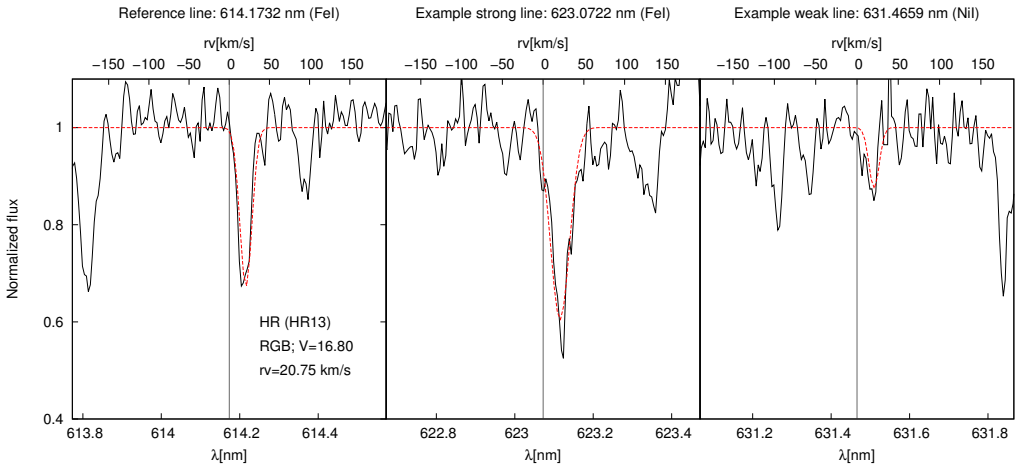

Figure B-8: Example of 3 lines for rv measurements in HR/HR13 grism.

λ [Å]	species	λ [Å]	species	λ [Å]	species	λ [Å]	species	λ [Å]	species
6393.6	FeI	6430.846	FeI	6481.869	FeI	6496.91	BaII	6562.797	HI
6408.018	FeI	6432.677	FeII	6482.796	NiI	6498.94	FeI	6572.779	CaI
6411.649	FeI	6439.075	CaI	6491.561	TiI	6499.65	CaI	6575.016	FeI
6419.949	FeI	6462.567	CaI$^{(*)}$	6493.781	CaI	6516.077	FeII	6592.913	FeI
6421.35	FeI	6471.662	CaI	6494.98	FeI	6546.238	FeI	6593.87	FeI

Table B.9: List of lines for radial velocity measurements in HR (HR14A). The asterisk (*) marks the reference line used in this grism.

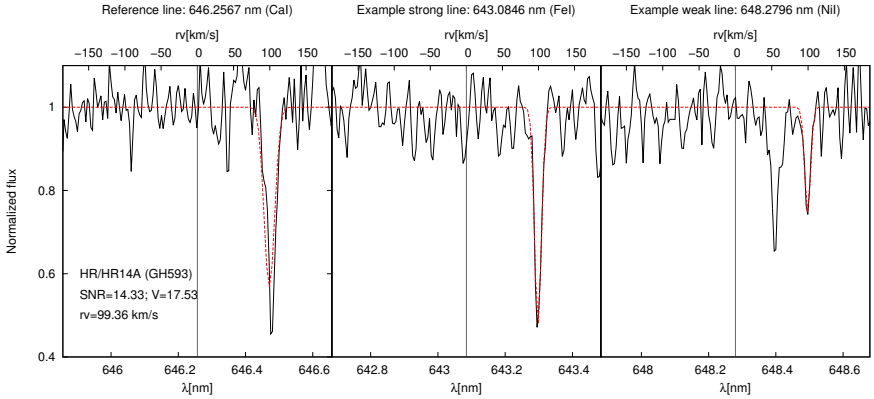

Figure B-9: Example of 3 lines for rv measurements in HR/HR14A grism.

λ [Å]	species	λ [Å]	species	λ [Å]	species	λ [Å]	species	λ [Å]	species
6613.735	FeI	6677.985	FeI	6743.122	TiI	6810.262	FeI	6914.559	NiI
6643.63	NiI	6703.566	FeI	6750.152	FeI$^{(*)}$	6841.339	FeI	6916.682	FeI
6648.08	FeI	6710.318	FeI	6752.707	FeI	6843.656	FeI	6945.204	FeI
6663.441	FeI	6717.681	CaI	6767.772	NiI	6858.132	FeI	...	...

Table B.10: List of lines for radial velocity measurements in HR (HR15). The asterisk (*) marks the reference line used in this grism.

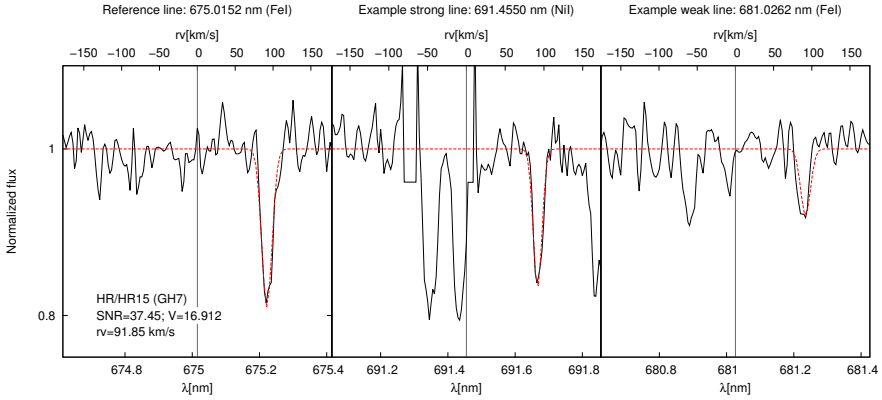

Figure B-10: Example of 3 lines for rv measurements in HR/HR15 grism.

GIRAFFE low resolution

λ [Å]	species	λ [Å]	species	λ [Å]	species	λ [Å]	species
8183.255	NaI	8434.957	TiI	8662.141	CaII	8838.428	FeI
8186.796	FeI	8498.023	CaII	8674.746	FeI	9228.093	SI
8194.824	NaI	8542.091	CaII$^{(*)}$	8688.624	FeI	9229.017	HI
8327.057	FeI	8582.258	FeI	8742.446	SiI	9255.778	MgI
8387.773	FeI	8611.803	FeI	8806.756	MgI	...	...

Table B.11: List of lines for radial velocity measurements in LR (LR08). The asterisk (*) marks the reference line used in this grism.

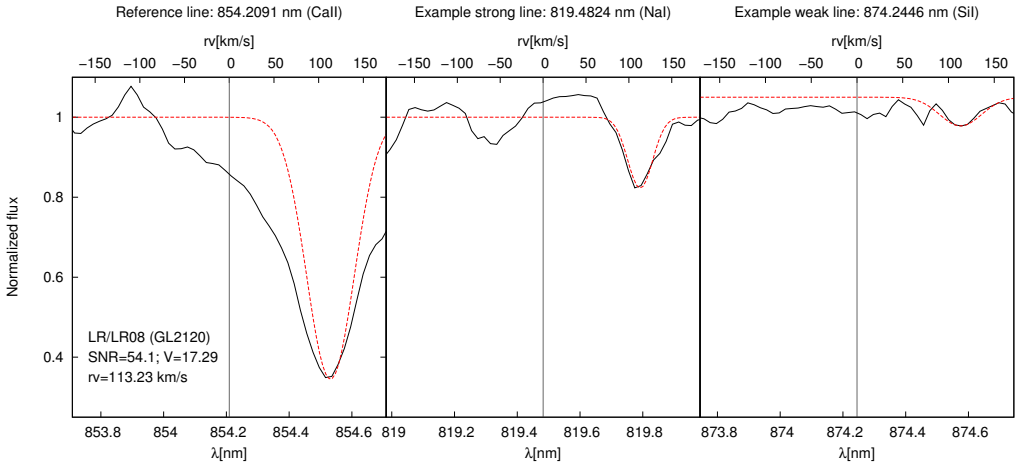

Figure B-11: Example of 3 lines for rv measurements in LR/LR08 grism.

Bibliography

[1] N. C. Amorisco and N. W. Evans. Line profiles from discrete kinematic data. *mnras*, 424:1899–1913, August 2012.

[2] T. E. Armandroff and G. S. Da Costa. The radial velocity, velocity dispersion, and mass-to-light ratio of the Sculptor dwarf galaxy. *aj*, 92:777–786, October 1986.

[3] Giuseppina Battagli. *Chemistry and kinematics of stars in Local Group galaxies*. PhD thesis, University of Groningen, 2007.

[4] Giuseppina Battaglia, Amina Helmi, and Maarten Breddels. Internal kinematics and dynamical models of dwarf spheroidal galaxies around the milky way. *New Astronomy Reviews*, 57(3 - 4):52 – 79, 2013. Galactic Archaeology.

[5] M. Boylan-Kolchin, J. S. Bullock, and M. Kaplinghat. Too big to fail? The puzzling darkness of massive Milky Way subhaloes. *mnras*, 415:L40–L44, July 2011.

[6] T. J. L. de Boer, E. Tolstoy, V. Hill, A. Saha, K. Olsen, E. Starkenburg, B. Lemasle, M. J. Irwin, and G. Battaglia. The star formation and chemical evolution history of the sculptor dwarf spheroidal galaxy. *aap*, 539:A103, March 2012.

[7] M. Fabrizio, G. Bono, M. Nonino, E. L. Łokas, I. Ferraro, G. Iannicola, R. Buonanno, S. Cassisi, G. Coppola, M. Dall'Ora, R. Gilmozzi, M. Marconi, M. Monelli, M. Romaniello, P. B. Stetson, F. Thévenin, and A. R. Walker. The carina project. x. on the kinematics of old and intermediate-age stellar populations1,2. *The Astrophysical Journal*, 830(2):126, 2016.

[8] M. Fabrizio, I. Ferraro, G. Iannicola, G. Bono, M. Nonino, and F. Thévenin. On the kinematic structure of the Carina dwarf spheroidal galaxy. In *Journal of Physics Conference Series*, volume 383 of *Journal of Physics Conference Series*, page 012009, October 2012.

[9] C. E. Martínez-Vázquez, M. Monelli, G. Bono, P. B. Stetson, I. Ferraro, E. J. Bernard, C. Gallart, G. Fiorentino, G. Iannicola, and A. Udalski. Variable stars in Local Group Galaxies - I. Tracing the early chemical enrichment and radial gradients in the Sculptor dSph with RR Lyrae stars. *mnras*, 454:1509–1516, December 2015.

[10] C. E. Martínez-Vázquez, P. B. Stetson, M. Monelli, E. J. Bernard, G. Fiorentino, C. Gallart, G. Bono, S. Cassisi, M. Dall'Ora, I. Ferraro, G. Iannicola, and A. R. Walker. Variable stars in Local Group Galaxies - II. Sculptor dSph. *mnras*, 462:4349–4370, November 2016.

[11] Alan W. McConnachie. The observed properties of dwarf galaxies in and around the local group. *The Astronomical Journal*, 144(1):4, 2012.

[12] Q. E. Minor. Binary Populations in Milky Way Satellite Galaxies: Constraints from Multi-epoch Data in the Carina, Fornax, Sculptor, and Sextans Dwarf Spheroidal Galaxies. *apj*, 779:116, December 2013.

[13] H. Mo, F. C. van den Bosch, and S. White. *Galaxy Formation and Evolution*. Cambridge University Press, Cambridge, UK, 2010.

[14] B. Moore, S. Ghigna, F. Governato, G. Lake, T. Quinn, J. Stadel, and P. Tozzi. Dark Matter Substructure within Galactic Halos. *apjl*, 524:L19–L22, October 1999.

[15] J. F. Navarro, C. S. Frenk, and S. D. M. White. The Structure of Cold Dark Matter Halos. *apj*, 462:563, May 1996.

[16] J. F. Navarro, C. S. Frenk, and S. D. M. White. A Universal Density Profile from Hierarchical Clustering. *apj*, 490:493–508, December 1997.

[17] J. Peñarrubia, A. Pontzen, M. G. Walker, and S. E. Koposov. The Coupling between the Core/Cusp and Missing Satellite Problems. *apjl*, 759:L42, November 2012.

[18] A. Pontzen and F. Governato. Cold dark matter heats up. *nat*, 506:171–178, February 2014.

[19] D. Queloz, P. Dubath, and L. Pasquini. A kinematic study of the Sculptor dwarf spheroidal galaxy. *aap*, 300:31, August 1995.

[20] T. Sawala, C. S. Frenk, A. Fattahi, J. F. Navarro, R. G. Bower, R. A. Crain, C. Dalla Vecchia, M. Furlong, J. C. Helly, A. Jenkins, K. A. Oman, M. Schaller, J. Schaye, T. Theuns, J. Trayford, and S. D. M. White. The APOSTLE simulations: solutions to the Local Group's cosmic puzzles. *mnras*, 457:1931–1943, April 2016.

[21] H. Shapley. A Stellar System of a New Type. *Harvard College Observatory Bulletin*, 908:1–11, March 1938.

[22] L. E. Strigari, C. S. Frenk, and S. D. M. White. Dynamical Models for the Sculptor Dwarf Spheroidal in a ΛCDM Universe. *apj*, 838:123, April 2017.

[23] K. Takeuchi. A Problem in Statistics. (Book Reviews: Robust Estimates of Location. Survey and Advances). *Science*, 179:469–470, February 1973.

[24] E. Tolstoy, V. Hill, and M. Tosi. Star-Formation Histories, Abundances, and Kinematics of Dwarf Galaxies in the Local Group. *araa*, 47:371–425, September 2009.

[25] M. G. Walker, M. Mateo, E. W. Olszewski, B. Sen, and M. Woodroofe. Clean kinematic samples in dwarf spheroidals: An algorithm for evaluating membership and estimating distribution parameters when contamination is present. *aj*, 137:3109–3138, February 2009.

[26] Matthew G. Walker, Mario Mateo, and Edward W. Olszewski. Stellar velocities in the carina, fornax, sculptor, and sextans dsph galaxies: Data from the magellan/mmfs survey. *The Astronomical Journal*, 137(2):3100, 2009.

[27] Matthew G. Walker, Mario Mateo, Edward W. Olszewski, Rebecca Bernstein, Bodhisattva Sen, and Michael Woodroofe. The michigan/mike fiber system survey of stellar radial velocities in dwarf spheroidal galaxies: Acquisition and reduction of data. *The Astrophysical Journal Supplement Series*, 171(2):389, 2007.

[28] Matthew G. Walker, Mario Mateo, Edward W. Olszewski, Oleg Y. Gnedin, Xiao Wang, Bodhisattva Sen, and Michael Woodroofe. Velocity dispersion profiles of seven dwarf spheroidal galaxies. *The Astrophysical Journal Letters*, 667(1):L53, 2007.